Technische Universität München

Max-Planck-Institut für Quantenoptik

Classical and Quantum Simulations of Many–Body Systems

Valentin Murg

Zusammenfassung

Diese Arbeit widmet sich kürzlichen Entwicklungen im Bereich der klassischen Simulationen und der Quantensimulationen von Vielteilchensystemen.

Wir beschreiben neue klassische Algorithmen, die Probleme von konventionellen Methoden wie Renormalisierungsgruppen- oder Monte Carlo Methoden bewältigen. Diese Algorithmen ermöglichen sowohl die Untersuchung von thermischen Eigenschaften zweidimensionaler klassischer Systeme und eindimensionaler Quantensysteme, als auch die Analyse von Grundzuständen und Zeitentwicklungen zweidimensionaler frustrierter oder fermionischer Quantensysteme.

Desweiteren machen wir Vorschläge für „analoge" Quantensimulatoren, die interessante Modelle wie das Tonks–Girardeau Gas oder das frustrierte XY–Modell auf einem trigonalen Gitter realisieren. Diese Simulatoren basieren auf optischen Gittern und Ionenfallen und sind technisch umsetzbar. Das Tonks–Girardeau Gas konnte experimentell bereits nachgewiesen werden. Für dieses zeigen wir einen detaillierten Vergleich der experimentellen Daten mit unseren theoretischen Vorhersagen.

Abstract

This thesis is devoted to recent developments in the fields of classical and quantum simulations of many–body systems.

We describe new classical algorithms that overcome problems apparent in conventional renormalization group and Monte Carlo methods. These algorithms make possible the detailed study of finite temperature properties of 2–D classical and 1–D quantum systems, the investigation of ground states of 2–D frustrated or fermionic systems and the analysis of time evolutions of 2–D quantum systems.

Furthermore, we propose new "analog" quantum simulators that are able to realize interesting models such as a Tonks–Girardeau gas or a frustrated spin–1/2 XY model on a trigonal lattice. These quantum simulators make use of optical lattices and trapped ions and are technically feasible. In fact, the Tonks–Girardeau gas has been realized experimentally and we provide a detailed comparison between the experimental data and the theoretical predictions.

Contents

Part I

Overview

Simulations of many–body quantum systems on a classical computer are known to be difficult problems. The difficulties have its origin in the *exponential* scaling of the required resources in time and space with the number of particles the system consists of. Consider, for example, a system of N spin-1/2-particles. The number of parameters that are required to describe the state of this system amounts to 2^N. Thus, the memory that has to be allocated in order to save the state of the system grows *exponentially* with the number of particles N. This has the consequence that the description of a system consisting of merely 50 particles ($N = 50$) requires several *million* Gigabytes of memory. On top of that, the number of elementary steps that the computer has to execute in order to perform the simulation is of order 2^{2N}. Thus, the time required for performing the simulation grows *exponentially* with the number of particles N, as well. In the case of 50 particles, this means that the the simulation will last no longer than 10^{13} years at Gigahertz speed.

Because of these difficulties, methods have been developed to simulate quantum systems on a classical computer in an *approximate* way. Popular methods are the renormalization group algorithms by K. Wilson [170] and S. White [169, 168, 135, 117] and quantum Monte Carlo methods [19]. Both of them have been used with great success, but they also have severe limitations: the renormalization group only works in cases where the original Hamiltonian can be mapped to a local Hamiltonian defined on a one–dimensional chain, while Monte Carlo methods suffer from the so–called sign problem [150] which makes them inappropriate for the description of fermionic and frustrated quantum systems. Very recently however, new insights coming from the field of quantum information and entanglement theory have shown how renormalization group methods can be generalized to higher dimensions, to finite temperature, to random systems etc. [160, 177, 162, 157, 156, 154, 101, 100, 114, 3]

Another approach to simulate many–body quantum systems goes back to a conjecture of Feynman in 1982 [40]: he proposed that quantum systems should be simulated by means of other quantum systems. His suspicion was that the exploitation of quantum effects would make the simulation more efficient and remove the exponential scaling. In 1996, this suspicion was shown to be correct by Seth Lloyd [86]. Seth Lloyd introduced the concept of a *Universal Quantum Simulator*. The *Universal Quantum Simulator* is a quantum computer equipped with a quantum algorithm that is capable of simulating the dynamics of arbitrary quantum systems. This algorithm is proven to be efficient, i.e. the duration of the algorithm scales *polynomially* with the size of the simulated quantum system. The only drawback is that a quantum computer is very difficult to build in practice and has very de-

manding requirements. Fortunately, there are physical systems with which it is not known how to build a quantum computer, but in which one can engineer certain kinds of interactions and thus simulate other systems. The advantage is that it is more controllable than the original system, so that more may be learned from the "analog" system rather than from the real version. Examples are atoms in optical lattices [54, 10, 93] or trapped ions interacting with lasers [26, 122, 121]. In those systems, one does not require to individually address the qubits, or to perform quantum gates on arbitrary pairs of qubits, but rather on all of them at the same time. Besides, one is interested in measuring physical properties (like magnetization, conductivity, etc.) which are robust with respect to the appearance of several errors. In a quantum computer without error correction, even a single error will destroy the computation. For example, to see whether a material is conducting or not one does not need to know with a high precision the corresponding conductivity.

Both the approximate simulations on a classical computer (termed "classical simulations" in the following) and simulations using a quantum system (termed "quantum simulations" in the following) bear the potential of understanding quantum systems that form a cornerstone of condensed–matter physics, chemistry or nuclear physics. For example, these methods might make it feasible to obtain an accurate description of chemical compounds and reactions, to gain deeper understanding of high temperature superconductivity, or to find out the reason why quarks are always confined.

In this thesis, recent developments in the fields of classical and quantum simulations are reported. New classical algorithms are described that overcome problems apparent in conventional renormalization group and Monte Carlo methods. These algorithms make possible the detailed study of finite temperature properties of 2–D classical and 1–D quantum systems, the investigation of the ground state of 2–D frustrated or fermionic systems and the analysis of time evolutions of 2–D quantum systems. Furthermore, new "analog" quantum systems are proposed that are able to realize interesting models such as a Tonks–Girardeau gas [51, 85] or a frustrated spin–1/2 XY model on a trigonal lattice. These quantum systems make use of optical lattices and trapped ions and are technically feasible. In fact, the Tonks–Girardeau gas has been realized experimentally and we provide a detailed comparison between the experimental data and the theoretical predictions.

The thesis is organized in two parts: part II is devoted to classical simulations and part III deals with quantum simulations.

Part II starts with a short introduction in chapter 1 on renormalization group methods from the viewpoint of the field of quantum information. In chapter 2, a joint work with Frank Verstraete and Ignacio Cirac is described

that is published in [100]. In this work, a method to calculate partition functions of 2–D classical systems and 1–D quantum systems is proposed. This method makes use of the variational algorithm for time evolution with matrix product states [47]. In chapter 3, this method is tested on the (exactly solvable) 2–D Ising model. Furthermore, it is used to predict density and momentum distributions at finite temperature of atoms in a 1–D optical lattice, which is a problem of great experimental interest [115]. In chapter 4, a natural extension of the class of MPS to two and higher dimensions is discussed and variational algorithms for finding the ground state and performing time evolutions within this class are described. This class of states has been introduced by Frank Verstraete and Ignacio Cirac in [154] and variational algorithms within this class have been proven to be useful for finding the ground state of the 2–D Heisenberg model. In chapter 5, these algorithms are applied to other models of interest. In particular, results for hard–core bosons on a 2–D optical lattice and 2–D frustrated antiferromagnets are presented. These results emanate from a joint work with Frank Verstraete and Ignacio Cirac and are published in [101] and [102]. Fragments of part II are also appear in a review paper about variational renormalization group methods published in [155].

In part III, two examples of "analog" quantum simulators are given. In Chapter 8, a joint work with Bélen Paredes, Artur Widera, Olaf Mandel, Simon Fölling, Ignacio Cirac, Gora V. Shlyapnikov, Theodor W. Hänsch and Immanuel Bloch is presented that is published in [115]. In this work, a way to create a gas of hard–core bosons in one dimension - a so–called Tonks-Girardeau gas - by means of atoms in an optical lattice is proposed. This work is special in the sense that it has been possible to validate this proposal experimentally. We give a detailed quantitative comparison of the experimental results and our theoretical predictions. Chapter 9 comprises a joint work with Roman Schmied, Tommaso Roscilde, Diego Porras and Ignacio Cirac, published in [134]. In this work, extensions of the idea to realize effective spin–models and interacting–boson models by means of trapped ions interacting with lasers [122, 121] are discussed. It is shown that a wide range of spatial dimensions and particle interactions may be achieved by placing the ions in a regular structure induced by an optical lattice or arrays of ion microtraps. In particular, the realization of the spin–1/2 model with frustrated XY interactions on a triangular lattice is illustrated. It is shown that this model has potentially interesting properties by applying the algorithm of chapter 4 in part II.

Part II

Classical Simulations

Chapter 1

Introduction

One of the main characteristics of quantum mechanics is that the underlying Hilbert space is endowed with a tensor product structure: the Hilbert space of two interacting systems is given by the tensor product space of the two individual ones. This structure of the Hilbert space is a direct consequence of the superposition principle, and opens up the possibility of entanglement and new phases of matter. This simple tensor product structure, however, makes it very clear what the main obstacle is in developing a general theory of quantum many-body quantum systems: the size of the Hilbert space grows exponentially in the number of basis constituents, and hence we would, in principle, need exponentially many variables to specify the wavefunction of a N-particle system. However, it is a priori not clear whether Nature can fully exploit and explore these vast territories of Hilbert space, because another main characteristic of quantum mechanics is that interactions always seem to happen locally and only between a few bodies.

As it turns out, all physical states live on a tiny submanifold of the Hilbert space: if we consider, for example, a system of a few hundred spins, it would take much longer than the lifetime of the universe to come close to a random point in the Hilbert space by an evolution with local interactions [158]. This shows that almost all points in the Hilbert space of a many–body quantum system are unphysical as they are inaccessible. This opens up a very interesting perspective in the context of the description of quantum many-body systems, as there might exist an efficient parametrization of such a submanifold that would provide the natural language for describing those systems. In the context of many-body quantum physics, one is furthermore mainly interested in describing the low energy sector of local Hamiltonians, and as we will discuss later, this puts many extra constraints on the allowed wavefunctions.

As a trivial example of such a submanifold, let's consider a system of $N \to \infty$ spins that all interact with each other via a permutation invariant

2–body Hamiltonian such as the Heisenberg interaction [61, 32]. Note that there is always a ground state that exhibits the same symmetry as the Hamiltonian. As a consequence of the quantum de-Finnetti theorem [146] one can show that the manifold of all density operators with permutation symmetry is exactly the set of all separable states $\rho = \sum_i p_i \rho_i^{\otimes N}$ when $N \to \infty$. Ground states correspond to the extreme points of this set, which are exactly the product states that have no entanglement. All ground states of permutational invariant systems therefore lie on the submanifold of separable states which indeed have an efficient representation (only N vectors, one for each individual spin, have to be specified); this is the equivalent statement as saying that mean-field theory becomes exact in the thermodynamic limit. This can also be understood in the context of the monogamy property of entanglement [27]: a spin has only a finite entanglement susceptibility, and if it has to share the entanglement with infinitely many other spins then the amount of entanglement between 2 spins will be go to zero.

In the more general situation when no permutation symmetry is present but only a smaller symmetry group such as the group of translations, the characterization of the relevant manifold is much harder. In contrast to the case of permutation symmetry, where every pure state of N spin s systems can be written as a linear combination of a polynomial number of states, the size of a complete basis of translational invariant states is exponentially increasing as $(2s+1)^N/N$, and hence the manifold of interest has exponentially many parameters. But ground states of local Hamiltonians have many more nongeneric properties, most notably the fact that they have extremal local properties such as to minimize the energy: as the energy is only dependent on the local properties, and the ground state is determined by the condition that its energy is extremal, ground states have extremal local properties and the global properties only emerge to allow for these local properties to be extremal. As an example, let's consider a spin–1/2 antiferromagnetic chain with associated Hamiltonian

$$H_{\text{Heis}} = \sum_{\langle i,j \rangle} \vec{S}_i \vec{S}_j$$

where the notation $\langle i, j \rangle$ denotes the sum over nearest neighbours. Each individual term in the Hamiltonian corresponds to an exchange interaction and would be minimized if spins i and j are in the singlet state

$$|\psi\rangle = \frac{1}{\sqrt{2}} \left(|01\rangle - |10\rangle \right),$$

but due to the monogamy or frustration properties of entanglement, a spin 1/2 cannot be in a singlet state with more than one neighbour. As a result,

the ground state becomes a complicated superposition of all possible singlet coverings, and as an interesting by–product quasi long–range order may arise. The important point, however, is that this wavefunction arises from the condition that its local properties are extremal: finding ground states of local translational invariant 2–body Hamiltonians is equivalent to characterizing the convex set of 2–body density operators that originate from a state with the right symmetry [153].

Clearly, we would like to parameterize the manifold of states $\{|\psi_{ex}\rangle\}$ with extremal local properties. In practice, it is enough to parameterize a manifold of states $\{|\psi_{appr}\rangle\}$ such that there always exists a large overlap with the exact states $\{|\psi_{ex}\rangle\}$:

$$\forall |\psi_{ex}\rangle, \exists |\psi_{appr}\rangle : \||\psi_{ex}\rangle - |\psi_{appr}\rangle\| \leq \epsilon$$

Let's consider any local Hamiltonian of N spins that exhibits the property that there is a unique ground state $|\psi_{ex}\rangle$ and that the gap is $\Delta(N)$. Let's furthermore consider the case when $\Delta(N)$ decays not faster than an inverse polynomial in N (this condition is satisfied for all gapped systems and for all known critical translational invariant systems in 1D). Then let's assume that there exists a state $|\psi_{appr}\rangle$ that reproduces well the local properties of all nearest neighbour reduced density operators: $\|\rho_{appr} - \rho_{ex}\| \leq \delta$. Then it follows that the global overlap is bounded by

$$\||\psi_{ex}\rangle - |\psi_{appr}\rangle\|^2 \leq \frac{N\delta}{\Delta(N)}.$$

This is remarkable as it shows that it is enough to reproduce the local properties well to guarantee that also the global properties are reproduced accurately: for a constant global accuracy ϵ, it is enough to reproduce the local properties well to an accuracy δ that scales as an inverse polynomial (as opposed to exponential) in the number of spins. This is very relevant in the context of variational simulation methods: if the energy is well reproduced and if the computational effort to get a better accuracy in the energy only scales polynomially in the number of spins, then a numerical method with polynomial scaling can be constructed that reproduces all global properties well.

The central question is thus: is it possible to find an efficient parameterization of a manifold of states whose local properties approximate well all possible local properties? A very interesting new development, mainly originating from the field of quantum information and entanglement theory, has shown that this is indeed possible. The main idea is to come up with a class of variational wave functions that captures the physics of the low-energy sector of local quantum spin Hamiltonians.
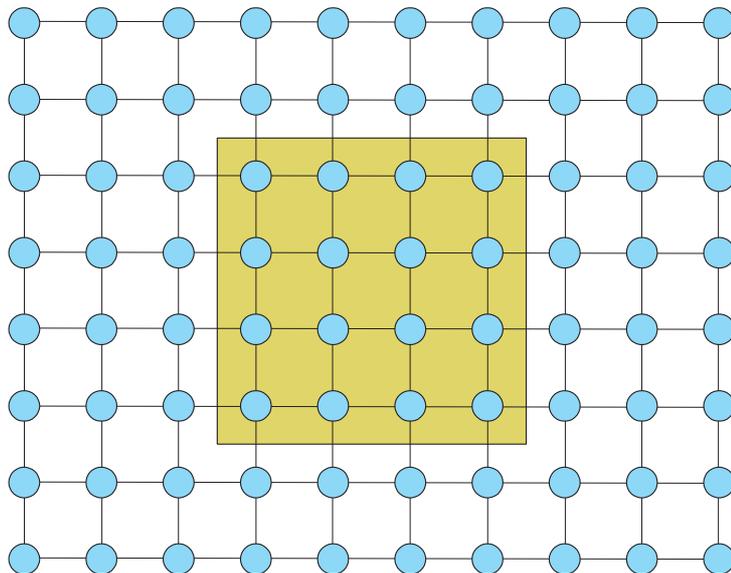
Figure 1.1: The entropy of a block of spins scales like the perimeter of the block.

So what other properties do ground states of local quantum Hamiltonians exhibit besides the fact that all global properties follow from their local ones? The key concept to understand their structure is to look at the amount of entanglement present in those states [163]: entanglement is the crucial ingredient that forces quantum systems to behave differently than classical ones, and it is precisely the existence of entanglement that is responsible for such exotic phenomena like quantum phase transitions and topological quantum order [166, 82]. It is also the central resource that gives rise to the power of quantum computing [103], and it is known that a lot of entanglement is needed between the different qubits as otherwise the quantum computation can be simulated on a classical computer [68, 160]. This is because the amount of entanglement effectively quantifies the relevant number of degrees of freedom that have to be taken into account, and if this is small then the quantum computation could be efficiently simulated on a classical computer. In the case of ground states of strongly correlated quantum many-body systems, there is also lot's of entanglement, but the key question is obviously to ask how much entanglement is present there: maybe the amount of entanglement is not too big such that those systems can still be simulated classically?

Let's for example consider a quantum spin system on a n-dimensional infinite lattice, and look at the reduced density operator ρ_L of a block of spins in a $L \times L \times \cdots \times L$ hypercube (Figure 1.1). The von-Neumann entropy of

ρ_L is a coarse-grained measure that quantifies the number of modes in that block that are entangled with the outside [103], and the relevant quantity is to study how this entropy scales with the size of the cube. This question was first studied in the context of black-hole entropy [8, 143, 49, 15] and has recently attracted a lot of attention [163]. Ground states of local Hamiltonians of spins or bosons seem to have the property that the entropy is not an extensive property but that the leading term in the entropy only scales as the boundary of the block (hence the name area-law):

$$S(\rho_L) \simeq cL^{n-1} \tag{1.1}$$

This has a very interesting physical meaning: it shows that most of the entanglement must be concentrated around the boundary, and therefore there is much less entanglement than would be present in a random quantum state (where the entropy would be extensive and scale like L^n). This is very encouraging, as it indicates that the wavefunctions involved exhibit some form of locality, and we might be able to exploit that to come up with efficient local parameterizations of those ground states.

The area law (1.1) is mildly violated in the case of 1-D critical spin systems where the entropy of a block of spins scales like [163, 14]

$$S(\rho_L) \simeq \frac{c + \bar{c}}{6} \log L,$$

but even in that case the amount of entanglement is still exponentially smaller then the amount present in a random state. It is at present not clear to what extent such a logarithmic correction will occur in the case of higher dimensional systems: the block-entropy of a critical 2-D system of free fermions scales like $L \log L$ [172, 50], while critical 2-D spin systems were reported where no such logarithmic correction are present [159], but in any case the amount of entanglement will be much smaller than for a random state. It is interesting to note that this violation of an area law is a pure quantum phenomenon as it occurs solely at zero temperature: in a recent paper [171], it has been shown that the block entropy, as measured by the mutual information (which is the natural measure of correlations for mixed states), obeys an exact area law for all local classical or quantum Hamiltonians. The logarithmic corrections therefore solely arise due to the zero-temperature quantum fluctuations. From the practical point of view, that might indicate that thermal states at low temperature are simpler to simulate than exact ground states.

The existence of an area law for the scaling of entropy is intimately connected to the fact that typical quantum spin systems exhibit a finite correlation length. In fact, M. Hastings has recently proven that all connected

$$\langle O_A O_B \rangle - \langle O_A \rangle \langle O_B \rangle \approx \exp\left(-\frac{l_{AB}}{\xi_{corr}}\right)$$

A   B

C

$$l_{AB} \gg \xi_{corr}$$
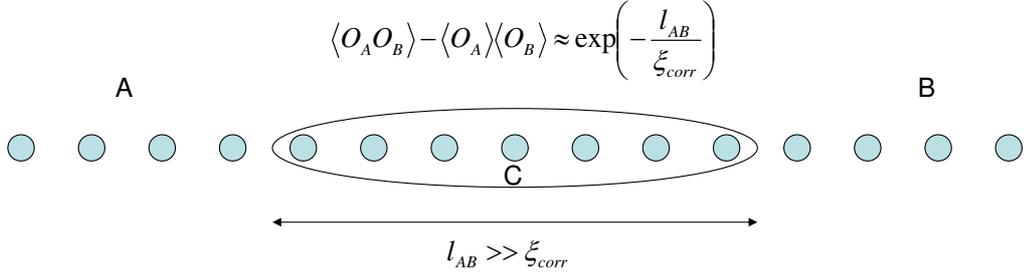
Figure 1.2: (taken from [153]) A one dimensional spin chain with finite correlation length ξ_{corr}; l_{AB} denotes the distance between the block A (left) and B (right). Because l_{AB} is much larger than the correlation length ξ_{corr}, the state ρ_{AB} is essentially a product state.

correlation functions between two blocks in a gapped system have to decay exponentially as a function of the distance of the blocks [59]. Let us therefore consider a 1-D gapped quantum spin system with correlation length ξ_{corr}. Due to the finite correlation length, the reduced density operator ρ_{AB} obtained when tracing out a block C of length $l_{AB} \gg \xi_{corr}$ (see figure 1.2) will be equal to

$$\rho_{AB} \simeq \rho_A \otimes \rho_B \tag{1.2}$$

up to exponentially small corrections. The original ground state $|\psi_{ABC}\rangle$ is a purification of this mixed state, but it is of course also possible to find another purification of the form $|\psi_{AC_l}\rangle \otimes |\psi_{BC_r}\rangle$ (up to exponentially small corrections) with no correlations whatsoever between A and B; here C_l and C_r together span the original block C. It is however well known that all possible purifications of a mixed state are equivalent to each other up to local unitaries on the ancillary Hilbert space. This automatically implies that there exists a unitary operation U_C on the block C (see figure 1.2) that completely disentangles the left from the right part:

$$I_A \otimes U_C \otimes I_B |\psi_{ABC}\rangle \simeq |\psi_{AC_l}\rangle \otimes |\psi_{BC_r}\rangle.$$

Thus, there exists a tensor $A^i_{\alpha,\beta}$ with indices $1 \le \alpha, \beta, i \le D$ (where D is the dimension of the Hilbert space of C) and states $|\psi^A_\alpha\rangle, |\psi^C_i\rangle, |\psi^B_\beta\rangle$ defined on the Hilbert spaces belonging to A, B, C such that

$$|\psi_{ABC}\rangle \simeq \sum_{\alpha,\beta,i} A^i_{\alpha,\beta} |\psi^A_\alpha\rangle |\psi^C_i\rangle |\psi^B_\beta\rangle.$$

Applying this argument recursively leads to a matrix product state (MPS) description of the state and gives a strong hint that ground states of gapped
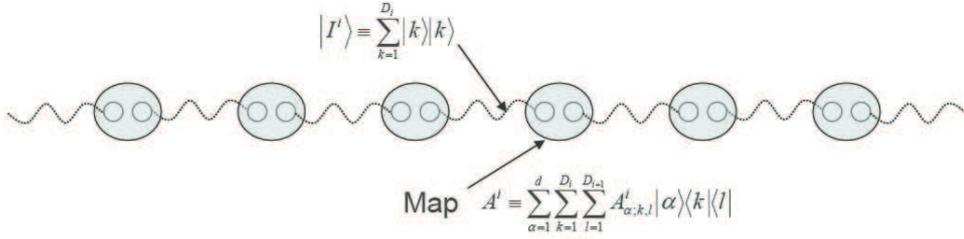
Figure 1.3: A general Matrix Product State

Hamiltonians are well represented by MPS. It turns out that this is even true for critical systems [153].

1.1 Matrix Product States

The most general form of a MPS [157, 36] on N spins of dimension d is given by

$$|\psi\rangle = \sum_{k_1,k_2,\ldots,k_N=1}^{d} \operatorname{tr}\left(A_{k_1}^{[1]}A_{k_2}^{[2]}\cdots A_{k_N}^{[N]}\right)|\,k_1\,\rangle|\,k_2\,\rangle\cdots|\,k_N\,\rangle$$

The matrices $A_k^{[i]}$ have dimension $D_i \times D_{i+1}$ (here we take the convention that $D_{N+1} = D_1$). A system with open boundary conditions is obtained by choosing $D_1 = 1$. Every state of N spins has an exact representation as a MPS if we allow D_i to grow exponentially in the number of spins; this can easily be shown by making use of the tool of quantum teleportation as shown in [157]. However, the whole point of MPS is that ground states can typically be represented by MPS where the dimension D_i is small and scales at most polynomially in the number of spins [153]. Then, the state is parametrized by a number of parameters that scale polynomially with N. This is the basic reason why variational methods within the set of MPS are exponentially more efficient than exact diagonalization.

A pictorial representation of a MPS is given in figure 1.3. In this picture, every physical spin at site i is replaced by two virtual spins of dimensions D_i and D_{i+1}. Each of the virtual spins forms a maximally entangled state

$$|\,I^i\,\rangle = \sum_{\gamma=1}^{D_i} |\,\gamma\,\rangle_i|\,\gamma\,\rangle_{i+1}$$

with one virtual spin of a neighboring site. The pair of virtual spins at site i is then projected onto the physical spin of dimension d by the linear map $A^{[i]}$.
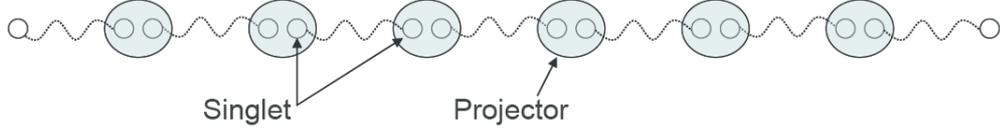
Figure 1.4: Building up the AKLT state by partial projections on bipartite singlets

This pictorial representation was first used in the work of Affleck, Kennedy, Lieb and Tasaki (AKLT) [2] in order to prove that the exact ground state of the spin-1 chain with Hamiltonian

$$\mathcal{H}_{AKLT} = \sum_{\langle i,j \rangle} \underbrace{\left(\vec{S}_i . \vec{S}_j + \frac{1}{3} \left(\vec{S}_i . \vec{S}_j \right)^2 + \frac{2}{3} \right)}_{=P_{ij}}$$

can be parameterized exactly as a matrix product state. To see this, they observed that the terms P_{ij} are projectors $(P_{ij})^2 = P_{ij}$ onto the 5-dimensional spin 2 subspace of 2 spin 1's, and proceeded by constructing the unique ground state $|\psi_{AKLT}\rangle$ which is annihilated by all projectors P_{ij} acting on nearest neighbours. This state $|\psi_{AKLT\rangle}$ can be constructed as follows:

- Imagine that the 3-dimensional Hilbert space of the a spin 1 particle is effectively the low-energy subspace of the Hilbert space spanned by 2 spin 1/2's, i.e. the 3-D Hilbert space is the symmetric subspace of 2 spin 1/2 particles.

- To assure that the global state defined on the spin chain has spin zero, let's imagine that each one of the spin 1/2's is in a singlet state with a spin 1/2 of its neighbours (see figure 1.4).

- The AKLT state can now be represented by locally projecting the pair of spin 1/2's in the symmetric subspace onto the spin-1 basis $\{|1\rangle, |0\rangle, |-1\rangle\}$:

$$
\begin{aligned}
P &= |-1\rangle \left(\frac{\langle 00| - \langle 11|}{\sqrt{2}} \right) + |0\rangle \left(\frac{\langle 01| + \langle 10|}{\sqrt{2}} \right) + |1\rangle \left(\frac{\langle 00| + \langle 11|}{\sqrt{2}} \right) \\
&\equiv \sum_{\alpha = x,y,z} |\alpha\rangle \left(\frac{\langle 00| + \langle 11|}{\sqrt{2}} \right) \tau_\alpha \otimes \tau_y
\end{aligned}
$$

where $\tau_x = \sigma_x, \tau_y = i\sigma_y, \tau_z = \sigma_z$ with $\{\sigma_\alpha\}$ the Pauli matrices and where we identified $|-1\rangle = |x\rangle, |0\rangle = |z\rangle, |1\rangle = |y\rangle$.

Historically, the AKLT state was very important as it shed new lights into the conjecture due to Haldane [57, 56] that integer spin Heisenberg chains give rise to a gap in the spectrum. That is a feature shared by all generic matrix product states: they are always ground states of local gapped quantum Hamiltonians.

Let's first try to rewrite $|\psi_{AKLT}\rangle$ in the MPS representation. Let's assume that we have an AKLT system of N spins with periodic boundary conditions; projecting the wavefunction in the computational basis leads to the following identity:

$$\langle \alpha_1, \alpha_2, ...\alpha_N | \psi_{AKLT} \rangle = \mathrm{Tr} \left(\tau_{\alpha_1}.\tau_{\mathrm{y}}.\tau_{\alpha_2}.\tau_{\mathrm{y}}...\tau_{\alpha_{\mathrm{N}}}\tau_{\mathrm{y}}. \right).$$

The different weights can therefore be calculated as a trace of a product of matrices. The complete AKLT state can therefore be represented as

$$|\psi_{AKLT}\rangle = \sum_{\alpha_1,\alpha_2,...\alpha_N} \mathrm{Tr} \left(\tau_{\alpha_1}.\tau_{\mathrm{y}}.\tau_{\alpha_2}.\tau_{\mathrm{y}}...\tau_{\alpha_{\mathrm{N}}}\tau_{\mathrm{y}}. \right) |\alpha_1\rangle|\alpha_2\rangle...|\alpha_{\mathrm{N}}\rangle$$

which is almost exactly of the same form as the matrix product states introduced earlier. The only difference between the is the occurence of the matrices τ_y between the different products. This is however only a consequence of the fact that we connected the different nodes with singlets, and we could as well have used maximally entangled states of the form

$$|I\rangle = \sum_{\gamma=1}^{2} |\gamma\rangle|\gamma\rangle$$

and absorbed τ_y into the projector; this way the the standard notation for MPS would have been recovered.

The calculus of MPS relies on the optimization of all parameters of the MPS, such that the expectation value of the energy

$$E = \frac{\langle \Psi |H| \Psi \rangle}{\langle \Psi | \Psi \rangle}$$

is minimized. The key idea to perform this optimization efficiently is to optimize the matrices $A_k^{[i]}$ of the MPS *independently* for each site i. Since both expressions $\langle \Psi |H| \Psi \rangle$ and $\langle \Psi | \Psi \rangle$ are quadratic functions in $A_k^{[i]}$, the optimization with respect to $A_k^{[i]}$ reduces to a simple eigenvalue problem in case of open boundary conditions and a generalized eigenvalue problem in case of periodic boundary conditions [157].

1.2   Matrix Product Operators

Instead of restricting our attention to pure matrix product states, we can readily generalize the approach and deal with matrix product operators (MPO). In its most general case, a MPO is defined as [156, 177]

$$\hat{O} = \sum_{k_1, k_2, \ldots, k_N = 1}^{d} \text{tr}\left(A_{k_1}^{[1]} A_{k_2}^{[2]} \cdots A_{k_N}^{[N]} \right) \sigma_{k_1} \otimes \sigma_{k_2} \otimes \cdots \otimes \sigma_{k_N} \qquad (1.3)$$

with σ_i a complete single particle basis (e.g. the Pauli matrices for a qubit).

Matrix product operators appear naturally in the variational formulation of time evolution with MPS [156]. There, every evolution following a Trotter step is expressed by a MPO. That MPO essentially plays the role of a transfer matrix during the evolution. As we will show later, any transfer matrix arising in the context of classical partition function will have an exact representation in terms of such a MPO. Matrix product operators have also been shown to be very useful to obtain spectral information about a given Hamiltonian. Examples are the parametrization of Gibbs states [156] and the simulation of random quantum spin systems [114].

The idea of the variational formulation of time evolution with MPS is, given a Hamiltonian and an initial MPS, to evolve that state within the manifold of MPS in such a way that the error in approximating the exact evolution is minimized at every infinitesimal step. We are particularly interested in the case where the Hamiltonian is a sum of local terms of the form

$$\mathcal{H} = \sum_{<ij>} f_{ij} \hat{O}_i \otimes \hat{O}_j$$

and where $< ij >$ means that the sum has to be taken over all pairs of nearest neighbours. There are several tools to discretize the corresponding evolution. This is not completely trivial because generically the different terms in the Hamiltonian don't commute. A standard tool is to use the Trotter decomposition [147, 148]

$$e^{A+B} = \lim_{n \to \infty} \left(e^{\frac{A}{n}} e^{\frac{B}{n}} \right)^n.$$

Suppose e.g. that the Hamiltonian can be split into two parts A and B such that all terms within A and within B are commuting: $\mathcal{H} = A + B; A = \sum_i A_i; B = \sum_i B_i; [A_i, A_j] = 0 = [B_i, B_j]$. This ensures that one can efficiently represent e^{iA} as a product of terms. The evolution can then be approximated by evolving first under the operator $e^{i\delta t A}$, then under $e^{i\delta t B}$, again under $e^{i\delta t A}$ and so further. The time step can be choosen such as to
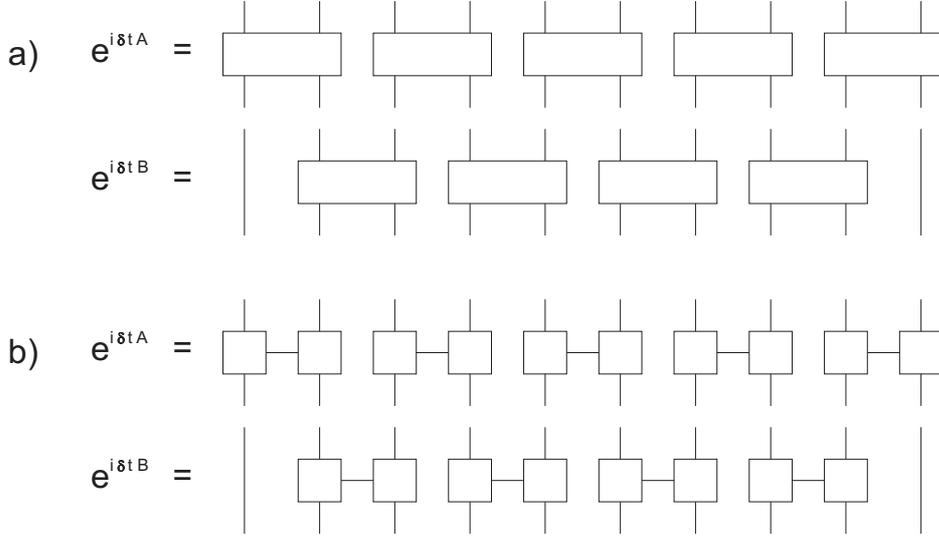
Figure 1.5: (a) Tensor network representation of the operators obtained in the case of a Trotter expansion of a nearest–neighbor Hamiltonian $H = A + B$ with A containing all interactions between odd–even sites and B all interactions between even–odd sites. (b) Tensor network representation after a Schmidt–decomposition of the 2-body operators.

ensure that the error made due to this discretization is smaller than a pre-specified error, and there is an extensive literature of how to improve on this by using e.g. the higher order Trotter decompositions [142, 111]. In the case of nearest neighbour Hamiltonians, a convenient choice for A is to take all terms that couple the even sites with the odd ones to the right of it and for B the ones to the left of it. In that case, $e^{i\delta t A}$ and $e^{i\delta t B}$ are tensor products of nearest-neigbour 2-body operators (see figure 1.5a for a pictorial representation). By performing Schmidt–decompositions of the 2-body operators, both $e^{i\delta t A}$ and $e^{i\delta t B}$ assume the form of MPOs (see figure 1.5b).

The time-evolution is treated in a variational way within the class of MPS as follows: a sensible cost function to minimize is given by

$$K = \| U |\psi(k)\rangle - |\psi(k+1)\rangle \|^2 \tag{1.4}$$

where $|\psi(k)\rangle$ is the initial MPS, $|\psi(k+1)\rangle$ is the one to be found, and U is the MPO arising out of the Trotter expansion. In principle, the cost function can be made equal to zero by increasing the bond dimension D of the MPS by a factor of at most d^2 (this is the largest possible Schmidt number of an operator acting on two sites). However, the whole point of using MPS is that MPS with low bond dimension are able to capture the

physics needed to describe the low-energy sector of the Hilbert space. So if we stay within that sector, the hope is that the bond dimension will not have to be multiplied by a constant factor at each step (which would lead to an exponential computational cost as a function of time), but will hopefully saturate. This is certainly the case if we evolve using e.g. imaginary time evolution of a constant local Hamiltonian, as we know that in that case the ground state is indeed well represented with a MPS with not too large bond dimension. It is however in principle possible that an exponential explosion occurs for real time evolution.

A way of dealing with time evolution is to prespecify an error ϵ, and then look for the minimal D for which there exists a MPS $|\psi(k+1)\rangle$ such that the cost function K is smaller than ϵ. The MPS $|\psi(k+1)\rangle$ that minimizes the cost function K can be found as follows: since the cost function has only multiquadratic and multilinear terms in the variables of the MPS, it can be minimized with respect to one site easily by solving a linear set of equations. In this way, the optimal MPS can be obtained by minimizing the cost function site-by-site until convergence is reached. After convergence, we can check how big the error has been for the particular value of D that we chose, and if this error is too big, we can increase D and repeat the optimization.

Chapter 2

Classical Partition Functions and Thermal Quantum States

In this chapter, we show how the concept of MPS and MPO can be used to calculate the free energy of a classical 2-dimensional spin system. This also leads to an alternative way of treating thermal states of 1-D quantum spin systems, as those can be mapped to classical 2-D spin systems by the standard classical-quantum mapping [1]. Historically, Nishino was the first one to pioneer the use of DMRG-techniques in the context of calculating partition functions of classical spin systems [105]. By making use of the Suzuki–Trotter decomposition, his method has then subsequently been used to calculate the free energy of translational invariant 1-D quantum systems [13, 139, 165], but the main restriction of those methods is that it cannot be applied in situations in which the number of particles is finite and/or the system is not homogeneous; furthermore, one has to explicitly use a system with periodic boundary condition in the quantum case, a task that is not well suited for standard DMRG. The variational MPS-approach gives an easy solution to those problems.

Our method relies in reexpressing the partition and correlation functions as a contraction of a collection of 4-index tensors, which are disposed according to a 2–D configuration [100]. We will perform this task for both 2–D classical and 1–D quantum systems.

---

[1]In the context of MPS and especially PEPS, there also exist a different mapping between classical and quantum spin models in the same dimension [159]. There, the thermal classical fluctuations map onto quantum ground state fluctuations, and this leads to a lot of insights in the nature of quantum spin systems.

2.1 2–D classical systems

Let us consider first the partition function of an inhomogeneous classical 2–D n–level spin system on a $L_1 \times L_2$ lattice. For simplicity we will concentrate on a square and nearest–neighbor interactions, although our method can be easily extended to other short–range situations. We have

$$Z = \sum_{x^{11},\ldots,x^{L_1 L_2}} \exp\left[-\beta H(x^{11},\ldots,x^{L_1 L_2})\right],$$

where

$$H\left(x^{11},\ldots\right) = \sum_{ij} \left[H^{ij}_\downarrow\left(x^{ij},x^{i+1,j}\right) + H^{ij}_\rightarrow\left(x^{ij},x^{i,j+1}\right)\right]$$

is the Hamiltonian, $x^{ij} = 1,\ldots,n$ and β is the inverse temperature. The singular value decomposition allows us to write

$$\exp\left[-\beta H^{ij}_q(x,y)\right] = \sum_{\alpha=1}^{n} f^{ij}_{q\alpha}(x)g^{ij}_{q\alpha}(y),$$

with $q \in \{\downarrow, \rightarrow\}$. Defining the tensors

$$X^{ij}_{lrud} = \sum_{x=1}^{n} f^{ij}_{\downarrow d}(x)g^{i-1,j}_{\downarrow u}(x)f^{ij}_{\rightarrow r}(x)g^{i,j-1}_{\rightarrow l}(x),$$

the partition function can now be calculated by contracting all 4-index tensors X^{ij} arranged on a square lattice in such a way that, e.g., the indices l, r, u, d of X^{ij} are contracted with the indices r, l, d, u of the respective tensors $X^{i,j-1}, X^{i,j+1}, X^{i-1,j}, X^{i+1,j}$. In order to determine the expectation value of a general operator of the form $O(\{x^{ij}\}) = Z \prod_{ij} O^{ij}(x^{ij})$, one just has to replace each tensor X^{ij} by

$$X^{ij}_{lrud}\left(O^{ij}\right) = \sum_{x=1}^{n} O^{ij}(x)f^{ij}_{\downarrow d}(x)g^{i-1,j}_{\downarrow u}(x)f^{ij}_{\rightarrow r}(x)g^{i,j-1}_{\rightarrow l}.$$

2.2 1–D quantum systems

We consider the partition function of an inhomogeneous 1–D quantum system composed of L n-level systems,

$$Z = \operatorname{tr}\exp\left(-\beta H\right).$$

It is always possible to write the Hamiltonian H as a sum $H = \sum_k H_k$ with each part consisting of a sum of commuting terms. Let us, for simplicity, assume that $H = H_1 + H_2$ and that only local and 2-body nearest neighbor interactions occur, i.e. $H_k = \sum_i O_k^{i,i+1}$ and $\left[O_k^{i,i+1}, O_k^{j,j+1}\right] = 0$, with $i, j = 1, \ldots, L$. The more general case can be treated in a similar way. Let us now consider a decomposition

$$\exp\left(-\frac{\beta}{M}O_k^{i,i+1}\right) = \sum_{\alpha=1}^{\kappa} \hat{S}_{k\alpha}^i \otimes \hat{T}_{k\alpha}^{i+1}. \tag{2.1}$$

The singular value decomposition guarantees the existence of such an expression with $\kappa \leq n^2$. As we will see later, a smart choice of $H = \sum_k H_k$ can typically decrease κ drastically. Making use of the Suzuki–Trotter formula [2]

$$Z = \mathrm{Tr}\left(\prod_k \exp\left(-\frac{\beta}{M}H_k\right)\right)^M + \mathrm{O}\left[\frac{1}{M}\right]$$

it can be readily seen that the partition function can again be calculated by contracting a collection of 4-index tensors X^{ij} defined as

$$X_{(ll')(rr')ud}^{ij} \equiv \left[\hat{T}_{1l}^j \hat{S}_{1r}^j \hat{T}_{2l'}^j \hat{S}_{2r'}^j\right]_{[ud]},$$

where the indices (l, l') and (r, r') are combined to yield a single index that may assume values ranging from 1 to κ^2. Note that now the tensors X^{ij} and $X^{i'j}$ coincide, and that the indices u of the first and d of the last row have to be contracted with each other as well, which corresponds to a classical spin system with periodic boundary conditions in the vertical direction. A general expectation value of an operator of the form $O = ZO^1 \otimes \cdots \otimes O^N$ can also be reexpressed as a contraction of tensors with the same structure: it is merely required to replace each tensor X^{1j} in the first row by

$$X_{(ll')(rr')ud}^{1j}\left(O^j\right) = \left[O^j\hat{T}_{1l}^j \hat{S}_{1r}^j \hat{T}_{2l'}^j \hat{S}_{2r'}^j\right]_{[ud]}.$$

2.3 Tensor contraction

In the following, we use the techniques that were originally developed in the context of PEPS in order to contract the tensors X^{ij} introduced above in a controlled way. The main idea is to express the objects resulting from the

---

[2]Note that in practice, it will be desirable to use the higher order versions of the Trotter decomposition.

contraction of tensors along the first and last column in the 2–D configuration as matrix product states (MPS) and those obtained along the columns $2, 3, \ldots, L-1$ as matrix product operators. More precisely, we define

$$
\langle \, \mathbb{X}^1 \, | \; := \; \sum_{r_1 \ldots r_M = 1}^{m} \mathrm{tr} \left(X_{r_1}^{11} \ldots X_{r_M}^{M1} \right) \langle \, r_1 \ldots r_M \, |
$$

$$
| \, \mathbb{X}^L \, \rangle \; := \; \sum_{l_1 \ldots l_M = 1}^{m} \mathrm{tr} \left(X_{l_1}^{1L} \ldots X_{l_M}^{ML} \right) | \, l_1 \ldots l_M \, \rangle
$$

$$
\mathbb{X}^j \; := \; \sum_{l_1, r_1, \ldots = 1}^{m} \mathrm{tr} \left(X_{l_1 r_1}^{1j} \ldots X_{l_M r_M}^{Mj} \right) | \, l_1 \ldots \rangle \langle \, r_1 \ldots \, |,
$$

where $m = n$ for 2–D classical systems and $m = \kappa^2$ for 1–D quantum systems. These MPS and MPOs are associated to a chain of M m–dimensional systems and their virtual dimension amounts to $D = n$. Note that for 2–D classical systems the first and last matrices under the trace in the MPS and MPO reduce to vectors. The partition function (and similarly other correlation functions) reads $Z = \langle \, \mathbb{X}^1 \, | \, \mathbb{X}^2 \cdots \mathbb{X}^{L-1} | \, \mathbb{X}^L \, \rangle$. Evaluating this expression iteratively by calculating step by step $\langle \, \mathbb{X}^j \, | := \langle \, \mathbb{X}^{j-1} \, | \, \mathbb{X}^j$ for $j = 2, \ldots, L-1$ fails because the virtual dimension of the MPS $\langle \, \mathbb{X}^j \, |$ increases exponentially with j. A way to circumvent this problem is to replace in each iterative step the MPS $\langle \, \mathbb{X}^j \, |$ by a MPS $\langle \, \tilde{\mathbb{X}}^j \, |$ with a reduced virtual dimension $\tilde{D}$ that approximates the state $\langle \, \mathbb{X}^j \, |$ best in the sense that the norm $\delta K :=$ $\| \langle \, \mathbb{X}^j \, | - \langle \, \tilde{\mathbb{X}}^j \, | \|$ is minimized. Due to the fact that this cost function is multiquadratic in the variables of the MPS, this minimization can be carried out very efficiently; the exponential increase of the virtual dimension can hence be prevented and the iterative evaluation of Z becomes tractable, such that an approximation to the partition function can be obtained from $Z \simeq$ $\langle \, \tilde{\mathbb{X}}^{L-1} \, | \, \mathbb{X}^L \, \rangle$. The accuracy of this approximation depends only on the choice of the reduced dimension $\tilde{D}$ and the approximation becomes exact for $\tilde{D} \geq$ D^L. As the norm δK can be calculated at each step, $\tilde{D}$ can be increased dynamically if the obtained accuracy is not large enough. In the worst case scenario, such as in the NP-complete Ising spin glasses [5], $\tilde{D}$ will probably have to grow exponentially in L for a fixed precision of the partition function. But in less pathological cases it seems that $\tilde{D}$ only has to grow polynomially in L; indeed, the success of the methods developed by Nishino [105] in the translational invariant case indicate that even a constant $\tilde{D}$ will produce very reliable results.

Chapter 3

Applications

3.1 Classical Ising Model in two Dimensions

The 2–D Ising model on a $L \times L$ lattice is one of very few nontrivial classical problems that is exactly solvable and shows a phase transition [112, 70, 138]. It is described by the Hamiltonian $H = J \sum_{<i,j>} s_i s_j$, where $s_i = \pm 1$. We have used this model as a first benchmark for our algorithm by comparing the exact solution for the free energy to our numerical results. The outcomes for the special case of a 50×50–lattice, antiferromagnetic coupling ($J = 1$) and periodic boundary conditions can be gathered from fig. 3.1. In this figure, numerical results for $\tilde{D} = 2$ and $\tilde{D} = 8$ are shown. From the inset, it can be gathered that the error of these results is maximal at the critical temperature $k_B T_c / J \sim 2.2692$ at which the phase transition takes place. At this temperature, the error is of order 10^{-2} for $\tilde{D} = 2$ and decreases significantly for $\tilde{D} = 8$.

3.2 Interacting Bosons in a 1–D Optical Lattice

A system of trapped bosonic particles in a 1–D optical lattice of L sites is described by the Bose-Hubbard Hamiltonian [66]

$$H = -J \sum_{i=1}^{L-1} (a_i^\dagger a_{i+1} + h.c.) + \frac{U}{2} \sum_{i=1}^{L} \hat{n}_i (\hat{n}_i - 1) + \sum_{i=1}^{L} V_i \hat{n}_i,$$

where $a_i^\dagger$ and a_i are the creation and annihilation operators on site i and $\hat{n}_i = a_i^\dagger a_i$ is the number operator. This Hamiltonian describes the interplay
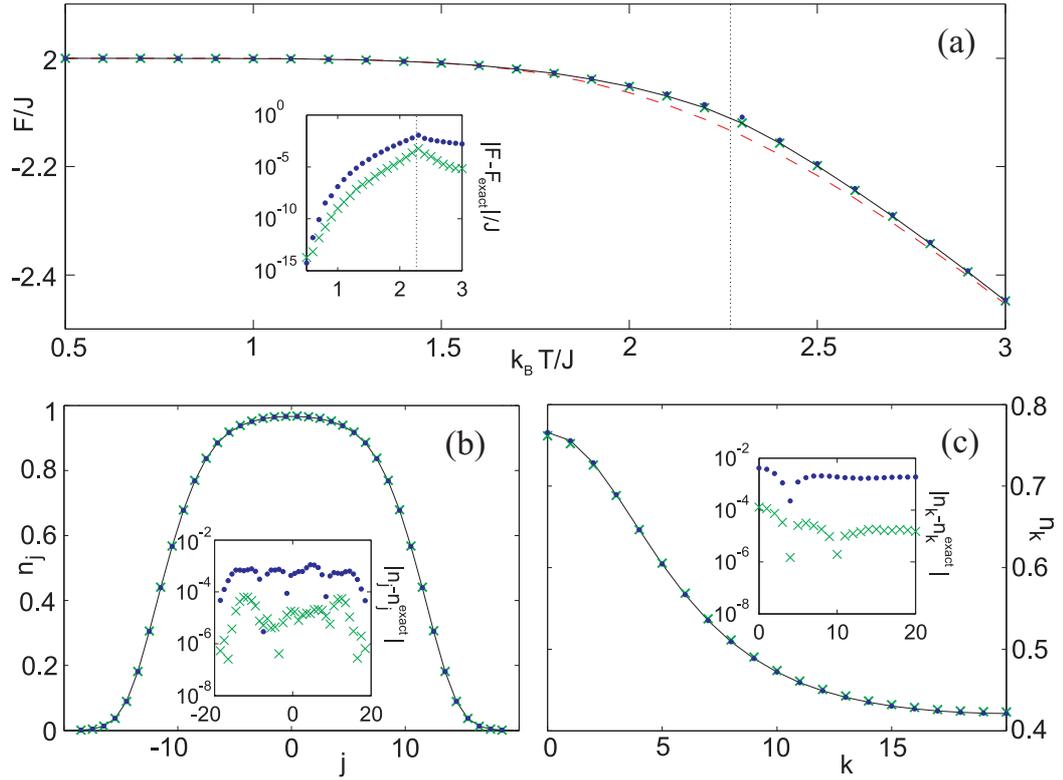
Figure 3.1: (a) Free energy of the 2–D Ising model ($J = 1$) on a 50×50–lattice. (b) and (c): Density and (quasi)-momentum distribution in the Tonks-Girardeau gas limit, plotted for $\beta J = 1$, $L = 40$, $N = 21$ and $V_0/J = 0.034$. In all parts, the numerical results for $\tilde{D} = 2$ ($\tilde{D} = 8$) are represented by dots (crosses) and the exact solution is illustrated by the solid line. From the insets, the error of the numerical results can be gathered. For comparison, in (a) the exact solution for the infinite–lattice case is also plotted (dashed line).

between the kinetic energy due to the next-neighbor hopping with amplitude J and the repulsive on-site interaction U of the particles. The last term in the Hamiltonian models the harmonic confinement of magnitude $V_i = V_0(i - i_0)^2$. The variation of the ratio U/J drives a phase-transition between the Mott-insulating and the superfluid phase, characterized by localized and delocalized particles respectively [42]. Experimentally, the variation of U/J can be realized by tuning the depth of the optical lattice [66, 12]. On the other hand, one typically measures directly the momentum distribution by letting the atomic gas expand and then measuring the density distribution. Thus, we will be mainly interested here in the (quasi)–momentum distribution

$$n_k = \frac{1}{L} \sum_{r,s=1}^{L} \langle a_r^\dagger a_s \rangle e^{i2\pi k(r-s)/L}.$$

Our goal is now to study with our numerical method the finite-temperature properties of this system for different ratios U/J. We thereby assume that the system is in a thermal state corresponding to a grand canonical ensemble with chemical potential μ, such that the partition function is obtained as $Z = \text{tr}\, e^{-\beta(H-\mu\hat{N})}$. Here, $\hat{N} = \sum_{i=1}^{L} \hat{n}_i$ represents the total number of particles. For the numerical study, we assume a maximal particle–number q per lattice site, such that we can project the Hamiltonian H on the subspace spanned by Fock-states with particle-numbers per site ranging from 0 to q. The projected Hamiltonian $\tilde{H}$ then describes a chain of L spins, with each spin acting on a Hilbert-space of dimension $n = q + 1$. A Trotter decomposition that turned out to be advantageous for this case is

$$e^{-\beta(\tilde{H}-\mu\hat{N})} = \left(\hat{V}^\dagger \hat{V} \right)^M + \text{O}\left[\frac{1}{M^2} \right], \tag{3.1}$$

with $\tilde{H} = H_R + H_S + H_T$, $H_R = -\frac{J}{2} \sum_{i=1}^{L-1} R^{(i)} R^{(i+1)}$, $H_S = -\frac{J}{2} \sum_{i=1}^{L-1} S^{(i)} S^{(i+1)}$, $H_T = \sum_{i=1}^{L} T^{(i)}$, $R^{(i)} = \tilde{a}_i^\dagger + \tilde{a}_i$, $S^{(i)} = -i(\tilde{a}_i^\dagger - \tilde{a}_i)$, $T^{(i)} = \frac{1}{2}\tilde{n}_i(\tilde{n}_i - 1) + V_i \tilde{n}_i$ and $\hat{V} = e^{-\frac{\beta}{2M}H_R} e^{-\frac{\beta}{2M}H_S} e^{-\frac{\beta}{2M}(H_T-\mu\hat{N})}$. $\tilde{a}_i^\dagger$, $\tilde{a}_i$ and $\tilde{n}_i$ thereby denote the projections of the creation, the annihilation and the number operators $a_i^\dagger$, a_i and n_i on the q-particle subspace. The decomposition (2.1) of all two-particle operators in expression (3.1) then straightforwardly leads to a set of 4-index tensors X_{lrud}^{ij}, with indices l and r ranging from 1 to $(q+1)^3$ and indices u and d ranging from 1 to $q + 1$. Note that the typical second order Trotter decomposition with $H = H_{\text{even}} + H_{\text{odd}}$ would make the indices l and r range from 1 to $(q+1)^6$.

Let us start out by considering the limit $U/J \to \infty$ in which double occupation of single lattice sites is prevented and the particles in the lattice form
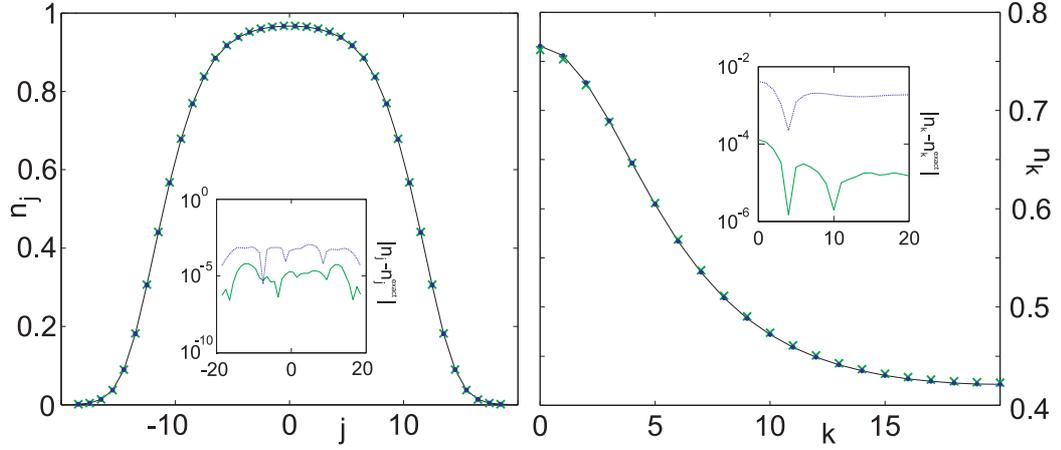
Figure 3.2: Density and (quasi)-momentum distribution in the Tonks-Girardeau gas limit, plotted for $\beta J = 1$, $L = 40$, $N = 21$ and $V_0/J = 0.034$. The dots (crosses) represent the numerical results for $\tilde{D} = 2$ ($\tilde{D} = 8$) and the solid line illustrates the exact results. From the insets, the error of the numerical results can be gathered.

a Tonks–Girardeau gas [115]. In this limit, the Bose-Hubbard Hamiltonian maps to the Hamiltonian of the exactly solvable (inhomogeneous) XX-model, which allows to benchmark our algorithm. The comparison of our numerical results to the exact results can be gathered from fig. 3.2. Here, the density and the (quasi)-momentum distribution are considered for the special case $\beta J = 1$, $L = 40$, $N = 21$ and $V_0/J = 0.034$. The numerical results shown have been obtained for Trotter-number $M = 10$ and two different reduced virtual dimensions $\tilde{D} = 2$ and $\tilde{D} = 8$. The norm δK was of order 10^{-4} for $\tilde{D} = 2$ and 10^{-6} for $\tilde{D} = 8$ [1]. From the insets, it can be gathered that the error of the numerical calculations is already very small for $\tilde{D} = 2$ (of order 10^{-3}) and decreases significantly for $\tilde{D} = 8$. This error can be decreased further by increasing the Trotter-number M.

As the ratio U/J becomes finite, the system becomes physically more interesting, but lacks an exact mathematical solution. In order to judge the reliability of our numerical solutions in this case, we check the convergence with respect to the free parameters of our algorithm (q, $\tilde{D}$ and M). As an illustration, the convergence with respect to the parameter q is shown in figure 3.3. In this figure, the density and the (quasi)-momentum distribution are plotted for $q = 2, 3$ and 4. We thereby assume that $\beta J = 1$, $L = 40$ and

---

[1]We note that we have stopped our iterative algorithm at the point the variation of δK was less than 10^{-8}.

$N = 21$ and consider interaction strengths $U/J = 4$ and 8. The harmonic potential V_0 is chosen in a way to describe Rb-atoms in a harmonic trap of frequency Hz (along the lines of [115]). We note that we have taken into account that changes of the ratio U/J are obtained from changes in both the on-site interaction U and the hopping amplitude J due to variations of the depth of the optical lattice. The numerical calculations have been performed with $M = 10$ and $\tilde{D} = q + 1$. From the figure it can be gathered that convergence with respect to q is achieved for $q \geq 3$.

We now use our numerical algorithm to study a physical property of interacting bosons in an optical lattice, namely the full width at half maximum (FWHM) of the (quasi)-momentum distribution. It has been predicted that the FWHM shows a kink at zero temperature [76, 167, 120]. This kink is an indication for a Mott-superfluid transition, since the FWHM is directly related to the inverse correlation length. Experiments have also revealed this kink [75, 145]; they are, however, performed at finite temperature, something we can study with our algorithm. In figure 3.4, we plot the numerical results for the FWHM as a function of U/J for three different (inverse) temperatures $\beta J = 0.5, 1$ and 2. The physical parameters L, N and V_0 are thereby chosen as in the previous case. The numerical results have been obtained for $M = 10$, $q = 4$ and $\tilde{D} = q + 1$. For each temperature, three different regions can be distinguished: the superfluid region with constant FWHM, the Mott-region with linearly increasing FWHM and an intermediate region in which both phases coexist. The value U/J at which the Mott-region starts increases with increasing temperature, which is consistent with the criteria $U \gg k_B T, J$ for the appearance of the Mott-phase. This behaviour could be easily observed in present experiments.
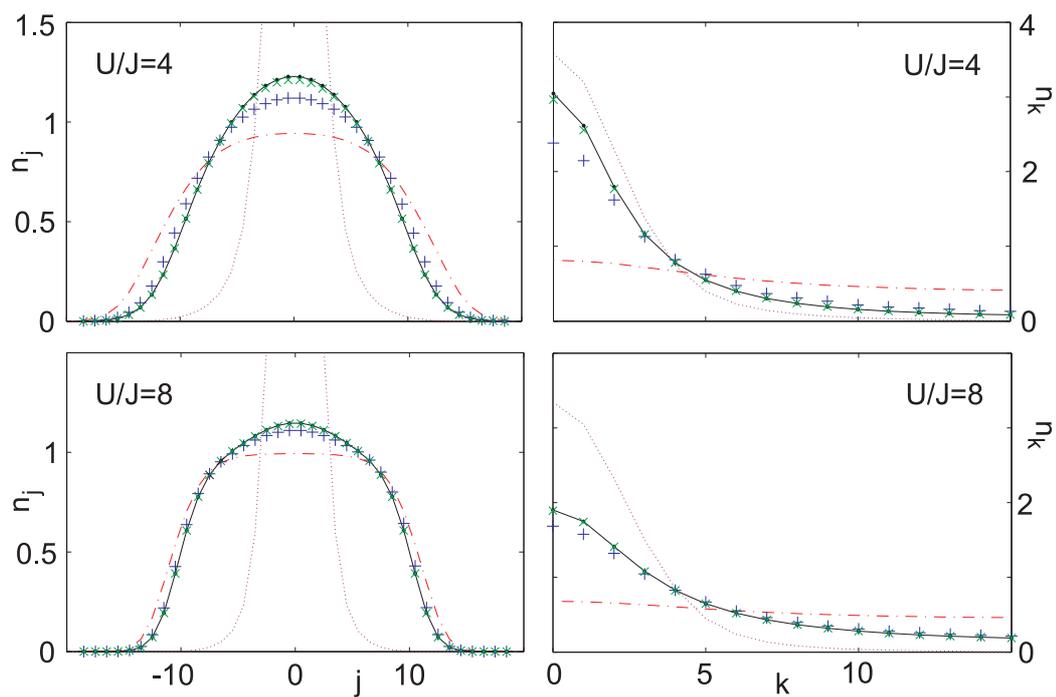
Figure 3.3: Density and (quasi)-momentum distributions for interaction strengths $U/J = 4$ and 8. Here, $\beta J = 1$, $L = 40$, $N = 21$ and $M = 10$. Numerical results were obtained for $q = 2$ (plus-signs), $q = 3$ (crosses) and $q = 4$ (solid line). For comparison, the distributions for $U/J = 0$ (dotted lines) and $U/J \to \infty$ (dash-dotted lines) are also included.
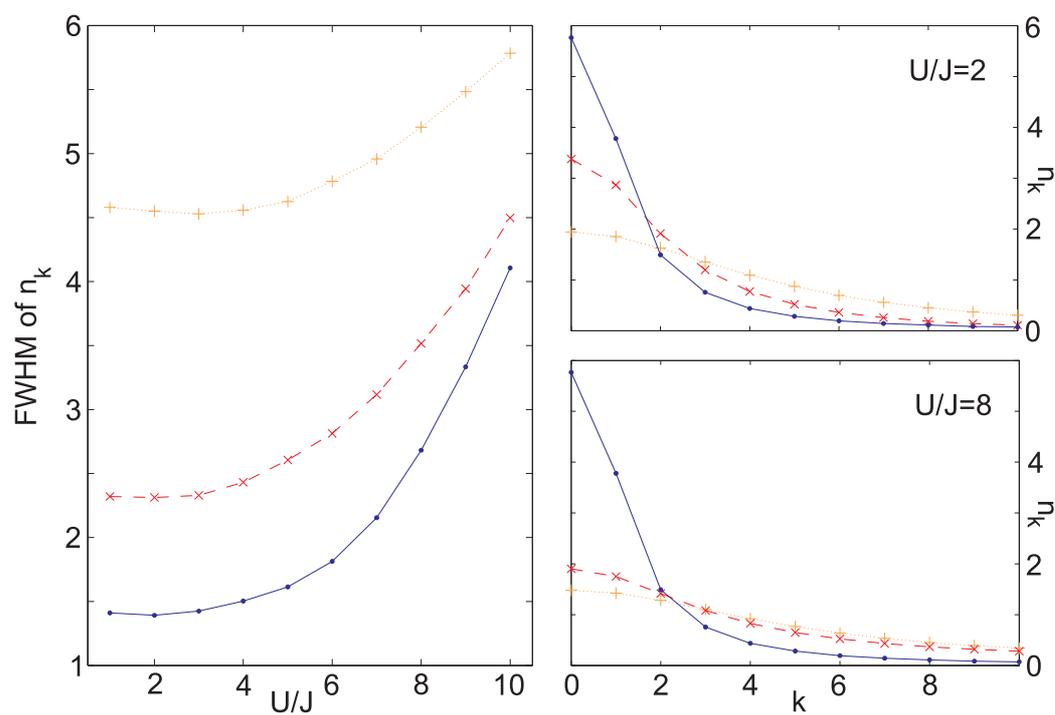
Figure 3.4: FWHM of the (quasi)-momentum distribution as a function of U/J, calculated for temperatures $\beta J = 0.5$ (plus-sign),$\beta J = 1$ (crosses) and $\beta J = 2$ (dots). The corresponding (quasi)-momentum distributions for $U/J = 2$ and $U/J = 8$ are illustrated in the plots at the right-hand side.

Chapter 4

Simulation of higher–dimensional quantum Systems

In this chapter, we present a natural generalization of the 1D MPS to two and higher dimensions and build simulation techniques based on those states which effectively extend DMRG to higher dimensions. We call those states *projected entangled–pair states* (PEPS) [154, 101], since they can be understood in terms of pairs of maximally entangled states of some auxiliary systems that are locally projected in some low–dimensional subspaces. This class of states includes the generalizations of the 2D AKLT-states known as tensor product states [62, 108, 106, 107, 104, 91, 152] which have been used for 2D problems but is much broader since every state can be represented as a PEPS (as long as the dimension of the entangled pairs is large enough). We also develop an efficient algorithm to calculate correlation functions of these PEPS, and which allows us to extend the 1D algorithms to higher dimensions. This leads to many interesting applications, such as scalable variational methods for finding ground or thermal states of spin systems in higher dimensions as well as to simulate their time-evolution. For the sake of simplicity, we will restrict to a square lattice in 2D. The generalization to higher dimensions and other geometries is straightforward.

4.1 Construction and calculus of PEPS

There have been various attempts at using the ideas developed in the context of the numerical renormalization group and DMRG to simulate 2-D quantum spin systems. However, in hindsight it is clear why those methods were never
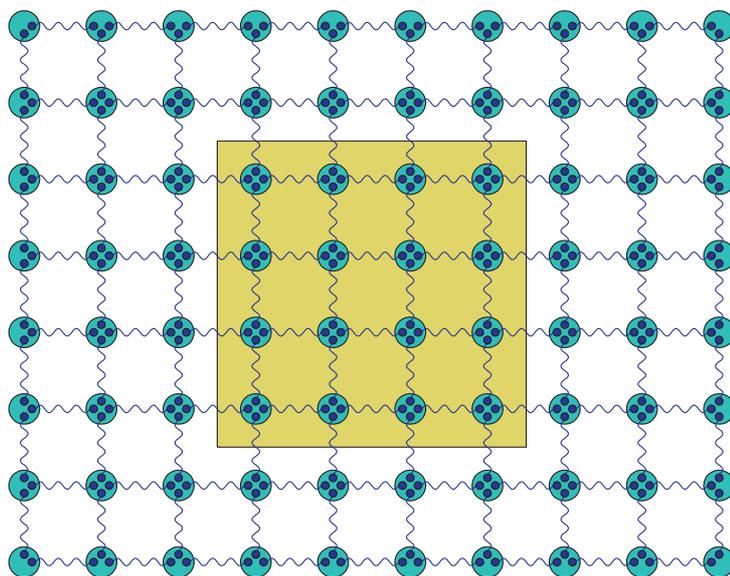
Figure 4.1: Representation of a quantum spin system in 2 dimensions using the PEPS representation. If we calculate the entropy of a block of spins, then this quantity will obey an area law and scale as the length of the boundary between the block and the rest. PEPS-states are constructed such as to have this property build in.

very successful: they can be reformulated as variational methods within the class of 1-dimensional matrix product states, and the structure of those MPS is certainly not well suited at describing ground states of 2-D quantum spin systems. This can immediately be understood when reconsidering the area law discussed in the introduction (see figure 4.1): if we look at the number of degrees of freedom needed to describe the relevant modes in a block of spins, this has to scale as the boundary of the block, and hence this increases exponentially with the size of that boundary. This means that it is impossible to use a NRG or DMRG approach, where the degrees of freedom are bounded by D.

However, it is straightforward to generalize the MPS-picture to higher dimensions: the main reason of the success of the MPS approach is that it allows to represent very well local properties that are compatible with e.g. the translational symmetry in the system. These strong local correlations are obtained by sharing maximally entangled states between neighbours, and the longer range correlations are basically mediated by the intermediate particles. This is of course a very physical picture, as the Hamiltonian does not force any long-range correlations to exist a priori, and those only come into

$$[A_{11}]^{k_{11}} \!\!-\!\! [A_{12}]^{k_{12}} \!\!-\!\! [A_{13}]^{k_{13}} \!\!-\!\! [A_{14}]^{k_{14}}$$

$$| \qquad | \qquad | \qquad |$$

$$[A_{21}]^{k_{21}} \!\!-\!\! [A_{22}]^{k_{22}} \!\!-\!\! [A_{23}]^{k_{23}} \!\!-\!\! [A_{24}]^{k_{24}}$$

$$| \qquad | \qquad | \qquad |$$

$$[A_{31}]^{k_{31}} \!\!-\!\! [A_{32}]^{k_{32}} \!\!-\!\! [A_{33}]^{k_{33}} \!\!-\!\! [A_{34}]^{k_{34}}$$

$$| \qquad | \qquad | \qquad |$$

$$[A_{41}]^{k_{41}} \!\!-\!\! [A_{42}]^{k_{42}} \!\!-\!\! [A_{43}]^{k_{43}} \!\!-\!\! [A_{44}]^{k_{44}}$$
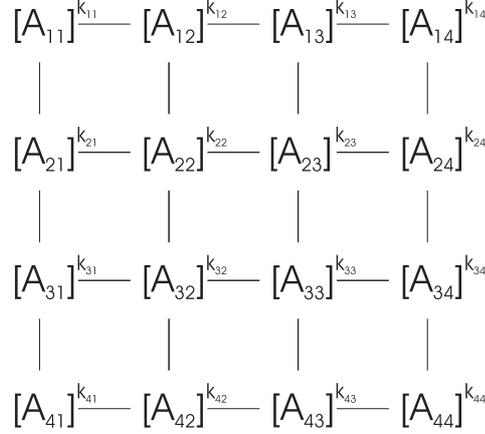
Figure 4.2: Structure of the coefficient related to the state $|\, k_{11}, .., k_{44} \,\rangle$ in the PEPS $|\, \Psi_A \,\rangle$. The bonds represent the indices of the tensors $[A_i]^k$ that are contracted.

existence because of frustration effects. This generalization to higher dimensions can therefore be obtained by distributing virtual maximally entangled states between all neighbouring sites, and as such a generalization of the AKLT-picture is obtained.

More specifically, each physical system at site i is represented by four auxiliary systems a_i, b_i, c_i, and d_i of dimension D (except at the borders of the lattices). Each of those systems is in a maximally entangled state

$$|\, I \,\rangle = \sum_{i=1}^{D} |\, ii \,\rangle$$

with one of its neighbors, as shown in the figure. The PEPS $|\, \Psi \,\rangle$ is then obtained by applying to each site one operator Q_i that maps the four auxiliary systems onto one physical system of dimension d. This leads to a state with coefficients that are contractions of tensors according to a certain scheme. Each of the tensors is related to one operator Q_i according to

$$\left[A_i \right]^{k}_{lrud} = \langle\, k \,|Q_i|\, l, r, u, d \,\rangle$$

and thus associated with one lattice–site i. All tensors possess one physical index k of dimension d and four virtual indices l, r, u and d of dimension D. The scheme according to which these tensors are contracted mimics the underlying lattice structure: the four virtual indices of the tensors are related

to the left, right, upper and lower bond emanating from the corresponding lattice–site. The coefficients of the PEPS are then formed by joining the tensors in such a way that all virtual indices related to same bonds are contracted. This is illustrated in fig. 4.2 for the special case of a 4×4 square lattice. Assuming this contraction of tensors is performed by the function $\mathcal{F}(\cdot)$, the resulting PEPS can be written as

$$| \Psi \rangle = \sum_{k_1,...,k_M=1}^{d} \mathcal{F}\big(\big[A_1 \big]^{k_1}, ..., \big[A_M \big]^{k_M} \big) | k_1, ..., k_M \rangle.$$

This construction can be generalized to any lattice shape and dimension and one can show that any state can be written as a PEPS if we allow the bond dimension to become very large. In this way, we also resolve the problem of the entropy of blocks mentioned before, since now this entropy is proportional to the bonds that connect such block with the rest, and therefore to the area of the block. Note also that, in analogy to the MPS [36], the PEPS are guaranteed to be ground states of local Hamiltonians.

There has recently been a lot of progress in justifying this PEPS picture; M. Hastings has shown [60] that indeed every ground state of a local quantum spin Hamiltonian has an efficient representation in terms of a PEPS, i.e. one whose bond dimension D scales subexponentially with the number of spins under interest. Also, he has shown that all thermal states have an efficient representation in terms of matrix product operators. This is great news, as it basically shows that we have identified the relevant manifold describing the low-energy physics of quantum spin systems. This can lead to many applications in theoretical condensed matter physics, as the questions about the possibility of some exotic phase of matter can now be answered by looking at the set of PEPS hence skipping the bottleneck of simulation of ground states.

The family of PEPS also seems to be very relevant in the field of quantum information theory. For example, all quantum error-correcting codes such as Kitaev's toric code [74] exhibiting topological quantum order have a very simple and exact description in terms of PEPS. Furthermore, the PEPS-picture has been used to show the equivalence between different models of quantum computation [137]; more specifically, the so-called cluster states [123] have a simple interpretation in terms of PEPS, and this picture demystifies the inner workings of the one-way quantum computer.
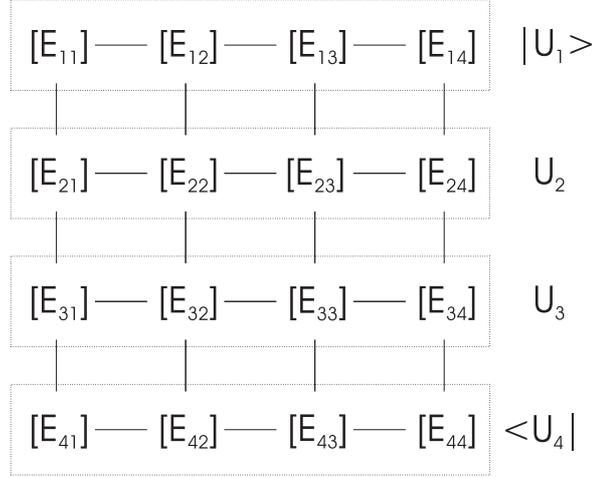
Figure 4.3: Structure of the contractions in $\langle\,\Psi_A\,|\,\Psi_A\,\rangle$. In this scheme, the first and last rows can be interpreted as MPS $|\,U_1\,\rangle$ and $\langle\,U_4\,|$ and the rows in between as MPO U_2 and U_3. The contraction of all tensors is then equal to $\langle\,U_4\,|U_3U_2|\,U_1\,\rangle$.

4.2 Calculus of PEPS

We now show how to determine expectation values of operators in the state $|\,\Psi\,\rangle$. We consider a general operator $O = \prod_i O_i$ and define the $D^2 \times D^2 \times D^2 \times D^2$–tensors

$$\left[E_j^{O_j}\right]_{(ll')(rr')}^{(uu')(dd')} = \sum_{k,k'=1}^{d} \langle\,k\,|O_j|\,k'\,\rangle\left[A_j^*\right]_{lrud}^{k'}\left[A_j\right]_{l'r'u'd'}^{k}.$$

In this definition, the symbols (ll'), (rr'), (uu') and (dd') indicate composite indices. We may interpret the 4 indices of this tensor as being related to the 4 bonds emanating from site j in the lattice. Then, $\langle\,\Psi\,|O|\,\Psi\,\rangle$ is formed by joining all tensors $E_j^{O_j}$ in such a way that all indices related to same bonds are contracted – as in the case of the coefficients of PEPS. These contractions have a rectangular structure, as depicted in fig. 4.3. In terms of the function $\mathcal{F}(\cdot)$, the expectation value reads

$$\langle\,\Psi\,|O|\,\Psi\,\rangle = \mathcal{F}\big(E_1^{O_1}, ..., E_N^{O_N}\big).$$

The contraction of all tensors $E_j^{O_j}$ according to this scheme requires a number of steps that scales exponentially with N – and makes calculations intractable

as the system grows larger. Because of this, an approximate method has to be used to calculate expectation values.

The approximate method suggested in [154] is based on matrix product states (MPS) and matrix product operators (MPO). The main idea is to interpret the first and last row in the contraction–scheme as MPS and the rows in between as MPO. The horizontal indices thereby form the virtual indices and the vertical indices are the physical indices. Thus, the MPS and MPO have both virtual dimension and physical dimension equal to D^2. Explicitly written, the MPS read

$$|U_1\rangle = \sum_{\tilde{d}_1,...,\tilde{d}_L=1}^{D^2} \mathrm{tr}\Big(\big[E_{11}^{O_{11}}\big]^{1\tilde{d}_1}\cdots\big[E_{1L}^{O_{1L}}\big]^{1\tilde{d}_L}\Big)|\tilde{d}_1,...,\tilde{d}_L\rangle$$

$$\langle U_L| = \sum_{\tilde{u}_1,...,\tilde{u}_L=1}^{D^2} \mathrm{tr}\Big(\big[E_{L1}^{O_{L1}}\big]^{\tilde{u}_1 1}\cdots\big[E_{LL}^{O_{LL}}\big]^{\tilde{u}_L 1}\Big)\langle\tilde{u}_1,...,\tilde{u}_L|$$

and the MPO at row r is

$$U_r = \sum_{\substack{\tilde{u}_1,...,\tilde{u}_L=1 \\ \tilde{d}_1,...,\tilde{d}_L=1}}^{D^2} \mathrm{tr}\Big(\big[E_{r1}^{O_{r1}}\big]^{\tilde{u}_1\tilde{d}_1}\cdots\big[E_{rL}^{O_{rL}}\big]^{\tilde{u}_L\tilde{d}_L}\Big)|\tilde{u}_1,...,\tilde{u}_L\rangle\langle\tilde{d}_1,...,\tilde{d}_L|.$$

In terms of these MPS and MPO, the expectation value is a product of MPO and MPS:

$$\langle\Psi|O|\Psi\rangle = \langle U_L|U_{L-1}\cdots U_2|U_1\rangle$$

The evaluation of this expression is, of course, intractable. With each multiplication of a MPO with a MPS, the virtual dimension increases by a factor of D^2. Thus, after L multiplications, the virtual dimension is D^{2L} – which is exponential in the number of rows. The expression, however, reminds of the time–evolution of a MPS [156, 29, 161]. There, each multiplication with a MPO corresponds to one evolution–step. The problem of the exponential increase of the virtual dimension is circumvented by restricting the evolution to the subspace of MPS with a certain virtual dimension $\tilde{D}$. This means that after each evolution–step the resulting MPS is approximated by the "nearest" MPS with virtual dimension $\tilde{D}$. This approximation can be done efficiently, as shown in [156]. In this way, also $\langle\Psi|O|\Psi\rangle$ can be calculated efficiently: first, the MPS $|U_2\rangle$ is formed by multiplying the MPS $|U_1\rangle$ with MPO U_2. The MPS $|U_2\rangle$ is then approximated by $|\tilde{U}_2\rangle$ with virtual dimension $\tilde{D}$. In this fashion the procedure is continued until $|\tilde{U}_{L-1}\rangle$ is obtained. The expectation value $\langle\Psi|O|\Psi\rangle$ is then simply

$$\langle\Psi|O|\Psi\rangle = \langle U_L|\tilde{U}_{L-1}\rangle.$$

Interestingly enough, this method to calculate expectation values can be adopted to develop very efficient algorithms to determine the ground states of 2D Hamiltonians and the time evolution of PEPS by extenting DMRG and the time evolution schemes to 2D.

4.3   Variational method with PEPS

Let us start with an algorithm to determine the ground state of a Hamiltonian with short range interactions on a square $L \times L$ lattice. The goal is to determine the PEPS $|\Psi\rangle$ with a given dimension D which minimizes the energy:

$$\langle H \rangle = \frac{\langle\, \Psi\, |H|\, \Psi\, \rangle}{\langle\, \Psi\, |\, \Psi\, \rangle} \tag{4.1}$$

Following [157], the idea is to iteratively optimize the tensors A_i one by one while fixing all the other ones until convergence is reached. The crucial observation is the fact that the exact energy of $|\Psi\rangle$ (and also its normalization) is a quadratic function of the components of the tensor A_i associated with *one* lattice site i. Because of this, the optimal parameters A_i can simply be found by solving a generalized eigenvalue problem.

The challenge that remains is to calculate the matrix–pair for which the generalized eigenvalues and eigenvectors shall be obtained. In principle, this is done by contracting all indices in the expressions $\langle\, \Psi\, |O|\, \Psi\, \rangle$ and $\langle\, \Psi\, |\, \Psi\, \rangle$ except those connecting to A_i. By interpreting the tensor A_i as a dD^4–dimensional vector $\boldsymbol{A}_i$, these expressions can be written as

$$\langle\, \Psi\, |O|\, \Psi\, \rangle = \boldsymbol{A}_i^\dagger \mathcal{H}_i \boldsymbol{A}_i \tag{4.2}$$

$$\langle\, \Psi\, |\, \Psi\, \rangle = \boldsymbol{A}_i^\dagger \mathcal{N}_i \boldsymbol{A}_i. \tag{4.3}$$

Thus, the minimum of the energy is attained by the generalized eigenvector $\boldsymbol{A}_i$ of the matrix–pair $(\mathcal{H}_i, \mathcal{N}_i)$ to the minimal eigenvalue μ:

$$\mathcal{H}_i \boldsymbol{A}_i = \mu \mathcal{N}_i \boldsymbol{A}_i$$

It turns out that the matrix–pair $(\mathcal{H}_i, \mathcal{N}_i)$ can be efficiently evaluated by the method developed for the calculation of expectation values: $\mathcal{N}_i$ relies on the contraction of all but one tensors E_j^I (with I denoting the identity) according to the same rectangular scheme as before. The one tensor that has to be omitted is E_i^I – the tensor related to site i. Assuming this contraction is performed by the function $\mathcal{G}_i(\cdot)$, $\mathcal{N}_i$ can be written as

$$\left[\mathcal{N}_i\right]_{lrud\ \ k'}^{k\ \ \ l'r'u'd'} = \mathcal{G}_i\big(E_1^I, ..., E_N^I\big)_{lrud}^{l'r'u'd'}\delta_{k'}^k.$$

If we join the indices $(klrud)$ and $(k'l'r'u'd')$, we obtain the $dD^4 \times dD^4$–matrix that fulfills equation (4.3). To evaluate $\mathcal{G}_i(\cdot)$ efficiently, we proceed in the same way as before by interpreting the rows in the contraction–structure as MPS and MPO. First, we join all rows that lie above site i by multiplying the topmost MPS $|U_1\rangle$ with subjacent MPO and reducing the dimension after each multiplication to $\tilde{D}$. Then, we join all rows lying below i by multiplying $\langle U_L|$ with adjacent MPO and reducing the dimension as well. We end up with two MPS of virtual dimension $\tilde{D}$ – which we can contract efficiently with all but one of the tensors E_j^I lying in the row of site i.

The effective Hamiltonian $\mathcal{H}_i$ can be determined in an analogous way, but here the procedure has to be repeated for every term in the Hamiltonian (i.e. in the order of $2N$ times in the case of nearest neighbor interactions). Assuming a single term in the Hamiltonian has the tensor–product structure $H^s \equiv \prod_i h_i^s$, the effective Hamiltonian $\mathcal{H}_i^s$ corresponding to this term is obtained as

$$\left[\mathcal{H}_i^s\right]_{lrud\ k'}^{k\quad l'r'u'd'} = \mathcal{G}_i\left(E_1^{h_1^s}, ..., E_N^{h_N^s}\right)_{lrud}^{l'r'u'd'} \left[h_i^s\right]_{k'}^k.$$

The complete effective Hamiltonian $\mathcal{H}_i$ that fulfills equation (4.2) is then produced as

$$\mathcal{H}_i = \sum_s \mathcal{H}_i^s.$$

Thus, both the matrices $\mathcal{N}_i$ and $\mathcal{H}_i$ are directly related to the expressions $\mathcal{G}_i\left(E_1^I, ..., E_N^I\right)$ and $\mathcal{G}_i\left(E_1^{h_1^s}, ..., E_N^{h_N^s}\right)$. These expressions, however, can be evaluated efficiently using the approximate method introduced before for the calculation of expectation values. Therefore, the optimal A_i can be determined, and one can proceed with the following site, iterating the procedure until convergence.

4.4   Time evolution with PEPS

Let us next move to describe how a time–evolution can be simulated on a PEPS. We will assume that the Hamiltonian only couples nearest neighbors, although more general settings can be considered. The principle of simulating a time–evolution step is as follows: first, a PEPS $|\Psi_A^0\rangle$ with physical dimension $d = 2$ and virtual dimension D is chosen as a starting state. This state is evolved by the time–evolution operator $U = e^{-iH\delta t}$ (we assume $\hbar = 1$) to yield another PEPS $|\Psi_B\rangle$ with a virtual dimension D_B increased by a factor η:

$$|\Psi_B\rangle = U|\Psi_A^0\rangle$$

The virtual dimension of this state is then reduced to D by calculating a new PEPS $|\Psi_A\rangle$ with virtual dimension D that has minimal distance to $|\Psi_B\rangle$. This new PEPS is the starting state for the next time–evolution step. The crucial point in simulating a time–evolution with PEPS is thus the development of an efficient algorithm for reducing the virtual dimension of a PEPS.

Before formulating this algorithm, let us recite how to express the product $U|\Psi_A^0\rangle$ in terms of a PEPS. This is done by means of a Trotter–approximation: first, the interaction–terms in H are classified in *horizontal* and *vertical* according to their orientation and in *even* and *odd* depending on whether the interaction is between even–odd or odd–even rows (or columns). The Hamiltonian can then be decomposed into a *horizontal–even*, a *horizontal–odd*, a *vertical–even* and a *vertical–odd* part:

$$H = H_{he} + H_{ho} + H_{ve} + H_{vo}$$

The single–particle operators of the Hamiltonian can simply be incorporated in one of the four parts (note that different Trotter decompositions are again possible, e.g. grouping all Pauli operators of the same kind in 3 different groups as we discussed earlier, and in some cases this leads to a clear computational advantage). Using the Trotter–approximation, the time–evolution operator U can be written as a product of four evolution–operators:

$$U = e^{-iH\delta t} \approx e^{-iH_{he}\delta t}e^{-iH_{ho}\delta t}e^{-iH_{ve}\delta t}e^{-iH_{vo}\delta t} \qquad (4.4)$$

Since each of the four parts of the Hamiltonian consists of a sum of commuting terms, each evolution–operator equals a product of two–particle operators w_{ij} acting on neighboring sites i and j. These two–particle operators have a Schmidt–decomposition consisting of, say, η terms:

$$w_{ij} = \sum_{\rho=1}^{\eta} u_i^\rho \otimes v_j^\rho$$

One such two–particle operator w_{ij} applied to the PEPS $|\Psi_A^0\rangle$ modifies the tensors A_i^0 and A_j^0 associated with sites i and j as follows: assuming the sites i and j are horizontal neighbors, A_i^0 has to be replaced by

$$\left[B_i\right]_{l(r\rho)ud}^k = \sum_{k'=1}^d \left[u_i^\rho\right]_{k'}^k \left[A_i^0\right]_{lrud}^{k'}$$

and A_j^0 becomes

$$\left[B_j\right]_{(l\rho)rud}^k = \sum_{k'=1}^d \left[v_j^\rho\right]_{k'}^k \left[A_j^0\right]_{lrud}^{k'}.$$

These new tensors have a joint index related to the bond between sites i and j. This joint index is composed of the original index of dimension D and the index ρ of dimension η that enumerates the terms in the Schmidt–decomposition. Thus, the effect of the two–particle operator w_{ij} is to increase the virtual dimension of the bond between sites i and j by a factor of η. Consequently, $e^{-iH_{he}\delta t}$ and $e^{-iH_{ho}\delta t}$ increase the dimension of every second horizontal bond by a factor of η; $e^{-iH_{ve}\delta t}$ and $e^{-iH_{vo}\delta t}$ do the same for every second vertical bond. By applying all four evolution–operators consecutively, we have found an approximate form of the time–evolution operator U that – when applied to a PEPS $|\Psi_A^0\rangle$ – yields another PEPS $|\Psi_B\rangle$ with a virtual dimension multiplied by a constant factor η.

The aim of the approximate algorithm is now to optimize the tensors A_i related to a PEPS $|\Psi_A\rangle$ with virtual dimension D, such that the distance between $|\Psi_A\rangle$ and $|\Psi_B\rangle$ tends to a minimum. The function to be minimized is thus

$$K\big(A_1,...,A_M\big) = \big\|\,|\Psi_A\rangle - |\Psi_B\rangle\big\|^2.$$

This function is non–convex with respect to all parameters $\{A_1,...,A_M\}$. However, due to the special structure of PEPS, it is quadratic in the parameters A_i associated with *one* lattice–site i. Because of this, the optimal parameters A_i can simply be found by solving a system of linear equations. The concept of the algorithm is to do this one–site optimization site-by-site until convergence is reached.

The coefficient matrix and the inhomogeneity of the linear equations system can be calculated efficiently using the method developed for the calculation of expectation values. In principle, they are obtained by contracting all indices in the expressions for the scalar–products $\langle\Psi_A|\Psi_A\rangle$ and $\langle\Psi_A|\Psi_B\rangle$ except those connecting to A_i. By interpreting the tensor A_i as a dD^4-dimensional vector $\boldsymbol{A}_i$, these scalar–products can be written as

$$\langle\Psi_A|\Psi_A\rangle = \boldsymbol{A}_i^\dagger \mathcal{N}_i \boldsymbol{A}_i \qquad (4.5)$$
$$\langle\Psi_A|\Psi_B\rangle = \boldsymbol{A}_i^\dagger \mathcal{W}_i. \qquad (4.6)$$

Since

$$K = \langle\Psi_B|\Psi_B\rangle + \langle\Psi_A|\Psi_A\rangle - 2Re\langle\Psi_A|\Psi_B\rangle,$$

the minimum is attained as

$$\mathcal{N}_i \boldsymbol{A}_i = \mathcal{W}_i.$$

The efficient calculation of $\mathcal{N}_i$ has already been described in the previous section. The scalar product $\langle\Psi_A|\Psi_B\rangle$ and the inhomogeneity $\mathcal{W}_i$ are calculated in an efficient way following the same ideas. First, the $DD_B \times DD_B \times$

$DD_B \times DD_B$–tensors

$$\left[F_j\right]^{(uu')(dd')}_{(ll')(rr')} = \sum_{k=1}^{d} \left[A_j^*\right]^k_{lrud} \left[B_j\right]^k_{l'r'u'd'}$$

are defined. The scalar–product $\langle \Psi_A \,|\, \Psi_B \rangle$ is then obtained by contracting all tensors F_j according to the previous scheme – which is performed by the function $\mathcal{F}(\cdot)$:

$$\langle \Psi_A \,|\, \Psi_B \rangle = \mathcal{F}\big(F_1, ..., F_M\big)$$

The inhomogenity $\mathcal{W}_i$ relies on the contraction of all but one of the tensors F_j, namely the function $\mathcal{G}_i(\cdot)$, in the sense that

$$\left[\mathcal{W}_i\right]^k_{lrud} = \sum_{l'r'u'd'=1}^{D} \mathcal{G}_i\big(F_1, ..., F_M\big)^{l'r'u'd'}_{lrud} \left[B_i\right]^k_{l'r'u'd'}.$$

Joining all indices $(klrud)$ in the resulting tensor leads to the vector of length dD^4 that fulfills equation (4.6). Thus, both the scalar–product $\langle \Psi_A \,|\, \Psi_B \rangle$ and the inhomogenity $\mathcal{W}_i$ are directly related to the expressions $\mathcal{F}\big(F_1, ..., F_M\big)$ and $\mathcal{G}_i\big(F_1, ..., F_M\big)$. These expressions, however, can be evaluated efficiently using the approximate method from before.

Even though the principle of simulating a time–evolution step has been recited now, the implementation in this form is numerically expensive. This is why we append some notes about how to make the simulation more efficient:

1.- Partitioning of the evolution: The number of required numerical operations decreases significantly as one time–evolution step is partitioned into 4 substeps: first the state $|\,\Psi_A^0\,\rangle$ is evolved by $e^{-iH_{vo}\delta t}$ only and the dimension of the increased bonds is reduced back to D. Next, evolutions according to $e^{-iH_{ve}\delta t}$, $e^{-iH_{ho}\delta t}$ and $e^{-iH_{he}\delta t}$ follow. Even though the partitioning increases the number of evolution–steps by a factor of 4, the number of multiplications in one evolution–step decreases by a factor of η^3.

2.- Optimization of the contraction order: Most critical for the efficiency of the numerical simulation is the order in which the contractions are performed. We have optimized the order in such a way that the scaling of the number of multiplications with the virtual dimension D is minimal. For this, we assume that the dimension $\tilde{D}$ that tunes the accuracy of the approximate calculation of $\mathcal{N}_i$ and $\mathcal{W}_i$ is proportional to D^2, i.e. $\tilde{D} = \kappa D^2$. The number of required multiplications is then of order [1] $\kappa^2 D^{10} L^2$ and the required memory scales

---

[1]The scaling D^{10} is obtained when at all steps in the algorithm, a sparse matrix algorithm is used. In particular, we have to use an iterative sparse method for solving the linear set of equations in the approximation step.

as $d\eta\kappa^2 D^8$.

3.- Optimization of the starting state: The number of sweeps required to reach convergence depends on the choice of the starting state for the optimization. The idea for finding a good starting state is to reduce the bonds with increased virtual dimension ηD by means of a Schmidt–decomposition. This is done as follows: assuming the bond is between the horizontal neighboring sites i and j, the contraction of the tensors associated with these sites, B_i and B_j, along the bond i–j forms the tensor

$$\left[\mathcal{M}_{ij}\right]^{k\ \ \ k'}_{lud\ r'u'd'} = \sum_{\rho=1}^{D\eta} \left[B_i\right]^k_{l\rho ud}\left[B_j\right]^{k'}_{\rho r'u'd'}.$$

By joining the indices $(klud)$ and $(k'r'u'd')$, this tensor can be interpreted as a $dD^3 \times dD^3$–matrix. The Schmidt–decomposition of this matrix is

$$\mathcal{M}_{ij} = \sum_{\rho=1}^{dD^3} c_\rho \mathcal{A}_i^\rho \otimes \mathcal{A}_j^\rho$$

with the Schmidt–coefficients c_ρ ($c_\rho \geq 0$) and corresponding matrices $\mathcal{A}_i^\rho$ and $\mathcal{A}_j^\rho$. We can relate these matrices to a new pair of tensors A_i^0 and A_j^0 associated with sites i and j:

$$\begin{aligned}
\left[A_i^0\right]^k_{l\rho ud} &= \sqrt{c_\rho}\left[\mathcal{A}_i^\rho\right]^k_{lud} \\
\left[A_j^0\right]^k_{\rho rud} &= \sqrt{c_\rho}\left[\mathcal{A}_j^\rho\right]^k_{rud}
\end{aligned}$$

The virtual dimension of these new tensors related to the bond between sites i and j is equal to the number of terms in the Schmidt–decomposition. Since these terms are weighted with the Schmidt–coefficients c_ρ, it is justified to keep only the D terms with coefficients of largest magnitude. Then, the contraction of the tensors A_i^0 and A_j^0 along the bond i–j with dimension D yields a good approximation to the true value $\mathcal{M}_{ij}$:

$$\left[\mathcal{M}_{ij}\right]^{k\ \ \ k'}_{lud\ r'u'd'} \approx \sum_{\rho=1}^{D} \left[A_i^0\right]^k_{l\rho ud}\left[A_j^0\right]^{k'}_{\rho r'u'd'}.$$

This method applied to all bonds with increased dimension provides us with the starting state for the optimization.

Chapter 5

Applications

5.1 Hard–Core Bosons in a 2–D Optical Lattice

Let us now illustrate the variational methods with some examples. Models the PEPS algorithms have already been applied to successfully include the Heisenberg antiferromagnet [154] and the Shastry-Sutherland model [64]. In the following, we present the results for the system of hard–core bosons in a 2D optical lattice [101] – which include calculations of ground state properties and studies of the time–evolution after sudden changes in the parameters.

The system of bosons in a 2D optical lattice is characterized by the Bose–Hubbard Hamiltonian

$$H = -J \sum_{<i,j>} \left(a_i^\dagger a_j + h.c. \right) + \frac{U}{2} \sum_i \hat{n}_i (\hat{n}_i - 1) + \sum_i V_i \hat{n}_i,$$

where $a_i^\dagger$ and a_i are the creation and annihilation operators on site i and $\hat{n}_i = a_i^\dagger a_i$ is the number operator. This Hamiltonian describes the interplay between the kinetic energy due to the next-neighbor hopping with amplitude J and the repulsive on-site interaction U of the particles. The last term in the Hamiltonian models the harmonic confinement of magnitude $V_i = V_0(i-i_0)^2$. Since the total number of particles $\hat{N} = \sum_i \hat{n}_i$ is a symmetry of the Hamiltonian, the ground–state will have a fixed number of particles N. We choose this number by appending the term $-\mu \hat{N}$ to the Hamiltonian and tuning the chemical potential μ. The variation of the ratio U/J drives a phase-transition between the Mott-insulating and the superfluid phase, characterized by localized and delocalized particles respectively [42]. Experimentally, the variation of U/J can be realized by tuning the depth of the optical lattice [66, 12]. The quantity that is typically measured is the

momentum distribution. The is done by letting the atomic gas expand and measuring the density distribution of the expanded cloud. Thus, we will be mainly interested here in the (quasi)–momentum distribution

$$n_k = \frac{1}{L^2} \sum_{r,s} \langle a_r^\dagger a_s \rangle e^{i2\pi k \cdot (r-s)/L^2}$$

of the particles.

In the following, we focus on the limit of a hard–core interaction, $U/J \to \infty$. In this limit, two particles are prevented from occupying a single site. This limit is especially interesting in one dimension where the particles form the so–called Tonks-Girardeau gas [51, 115]. The particles in this gas are strongly correlated – which leads to algebraically decaying correlation functions. In two dimensions, the model was studied in detail in [72]. In the hard–core limit, the Bose–Hubbard model is equivalent to a spin–system with XX–interactions described by the Hamiltonian

$$H = -\frac{J}{2} \sum_{<i,j>} \left(\sigma_x^{(i)} \sigma_x^{(j)} + \sigma_y^{(i)} \sigma_y^{(j)} \right) + \frac{1}{2} \sum_i \left(V_i - \mu \right) \sigma_z^{(i)}.$$

Here, $\sigma_x^{(i)}$, $\sigma_y^{(i)}$ and $\sigma_z^{(i)}$ denote the Pauli-operators acting on site i. This Hamiltonian has the structure we can simulate with the algorithm: it describes L^2 physical systems of dimension $d = 2$ on a $L \times L$–square lattice.

5.1.1 Ground state properties

We start with the study the ground–state properties of the system of hard–core bosons for lattice–sizes 4×4 and 11×11. We calculate the ground–state by means of an imaginary time–evolution which we can simulate with the method from before.

We first focus on the 4×4–lattice for which we can calculate the ground–state exactly and are able to estimate the precision of the algorithm by comparison with exact results. In fig. 5.1, the energy is plotted as the system undergoes the imaginary time–evolution. We thereby assume a time–step $\delta t = -i0.03$. We choose the magnitude of the harmonic confinement (in units of the tunneling–constant) $V_0/J = 36$. In addition, we tune the chemical potential to $\mu/J = 3.4$ such that the ground state has particle–number $N = 4$. With this configuration, we perform the imaginary time–evolution both exactly and variationally with PEPS. As a starting state we take a product state that represents a Mott-like distribution with 4 particles arranged in the center of the trap and none elsewhere. The variational calculation is
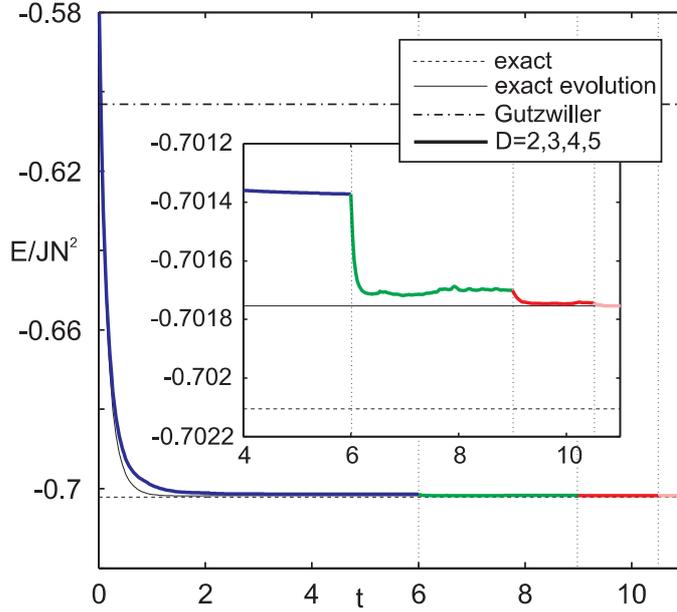
Figure 5.1: Energy as a function of time for the imaginary time–evolution of the system of hard–core bosons on a 4×4–lattice. The evolutions are performed sequentially with PEPS of virtual dimension $D = 2$, $D = 3$, $D = 4$ and $D = 5$. The times at which D is increased are indicated by vertical lines. For comparison, the exact ground state–energy, the exact imaginary time–evolution and the energy of the optimal Gutzwiller ansatz are included.

performed with $D = 2$ first until convergence is reached; then, evolutions with $D = 3$, $D = 4$ and $D = 5$ follow. At the end, a state is obtained that is very close to the state obtained by exact evolution. The difference in energy is $|E_{D=5} - E_{exact}| \simeq 6.4614 \cdot 10^{-5} J$. For comparison, also the exact ground–state energy obtained by an eigenvalue–calculation and the energy of the optimal Gutzwiller ansatz are included in fig. 5.1. The difference between the exact result and the results of the imaginary time–evolution is due to the Trotter–error and is of order $O(\delta t^2)$. The energy of the optimal Gutzwiller-Ansatz is well seperated from the exact ground–state energy and the results of the imaginary time–evolution.

In fig. 5.2, the energy as a function of time is plotted for the imaginary time–evolution on the 11×11–lattice. Again, a time–step $\delta t = -i0.03$ is assumed for the evolution. The other parameters are set as follows: the ratio between harmonic confinement and the tunneling constant is chosen as $V_0/J = 100$ and the chemical potential is tuned to $\mu/J = 3.8$ such that
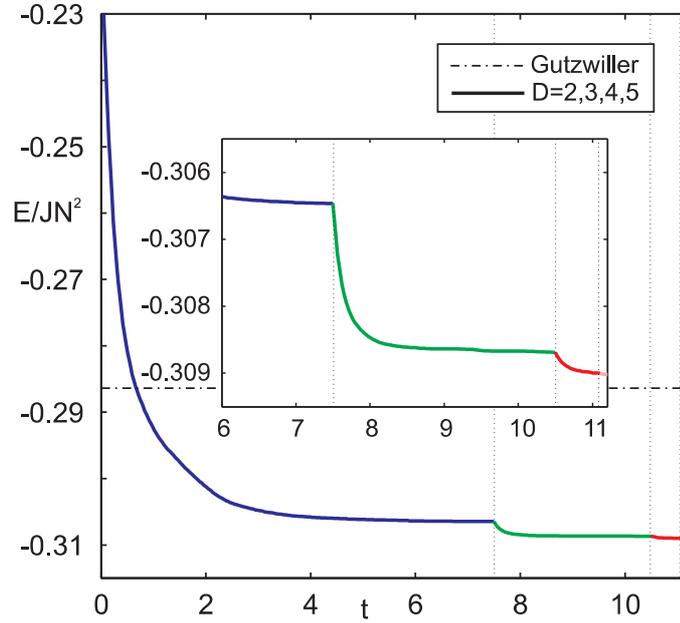
Figure 5.2: Energy as a function of time for the imaginary time–evolution of the system of hard–core bosons on a 11×11–lattice. The evolutions are performed sequentially with PEPS of virtual dimension $D = 2$, $D = 3$, $D = 4$ and $D = 5$. The times at which D is increased are indicated by vertical lines. For comparison, the energy of the optimal Gutzwiller ansatz is included.

the total number of particles N is 14. The starting state for the imaginary time–evolution is, similar to before, a Mott-like distribution with 14 particles arranged in the center of the trap. This state is evolved within the subset of PEPS with $D = 2$, $D = 3$, $D = 4$ and $D = 5$. As can be gathered from the plot, this evolution shows a definite convergence. In addition, the energy of the final PEPS lies well below the energy of the optimal Gutzwiller ansatz.

The difference between the PEPS and the Gutzwiller ansatz becomes more evident as one studies the momentum distribution of the particles. The diagonal slice of the (quasi)–momentum distribution is shown in fig. 5.3. As can be seen, there is a clear difference between the momentum distribution derived from the PEPS and the one from the Gutzwiller ansatz. In contrast, the PEPS and the Gutzwiller ansatz produce a very similar density profile (see inset). The acceptability of the Gutzwiller ansatz is due to the inhomegenity of the system: the different average particle number at each site is the cause for the correlations between different sites. These correlations are, in many cases, good approximations. In contrast, the average particle number
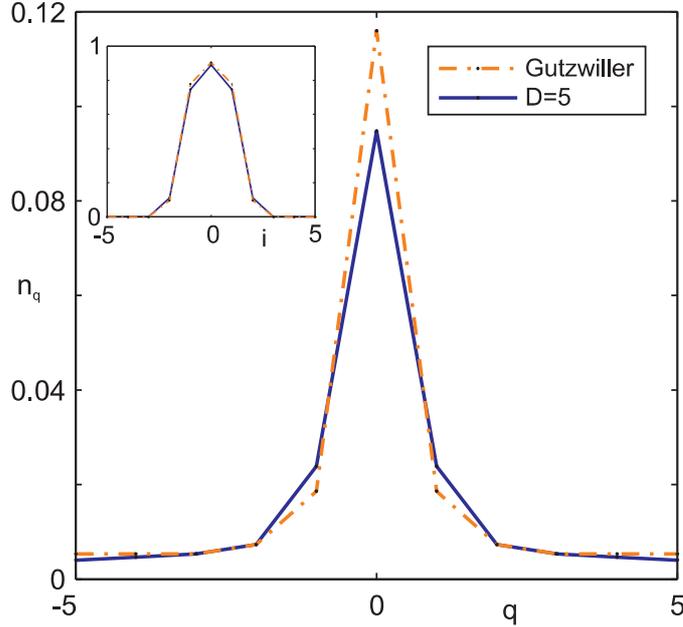
Figure 5.3: (Quasi)–momentum distribution of the particles in the ground state of a 11×11–lattice. Plotted are results of the variational calculations with PEPS of dimension $D = 5$ and with the Gutzwiller ansatz. From the inset, the density of the particles can be gathered.

is constant in homogeneous systems – which leads to correlations that are constant. Thus, the Gutzwiller ansatz is expected to be less appropriate for the study of correlations of homogeneous systems.

5.1.2 Dynamics of the system

We now focus on the study of dynamic properties of hard–core bosons on a lattice of size 11×11. We investigate the responses of this system to sudden changes in the parameters and compare our numerical results to the results obtained by the Gutzwiller ansatz. The property we are interested in is the fraction of particles that are condensed. For interacting and finite systems, this property is measured best by the condensate density ρ which is defined as largest eigenvalue of the correlation–matrix $\langle a_i^\dagger a_j \rangle$.

First, we study the time evolution of the condensate density after a sudden change of the trapping potential. We start with a Gutzwiller–approximation of the ground state in case of a trapping potential of magnitude $V_0/J = 100$. The chemical potential we tune to $\mu/J = 3.8$ to achieve an average
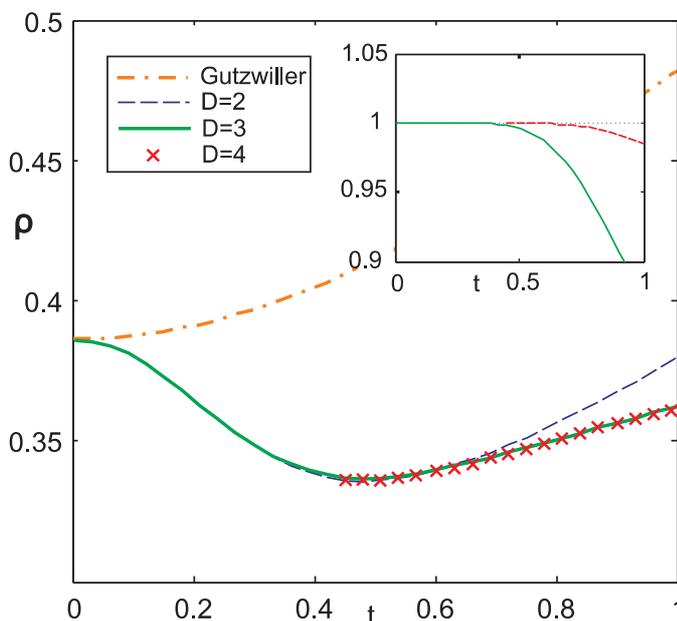
Figure 5.4: Time evolution of the condensate density after a sudden change of the magnitude of the trapping potential from $V_0/J = 100$ to $V_0/J = 64$. As a starting state, we use the Gutzwiller–approximation of the ground state. The evolution is performed on the basis of the Gutzwiller ansatz and PEPS with $D = 2$, $D = 3$ and $D = 4$. From the inset, the overlap between the PEPS with $D = 2$ and $D = 3$ (solid line) and the PEPS with $D = 3$ and $D = 4$ (dashed line) can be gathered.

particle–number of $\langle \hat{N} \rangle = 14$. This state we expose to a trapping potential of magnitude $V_0/J = 64$ and calculate the evolution of the condensate density using the Gutzwiller ansatz and PEPS with $D = 2$, $D = 3$ and $D = 4$. We thereby assume a time–step $\delta t = 0.03$. To assure that our results are accurate, we proceed as follows: first, we perform the simulation using PEPS with $D = 2$ and $D = 3$ until the overlap between these two states falls below a certain value. Then, we continue the simulation using PEPS with $D = 3$ and $D = 4$ as long as the overlap between these two states is close to 1. The results of this calculation can be gathered from fig. 5.4. What can be observed is that the results obtained from using PEPS are qualitatively very different from the result based on the Gutzwiller ansatz. The inset in fig. 5.4 shows the overlap of the $D = 2$ with the $D = 3$–PEPS and the $D = 3$ with the $D = 4$–PEPS.

In fig. 5.5, the time–evolution of the condensate density after a sudden
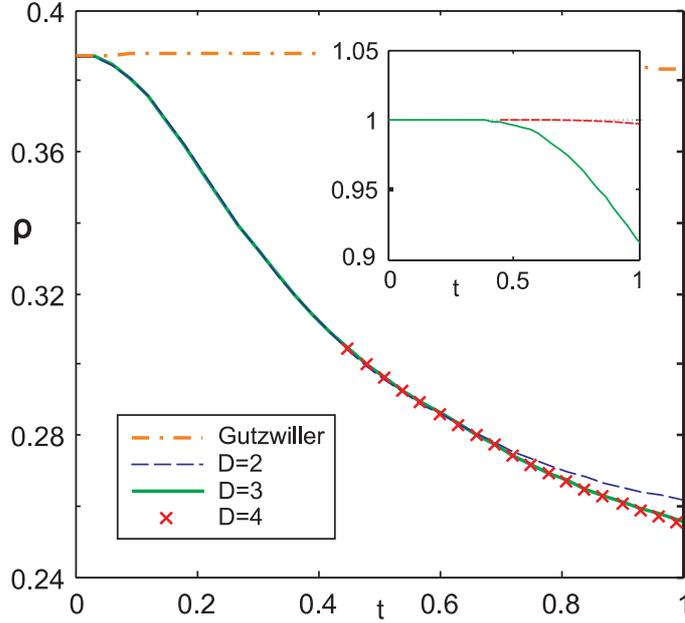
Figure 5.5: Time evolution of the condensate density after a sudden shift of the center of the trap by one site in x– and y–direction. Starting state is the Gutzwiller–approximation of the ground state. The evolution is performed using the Gutzwiller ansatz and PEPS with $D = 2$, $D = 3$ and $D = 4$. The inset shows the overlap between the PEPS with $D = 2$ and $D = 3$ (solid line) and $D = 3$ and $D = 4$ (dashed line).

shift of the trapping potential is plotted. As a starting state, again the Gutzwiller–approximation of the ground state in a trap of magnitude $V_0/J = 100$ is used. This state is evolved with respect to a trapping potential that is shifted by one lattice–site in x– and y–direction. We assume a time–step $\delta t = 0.03$ and tune the chemical potential to $\mu/J = 3.8$. As before, we perform the simulation successively with $D = 2$, $D = 3$ and $D = 4$ and judge the accuracy of the results by monitoring the overlap between PEPS with different Ds. From the plot, it can be gathered that the evolution of the condensate density based on the Gutzwiller ansatz is qualitatively again very different from the evolution obtained from using PEPS. The evolution obtained from using PEPS shows a definite damping. The shift of the trap thus provokes a destruction of the condensate. The evolution based on the Gutzwiller ansatz doesn't show this feature.

As a contrary example, we study the evolution of a Mott-distribution with 14 particles arranged in the center of the trap. We assume $V_0/J = 100$,
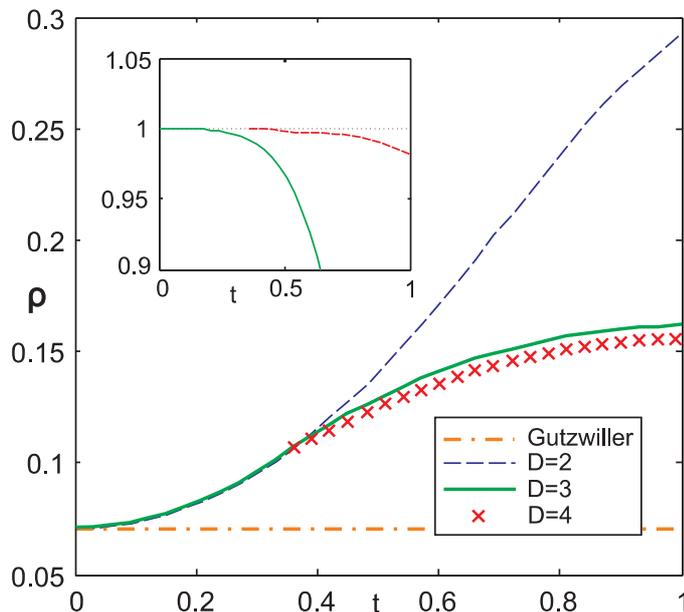
Figure 5.6: Time evolution of the condensate density starting from a Mott–distribution with 14–particles arranged in the center of the trap. The magnitude of the trapping potential is $V_0/J = 100$. For the evolution, the Gutzwiller ansatz and PEPS with $D = 2$, $D = 3$ and $D = 4$ are used. The inset shows the overlap between the $D = 2$ and $D = 3$–PEPS (solid line) and the $D = 3$ and $D = 4$–PEPS (dashed line).

$\mu/J = 3.8$ and $\delta t = 0.03$. We perform the simulation in the same way as before with $D = 2$, $D = 3$ and $D = 4$. In fig. 5.6, the time evolution of the condensate density is plotted. It can be observed that there is a definite increase in the condensate fraction. The Gutzwiller ansatz is in contrast to this result since it predicts that the condensate density remains constant.

5.1.3 Accuracy and performance of the algorithm

Finally, we make a few comments about the accuracy and the performance of the algorithm. One indicator for the accuracy of the algorithm is the distance between the time–evolved state and the state with reduced virtual dimension. For the time–evolution of the Mott–distribution that was discussed in section 5.1.2, this quantity is plotted in fig. 5.7. We find that the distance is typically of order 10^{-3} for $D = 2$ and of order 10^{-4} for $D = 3$ and $D = 4$. Another quantity we monitor is the total number of particles $\langle \hat{N} \rangle$. Since this quantity is supposed to be conserved during the whole evolution,
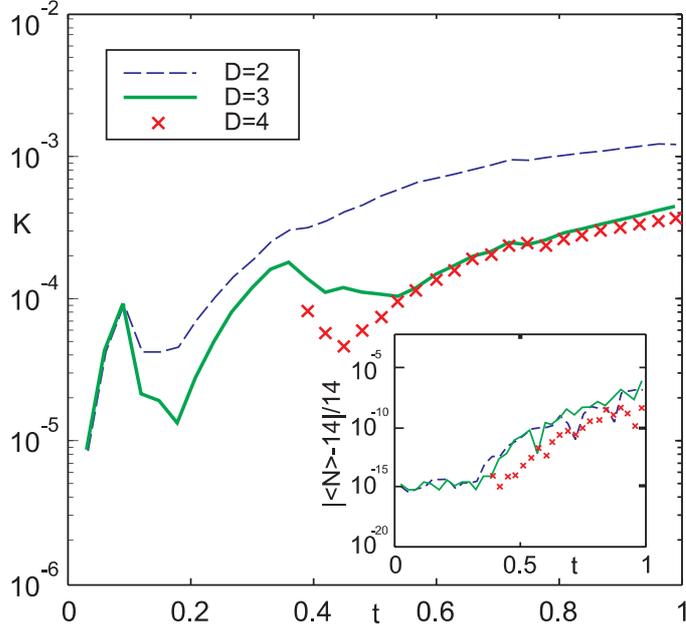
Figure 5.7: Distance K between the time–evolved state and the state with reduced virtual dimension. The virtual dimensions $D = 2$, $D = 3$ and $D = 4$ are included. The distance is plotted for the evolution of a Mott-distribution with $N = 14$, as explained in fig. 5.6. From the inset, the deviation of the particle number from the value 14 can be gathered.

its fluctiations indicate the reliability of the algorithm. From the inset in fig. 5.7, the fluctuations of the particle number in case of the time–evolution of the Mott–distribution can be gathered. We find that these fluctuations are at most of order 10^{-5}.

The main bottleneck for the performance of the algorithm is the scaling of the number of required multiplications with the virtual dimension D. As mentioned in section 4.4, the number of required multiplications is of order D^{10}. Another bottleneck for the algorithm forms the scaling of the required memory with the virtual dimension D – which is of order D^8. The simulation on a 11×11–lattice with $D = 5$ thereby required a main memory of 2 GB. These bottlenecks make it difficult at the moment to go beyond a virtual dimension of $D = 5$. Nonetheless, a virtual dimension of $D = 5$ is expected to yield good results for many problems already.

5.2 Frustrated Antiferromagnets in two Dimensions

Frustrated spin–systems have attracted a lot of interest in the last years, because they may possess exotic ground states that are very different from conventional Néel–ordered states. Such states are especially intriguing, as connections to high-T_c superconductivity have been put forward [4]. They are usually characterized by a break down of long–range order: the system reorganizes in a quantum state where only local antiferromagnetic correlations are present. The class of such states, named Short Range Valence Bond States (SRVB), encompasses a broad range of phases: they range from valence bond crystals with broken translational symmetry to pure spin liquids that have all symmetries restored.

Studies of frustrated systems are especially challenging, because Quantum Monte–Carlo (QMC) studies are hindered by the sign-problem [150] and Density Matrix Renormalization Group (DMRG) [169, 168, 135] investigations are restricted to one–dimensional systems. Other methods that have been developed to take on these systems are, for example, the coupled cluster method [127], DMRG combined with QMC [33] and exact diagonalizations within the subspace of SRVB [88, 89]. In this section, we give the PEPS–algorithm [154, 101] presented in chapter 4 a try.

In the following, we focus on the $J_1 - J_2 - J_3$ model, especially on the $J_1 - J_3$ and the $J_1 - J_2$ model (section 5.2.1 and section 5.2.2). We discuss our observations and possible implications. In the $J_1 - J_2 - J_3$ model on a square lattice, frustration is caused by the competition between first, second and third neighbor interactions of magnitudes J_1, J_2 and J_3 respectively:

$$H = J_1 \sum_{\langle ij \rangle} \mathbf{s}_i \cdot \mathbf{s}_j + J_2 \sum_{\langle\langle ij \rangle\rangle} \mathbf{s}_i \cdot \mathbf{s}_j + J_3 \sum_{\langle\langle\langle ij \rangle\rangle\rangle} \mathbf{s}_i \cdot \mathbf{s}_j$$

The phase diagram of this model is involved and still controversal. Of special interest are the regimes of maximal frustration that are suspected of having non-classical ground states.

Let us first review the classical limit [39, 24, 97, 48] ($S \to \infty$). In this limit, the system possesses four phases, as shown in figure 5.8: the usual Néel phase, two spiral antiferromagnetic phases ordered at (q, q) and (q, π) and a phase with collinear order. The Néel phase is bounded by the *classical critical line* $(J_2 + 2J_3)/J_1 = 1/2$.

When quantum fluctuations are taken into account, the phase diagram changes considerably [39, 41, 124, 88]: the Néel phase substantially extends to larger values of J_3, up to the line of maximal frustration $(J_2 + J_3)/J_1 = 1/2$
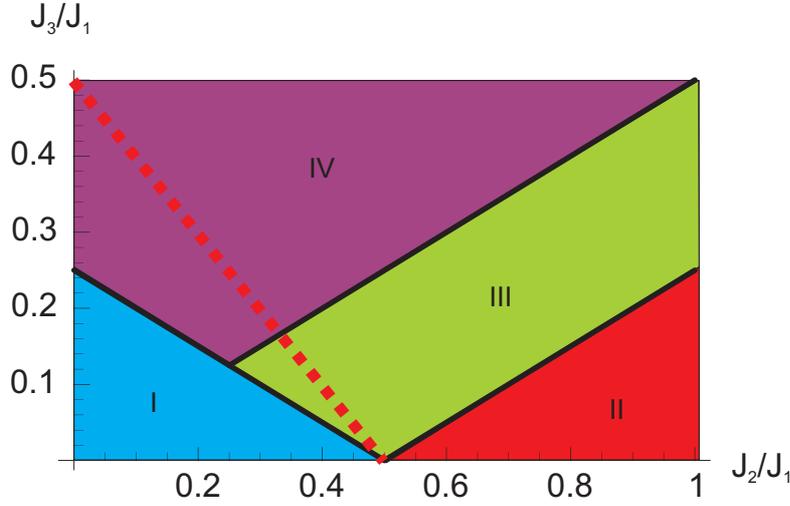
Figure 5.8: Classical phase diagram of the $J_1 - J_2 - J_3$ model. Phase I is the usual Néel phase, phase II a collinear phase and phases III and IV are two spiral antiferromagnetic phases ordered at (q, q) and (q, π). The red dotted line denotes the line of maximal frustration in the quantum case.

(see red dotted line in figure 5.8). In the vicinity of this line, it is believed that the classical ordered ground state is destabilized and a singlet ground state is formed [88]. The precise nature of this state is still controversal: suggestions include columnar valence bond crystals [81], plaquette states [88] and spin liquids [17, 175, 16, 21, 87]. Special attention has been devoted to the end-points of the line: the point at $J_3/J_1 = 1/2$ that separates the Néel from the spiral antiferromagnetic phase [17, 16, 87], and the tri-critial point at $J_2/J_1 = 1/2$ at which 3 phases meet [175, 33, 21, 20].

In the following, we focus on two lines in the phase diagram that include these points: $J_2 = 0$ ($J_1 - J_3$ model) and $J_3 = 0$ ($J_1 - J_2$ model). In both cases, we apply the PEPS-algorithm and discuss our observations.

5.2.1 $J_1 - J_3$ Model

In order to get a first idea of the nature of the ground state as J_3/J_1 increases, we calculate the static structure factor,

$$S(\mathbf{q}) = \frac{1}{N^2} \sum_{kl} e^{i\mathbf{q} \cdot (\mathbf{r}_k - \mathbf{r}_l)} \langle \mathbf{s}_k \cdot \mathbf{s}_l \rangle. \tag{5.1}$$

Figure 5.9 shows $S(\mathbf{q})$ for the 10×10 lattice at values of J_3/J_1 of 0.1, 0.5, 0.7 and 0.9. For $J_3/J_1 < 0.5$, it is clearly observed that $S(\mathbf{q})$ is peaked
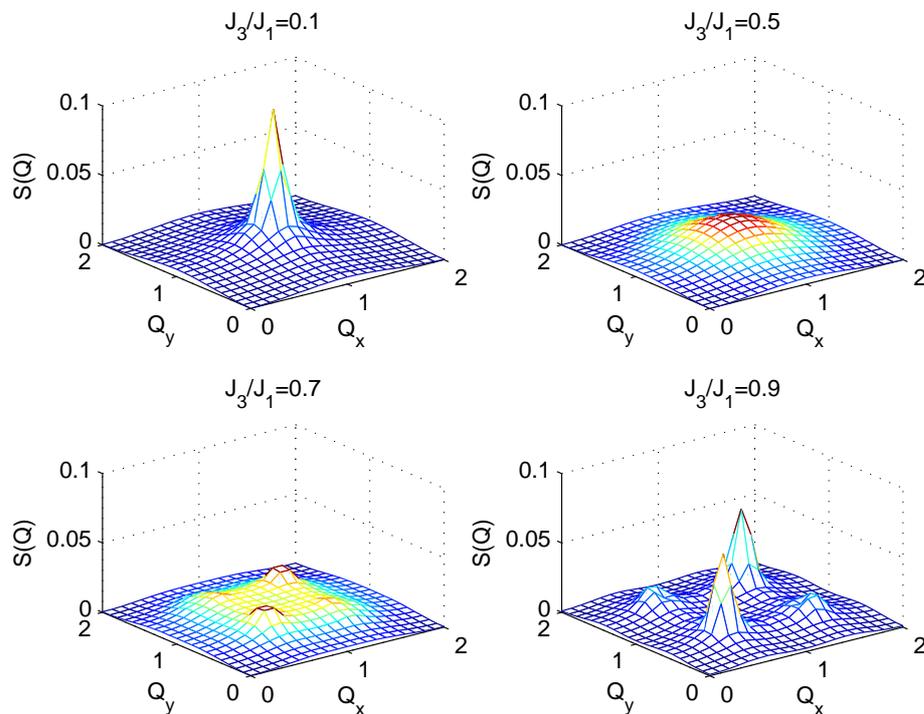
Figure 5.9: Structure factor $S(\mathbf{q})$ for different values of J_3/J_1. The values of Q_x and Q_y are in units of π. The results were obtained for a 10×10–lattice and virtual dimension $D = 3$.

at $\mathbf{q} = (\pi, \pi)$, indicating long–range Néel order. This order disappears at $J_3/J_1 \sim 0.5$ at which the structure factor becomes smooth. At around $J_3/J_1 \sim 0.7$ peaks at $(\pm\pi/2, \pm\pi/2)$ reappear, indicating a revival of incommensurate long–range order.

The collapse of long–range order is confirmed by a direct observation of the spin–spin correlations $\langle \mathbf{s}_i \cdot \mathbf{s}_j \rangle$. These are shown in figure 5.10 for $J_3/J_1 = 0.1$, 0.3, 0.5 and 0.8. The system–size considered is 20×20. As can be seen, the spins are antiferromagnetically ordered for $J_3/J_1 < 0.5$. For $J_3/J_1 > 0.5$, every second spin possesses antiferromagnetic order. However, the long–range order of the spins disappears in the vicinity of $J_3/J_1 \sim 0.5$.

The considerable decrease of the correlation length at $J_3/J_1 \sim 0.5$ opens the possibility for a short–range resonating valence bond state (SRVB) in this area. We investigate this possibility by doing a direct comparison of the PEPS results to results obtained by an exact diagonalization of the Hamil-
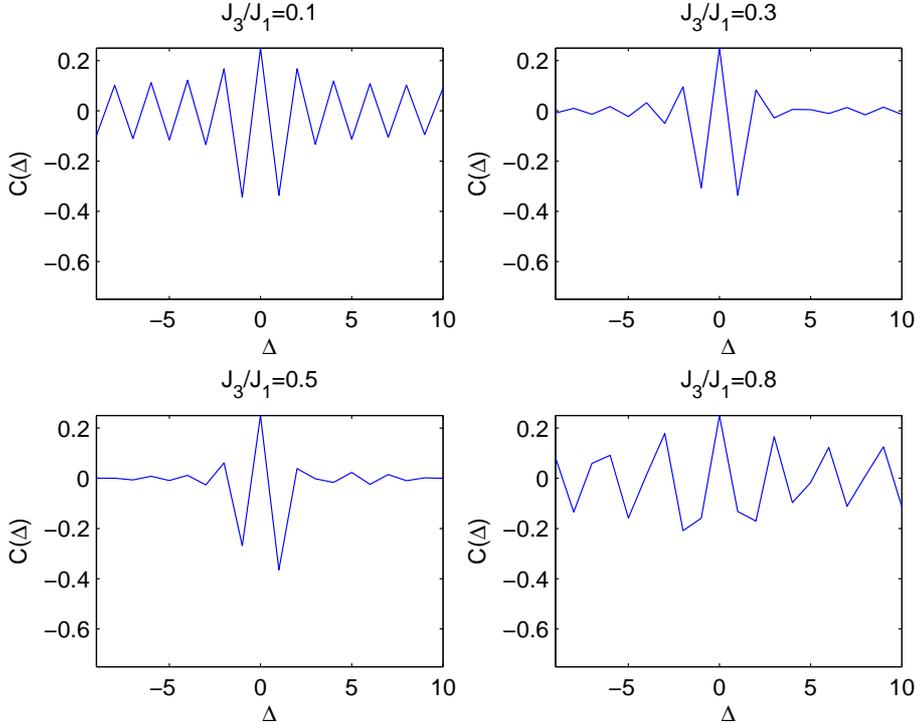
Figure 5.10: Spin–spin correlations $\langle \mathbf{s}_i \cdot \mathbf{s}_j \rangle$ as a function of the distance $\Delta = |i - j|$ for the 20×20 $J_1 - J_3$ model. The results have been obtained using a $D = 3$–PEPS.

tonian in the subspace of SRVB. The overlap between the SRVB and PEPS with virtual dimensions 3 and 4 on a 6×6–lattice can be gathered from figure 5.11a. As it can be seen, the overlap increases up to 99% at the point $J_3/J_1 = 0.5$ and is significantly smaller in other regions. A comparison of energies, however, reveals that the set of valence bond states does not cover all terms in the ground state. As shown in figure 5.11b, the energies of the diagonalization within the subspace of SRVB are - though very close to the PEPS–results at $J_3/J_1 = 0.5$ - always higher than the energies obtained within the set of PEPS. Thus, the true ground state at $J_3/J_1 = 0.5$ might contain a small fraction of valence bond terms that have longer range.

Even if it is assumed that the ground state is a pure SRVB in the vicinity of $J_3/J_1 = 0.5$, its properties can be very rich and it needs a more precise classification. On the one hand, it could be a state with broken translational symmetry - such as a columnar valence bond crystal or a plaquette state.
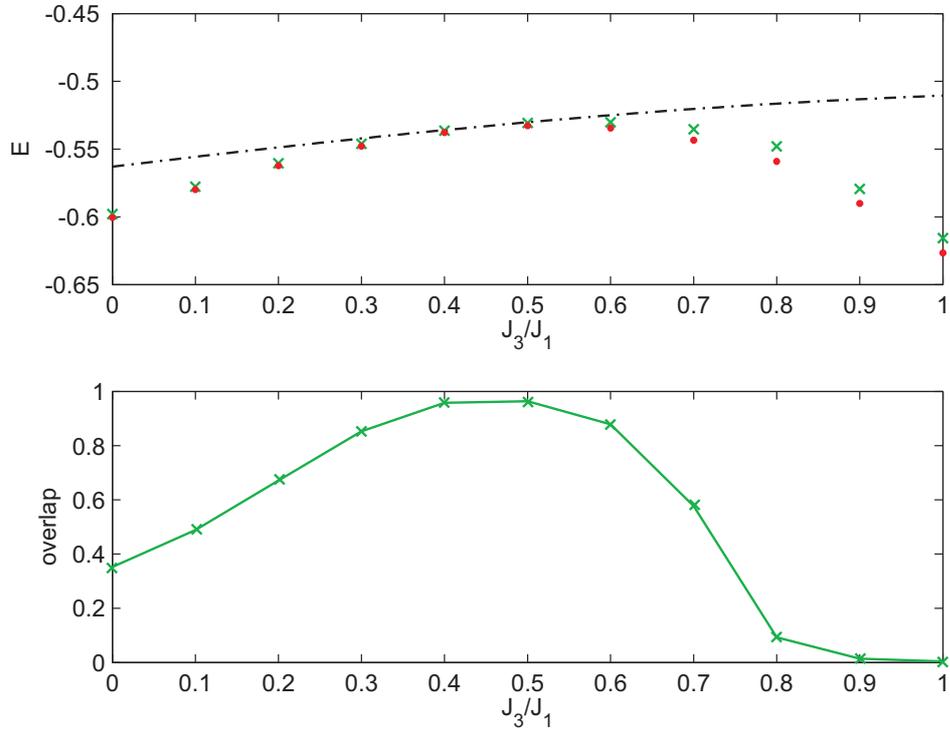
Figure 5.11: (a) Ground state energy of the $J_1 - J_3$ model on a 6×6 lattice as a function of J_3/J_1, obtained by diagonalizing within the SRVB subspace (solid line) and by PEPS calculations with $D = 3$ (crosses) and $D = 4$ (dots). (b) Overlap between the SRVB ground state and the $D = 3$–PEPS ground state.

On the other hand, an equally weighted superposition of valence bond states with restored translational symmetry known as spin–liquid is possible.

The observation of nearest–neighbor spin–spin correlations $\langle \mathbf{s}_i \cdot \mathbf{s}_j \rangle$ gives us an indication of a plaquette state [44]. These correlations are shown in figure 5.12 for a 8×8 lattice and $D = 3$. In case of a pure plaquette state, the nearest–neighbor spin–spin correlations would be equal to $-1/2$ on a plaquette and 0 between two plaquettes. In our case, the values of the spin–spin correlations deviate slightly from these values, nontheless a clear plaquette structure remains visible.

The plaquette order is better detected and more clearly distinguished from the Néel ordered phase by the cyclic permutation operator $P_{\alpha\beta\gamma\delta}$ of the four spins α, β, γ and δ on one plaquette. By means of this operator, the
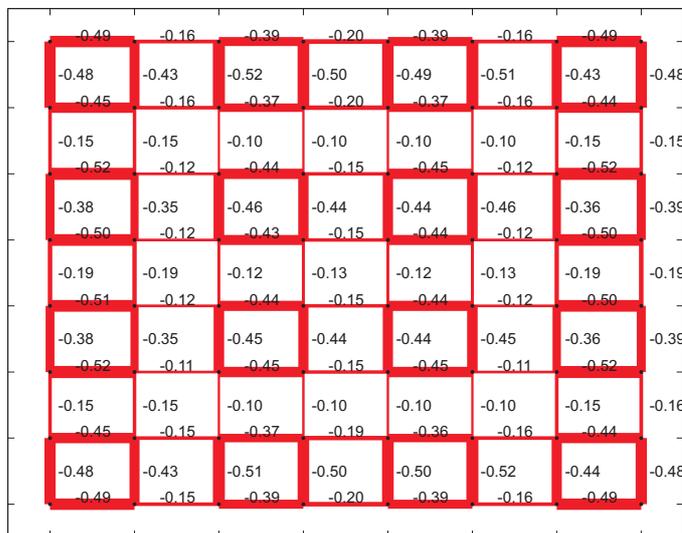
Figure 5.12: Nearest–neighbor spin–spin correlations at $J_3/J_1 = 0.5$, calculated with $D = 3$–PEPS.
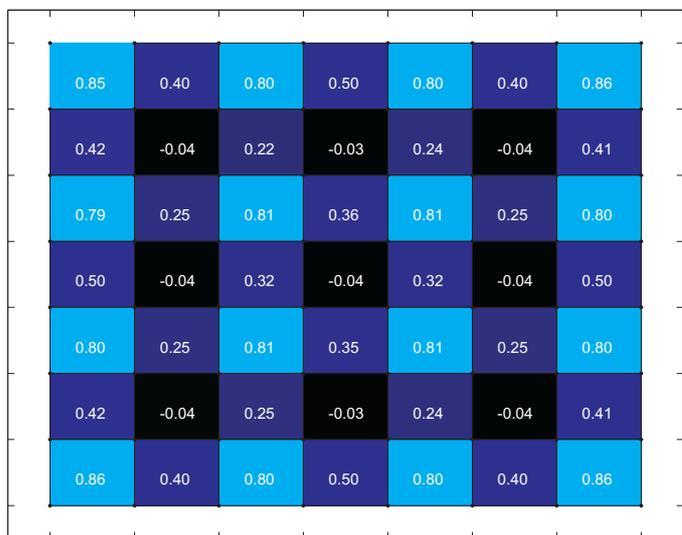
Figure 5.13: Plaquette order parameter $Q_{\alpha\beta\gamma\delta}$ at $J_3/J_1 = 0.5$, evaluated on a 8×8 lattice. The used virtual dimension is $D = 3$.

plaquette order parameter [44] is defined as

$$
\begin{aligned}
Q_{\alpha\beta\gamma\delta} &= \frac{1}{2}\left(P_{\alpha\beta\gamma\delta} + P_{\alpha\beta\gamma\delta}^{-1}\right) \\
&= 2\left(\mathbf{s}_\alpha \cdot \mathbf{s}_\beta \mathbf{s}_\gamma \cdot \mathbf{s}_\delta + \mathbf{s}_\alpha \cdot \mathbf{s}_\delta \mathbf{s}_\beta \cdot \mathbf{s}_\gamma - \mathbf{s}_\alpha \cdot \mathbf{s}_\gamma \mathbf{s}_\beta \cdot \mathbf{s}_\delta\right) \\
&\quad + 1/2\left(\mathbf{s}_\alpha \cdot \mathbf{s}_\beta + \mathbf{s}_\gamma \cdot \mathbf{s}_\delta + \mathbf{s}_\alpha \cdot \mathbf{s}_\delta + \mathbf{s}_\beta \cdot \mathbf{s}_\gamma\right) \\
&\quad + 1/2\left(\mathbf{s}_\alpha \cdot \mathbf{s}_\gamma + \mathbf{s}_\beta \cdot \mathbf{s}_\delta + 1/4\right).
\end{aligned}
$$

In case of a pure plaquette state, this order parameter assumes the value 1 on each plaquette; between the plaquettes, its expectation value is $1/8$. The order parameter vanishes in case of the Néel state which lacks the cyclic permutation symmetry. In figure 5.13, we plot the plaquette order parameter evaluated on all square clusters. As before, a clear plaquette structure is visible, though the absolute values of the expectation values differ slightly from the optimal ones.

To get a better impression of the vicinity of the ground state to a pure plaquette state, we average the expectation values of the plaquette order parameters evaluated on all plaquettes. The dependence of this quantity on the ratio J_3/J_1 can be gathered from figure 5.14. Lattice sizes of 4×4, 6×6, 8×8, 10×10, 14×14 and 20×20 are considered and indicated by the different lines in the figure. As can be clearly seen, the averaged plaquette order parameter shows a peak in the vicinity of $J_3/J_1 = 0.5$. It is further noticed that the absolute value of the order parameter decreases with increasing particle number N. An extrapolation to $N \to \infty$, however, suggests that the value remains finite. For the extrapolation, a scaling with $1/\sqrt{N}$ is assumed. The extrapolation is illustrated by the dashed line in the figure. The error bars indicate the reliability of the extrapolation.

In conclusion, the PEPS algorithm reproduces well the properties of the $J_1 - J_3$ model in the regimes of weak frustration and gives strong indications for a plaquette ordered state in the regime of strong frustration. In this regime, our results are thus consistent with ref. [88].

5.2.2 $J_1 - J_2$ Model

As in the previous section, we get a first impression of the order in the ground state of the $J_1 - J_2$ model by studying the static structure factor $S(\mathbf{q})$ given in (5.1). The structure factor is plotted in figure 5.15 for values of J_2/J_1 equal to 0.1, 0.5, 0.6 and 0.9. Similar to the $J_1 - J_3$ model, $S(\mathbf{q})$ indicates long–range Néel order for $J_2/J_1 \lesssim 0.5$ with a peak at (π, π). For J_2/J_1 larger than 0.5, columnar long–range order develops which is detected by a peak at $(0, \pi)$. In fact, this columnar long–range order reveals an order–by–disorder
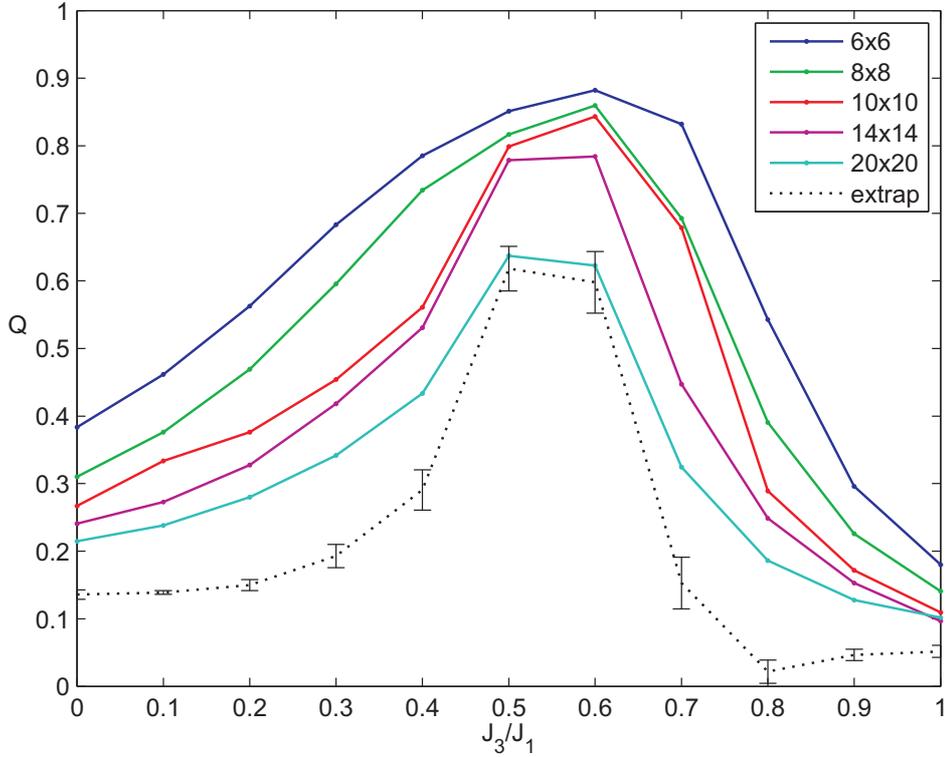
Figure 5.14: Averaged plaquette order parameter $Q_{\alpha\beta\gamma\delta}$ as a function of J_3/J_1 for different lattice–sizes. The used virtual dimension is $D = 3$. The dotted line indicates results of an extrapolation to $N \to \infty$ via finte–size scaling. The error bars indicate the reliability of the extrapolation.

phenomenon [164]: quantum fluctuations select from the huge manifold of classical ground states configurations where all spins are parallel to a given direction. In the regime in–between the Néel and the columnar phase the peaks disappear and long–range order breaks down.

The vicinity of the ground state to the class of SRVB in this region is analyzed in figure 5.16a. This figure shows the overlap of the PEPS ground state with the ground state obtained by exact diagonalization within the PEPS subspace. Lattice size 6×6 and virtual dimensions 3 and 4 were considered. The overlap clearly reaches the maximum at $J_2/J_1 = 0.5$ and assumes a value of about 70%. A comparison of the energies, as shown in figure 5.16b, uncovers that the true ground state will not be exactly in the subspace of SRVB: the energies of the PEPS calculations are slightly lower than the ones obtained from SRVB, even at the critical point. Nonetheless, the distance to the subspace of SRVB might be very small for $J_2/J_1 \approx 0.5$.
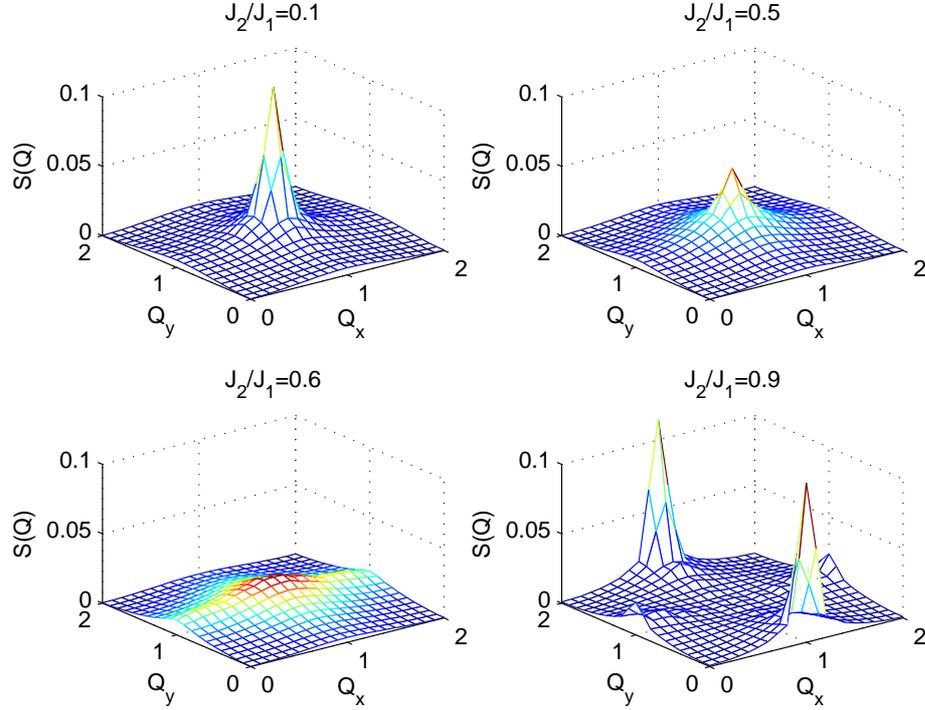
Figure 5.15: Structure factor $S(\mathbf{q})$ for different values of J_2/J_1. The values of Q_x and Q_y are printed in units of π. The results were obtained for a 10×10–lattice and $D = 3$.

A more precise classification of the ground state is done by observing the *order parameter for the columnar dimer state* [81]

$$\chi = \langle \left| \frac{1}{N} \sum_{\mathbf{r}} \theta_{\mathbf{r}} \right|^2 \rangle$$

with

$$\theta_{\mathbf{r}} = (-1)^{r_x} \mathbf{s_r} \cdot \mathbf{s_{r+\hat{x}}} + i(-1)^{r_y} \mathbf{s_r} \cdot \mathbf{s_{r+\hat{y}}}.$$

The vectors $\hat{\mathbf{x}}$ and $\hat{\mathbf{y}}$ denote unit vectors in horizontal and vertical direction respectively. The values of this order parameter as a function of J_2/J_1 for $D = 3$ and lattice sizes 6×6, 8×8 and 10×10 can be gathered from figure 5.17. As can be seen, there is a clear peak in the region of maximal frustration. The order parameter decreases with increasing N. The extrapolation to $N \to \infty$ shows that this peak remains finite. This gives a strong indication of a valence bond crystal with columnar order in the region of maximal frustration.
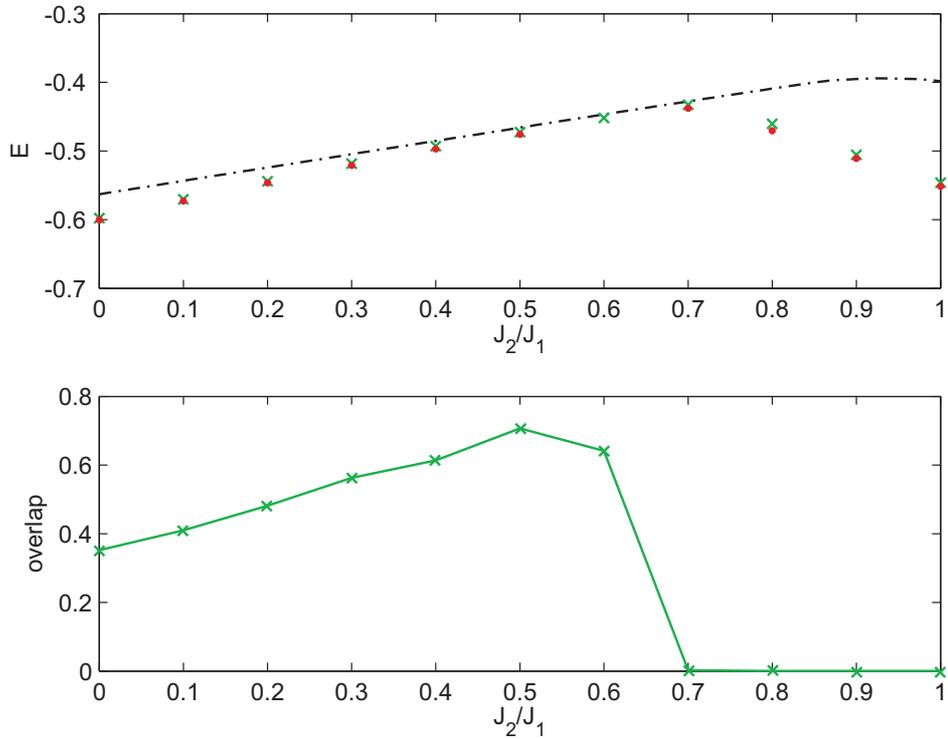
Figure 5.16: (a) Ground state energy of the $J_1 - J_2$ model on a 6×6 lattice as a function of J_2/J_1, obtained by diagonalizing within the SRVB subspace (solid line) and by PEPS calculations with $D = 3$ (crosses) and $D = 4$ (dots). (b) Overlap between the SRVB ground state and the $D = 3$–PEPS ground state.

Thus, the PEPS algorithm reproduces also well the properties of the $J_1 - J_2$ model. Furthermore, it gives strong indications for a columnar ordered valence bond state in the regime of strong frustration.
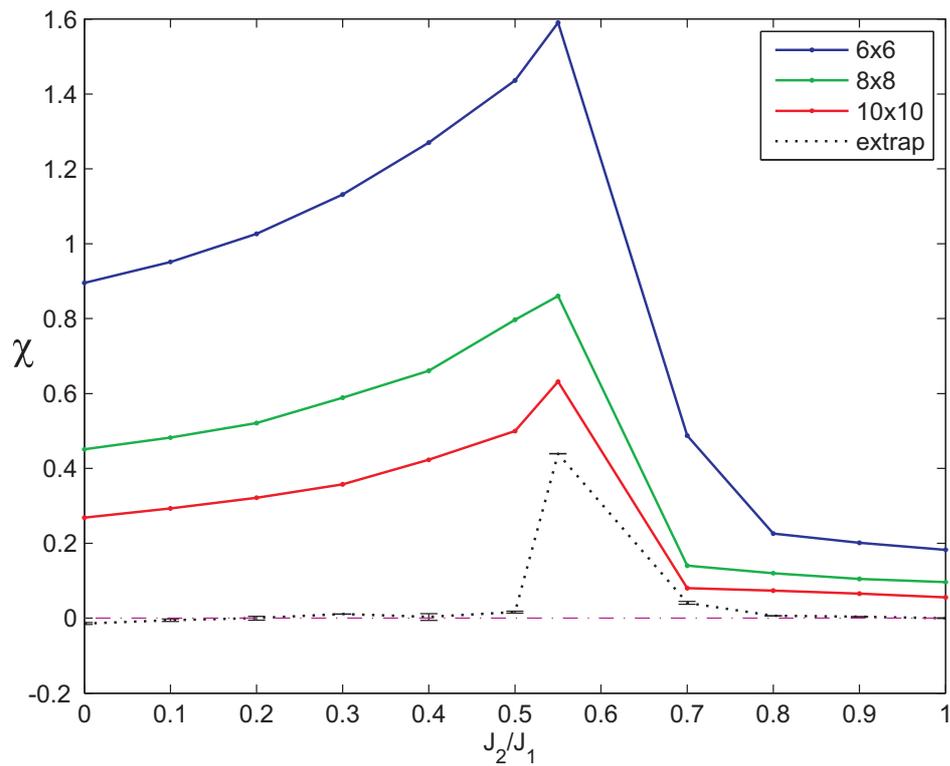
Figure 5.17: Order parameter for the columnar dimer state χ as a function of J_3/J_1 for different lattice–sizes. The used virtual dimension is $D = 3$. The dotted line indicates results of an extrapolation to $N \to \infty$ via finte–size scaling. The error bars indicate the reliability of the extrapolation.

Chapter 6

Conclusions

Summing up, we have described two algorithms that are natural extentions of variational algorithms with MPS.

In chapters 2 and 3, we have introduced an algorithm to efficiently calculate partition functions of 2–D classical and 1–D quantum systems. This algorithm we have applied to the 2–D Ising model and the 1–D Bose–Hubbard model with a harmonic trap. In case of the 2–D Ising model, we have compared our results to exact solutions of the model and found that the error can indeed be made very small. For the 1–D Bose–Hubbard model, we have found indications for a Mott–superfluid transition by observing the full width at half maximum of the (quasi)–momentum distribution at various interaction–strengths.

In chapters 4 and 5, we have described the class of *Projected Entangled Pair States* (PEPS) as a natural generalization of MPS to higher dimensions. As a first application, we have studied the system of hard–core bosons on a 2–D lattice using a variational method based these states. We have thereby investigated the ground state properties of the system and its responses to sudden changes in the parameters. We have compared our results to results based on the Gutzwiller ansatz. We have observed that the Gutzwiller ansatz predicts very well the density distribution of the particles. However, the momentum distribution obtained from the Gutzwiller ansatz is, though qualitatively similar, quantitatively clearly different from the distribution obtained from the PEPS ansatz. In addition, the PEPS and the Gutzwiller ansatz are very different in the prediction of time evolutions. We conclude that the Gutzwiller ansatz has to be applied carefully in these cases.

As a further application, we have investigated the ground states of frustrated spin–systems on 2–D lattices. We have thereby focused on the $J_1 - J_2 - J_3$ model and found that the ground state in the strongly frustrated parameter regime is constructed of nearest–neighbor dimers. These dimers form

a plaquette structure at the point $(J_2/J_1, J_3/J_1) = (0, 1/2)$ and a columnar structure at the point $(J_2/J_1, J_3/J_1) = (1/2, 0)$. We have shown via finite–size scaling plots that these structures persist in the thermodynamic limit.

These applications give a clear demonstration of the power of the PEPS-approach, both for finding ground states in higher-dimensional quantum spin systems and for simulating real-time evolution.

Part III

Quantum Simulations

Chapter 7

Introduction

As it was argued in the previous part, exact simulations of quantum systems on classical computers are not feasible, since the required resources scale exponentially with the number of particles, and the utilization of sophisticated approximative methods becomes necessary. On a quantum computer, however, such simulations can be performed efficiently - a conclusion already reached by Richard Feynman in 1982. The reason is that these devices harness the laws and phenomena of quantum mechanics. These laws and phenomena characterize the quantum world and they are fundamentally different from those one encounters in classical physics: Complex probability amplitudes, quantum interference, quantum parallelism, quantum entanglement and the unitarity of the quantum evolution are the most impressive of these phenomena. These phenomena comprise an enormous potential of computational power.

A quantum computer is a system built up of a set of quantum systems (qubits), such as $s = 1/2$ nuclear spins with possible orientations *up* and *down*. The basis states of one qubit are usually denoted as $|\,0\,\rangle$ and $|\,1\,\rangle$. These states represent the binary values 0 and 1. Thus, a qubit is the quantum analogue to a classical memory cell that stores the binary values 0 or 1. However, a qubit has properties that are more general than the properties of a classical memory cell: A qubit is allowed to be in a superimposed state, such as $\frac{1}{2}(|\,0\,\rangle + |\,1\,\rangle)$, and it can be entangled with numerous other qubits of the system. These properties constitute the basis for the power of a quantum computation. A quantum computation consists of the following three steps: First of all, the input data is encoded in a quantum state and the quantum computer is prepared in this state. In second place, the state of the quantum computer is manipulated by realizing a certain time–evolution. Finally, a measurement of interest is performed. The result of the measurement forms the output data of the computation. The way in which the time–evolution

is realized leads to a classification of quantum computers in "analog" and "digital" - in the same spirit as in case of classical computers.

The "digital" quantum computer realizes the time–evolution by means of few elementary operations acting on one or two qubits - usually referred to as quantum gates. With appropriate sequences of such quantum gates, arbitrary time–evolutions can be created. Sequences of quantum gates are usually denoted as *quantum networks* or *quantum algorithms*. The efficiency of the quantum algorithm is judged by the scaling of the number of required gates with the size of the input: If the number of gates scales *polynomially* with the size of the input, the quantum algorithm is considered to be efficient. At this point, the question arises whether efficient quantum algorithms exist that have no classical analogue. Indeed, this question can be answered affirmatively. For example, Shor's algorithm [140] allows to factorize integers in a time that scales *polynomially* with the number of digits, whereas every known classical algorithm requires an *exponenial* number of gates. In addition, Seth Lloys introduced the concept of a *Universal Quantum Simulator* [86] that is based on a quantum algorithm that is capable of efficiently simulating arbitrary quantum systems.

The *Universal Quantum Simulator* works as follows: assume, the quantum system under study consists of N particles. The state of each particle shall live in the Hilbert-space $\mathcal{H}^{(j)}$ of dimension d. The Hilbert-space that corresponds to the whole quantum system then decomposes as

$$\mathcal{H}_N = \mathcal{H}^{(1)} \otimes \cdots \otimes \mathcal{H}^{(N)}$$

and is of dimension d^N. The dynamics of the system shall be described by the Hamiltonian H. The time evolution operator that corresponds to this Hamiltonian reads

$$U(t) = e^{-iHt/\hbar}.$$

A time evolution according to H of duration T transforms the initial state of the system, $|\psi(0)\rangle$, into the final state $|\psi(T)\rangle = U(T)|\psi(0)\rangle$. The *Universal Quantum Simulator* is a quantum computer equipped with a quantum algorithm that simulates this time evolution and yields properties of the final state $|\psi(T)\rangle$. An efficient decomposition of this time–evolution into elementary gates is possible if the quantum system evolves according to local interactions, i.e. is described by a Hamiltonian that is equal to a sum of operators H_j that act on a smaller subspace of $\mathcal{H}_N$:

$$H = \sum_{j=1}^{L} H_j$$

It is assumed that the operator H_j acts on a subspace of dimension m_j and that this dimension is independent from N. The time evolution operator corresponding to the Hamiltonian H can now be approximated by a product of exponentials:

$$U(T) \approx \left(e^{-iH_1T/\hbar} \cdots e^{-iH_LT/\hbar} \right)^n \qquad (7.1)$$

The error that is made by this approximation is calculated as [86]

$$\left\| e^{-iHT/\hbar} - \left(e^{-iH_1T/\hbar} \cdots e^{-iH_LT/\hbar} \right)^n \right\|_\infty \leq \kappa \frac{T^2}{n},$$

with

$$\kappa = \frac{1}{2} \left\| \sum_{j<k} [H_j, H_k] \right\|_\infty.$$

In order to guarantee that the error is at most ϵ, the value of n has to exceed the bound $\kappa\frac{T^2}{\epsilon}$. The number of gates that are required to realize the approximation (7.1) of the unitary transformation $U(T)$ on the quantum computer is estimated as follows: The realization of the operator $e^{-iH_jT/\hbar}$ requires a number of gates of order m_j^2. The number of gates for the realization of $U(T)$ with an accuracy $1 - \epsilon$ therefore amounts to

$$n \sum_{j=1}^{L} m_j^2 \leq nLm^2 \approx \kappa\frac{T^2}{\epsilon} Lm^2,$$

with

$$m = \max_j \{m_j\}.$$

Since κ, T, m and ϵ are independent from N, the efficiency of the algorithm is determined by the scaling of the function L with the number of particles N: A *polynomial* scaling of L with N makes the algorithm efficient. Such a *polynomial* scaling is shown by all many-particle systems with local interactions. Famous examples are the Ising model, the Heisenberg model and the Hubbard model.

A system that may hold the promise of a "digital" quantum simulator is a system of laser–cooled trapped ions [25, 26, 78]. In this system, ions are stored and laser–cooled in an electromagnetic trap in such a way that they remain practically frozen in a specific region of space. The internal states of an ion are used as a storage for a single qubit. Due to the relatively large separation of the ions (about $10\mu m$), the ions can be individually addressed with lasers. Thus, the internal states of individual ions can be precisely manipulated and measured with very high efficiency. Furthermore, they can be decoupled from the environment very efficiently. All this makes possible the

implementation of one- and two–qubit gates [25] - the main building blocks of universal quantum simulators. The two–quibit gates are thereby based on the strong interaction between the ions via Coulomb repulsion. By a first laser–pulse directed on one ion, the internal state of this ion is transferred to the collective center–of–mass motion of all ions. A second laser–pulse directed on another ion triggers the absorbtion of the state–dependent center–of–mass motion by the ion. This way, a state–dependent interaction between 2 ions is realized. Realizations of such systems have been achieved in numerous experiments [96, 73, 79, 132].

Another system of interest for "digital" quantum simulations is a system of cold atoms in optical lattices [66, 65]. Here, neutral atoms are loaded from a Bose-Einstein condensate into an optical lattice via a quantum phase transition. Each qubit is stored in the internal states of an atom. The result is an array of a huge number of identifiable qubits. These qubits cannot be addressed individually, but it is possible to apply massively parallel operations. This is done by using two spin–dependent optical lattices: one that traps the qubit state $|0\rangle$ and one that traps the qubit state $|1\rangle$. By shifting one optical lattice by a single lattice-site, state–dependent controlled collisions between adjacent atoms are induced. These state–dependent collisions realize two–qubit gates that are the same for all adjacent qubits. This makes this scheme very useful for the simulation of translational invariant systems [141]. In the laboratory, such scenarios have been realized in series of remarkable experiments [54, 90].

Unlike the "digital" quantum computer, the "analog" quantum computer realizes the desired time–evolution directly by using a system that evolves according to the same physical equations, but can be controlled and measured more easily than the original system. This is very close to the idea of a classical "analog" computer: for example, electrical phenomena are used to model mechanical components, such as springs and dashpots, because they are described in terms of equations that are essentially of the same form. Also, physical simulations in wind tunnels may be considered as "analog" computers. In the same spirit, one can simulate the dynamics of a complicated quantum system by choosing a system that is described by the same Hamiltonian but can be very well controlled and measured.

Many mathematical problems and ground–states of physical systems can be investigated very well with an "analog" quantum computer by means of adiabatic variations of the available parameters. This way of obtaining solutions is referred to as "adiabatic quantum computation" [38, 23, 37, 151]. The prerequisite for such a method to work is that the solution can be encoded in the ground state of a Hamiltonian. This Hamiltonian is usually referred to as *problem Hamiltonian H_P*. Mathematical problems with this

property are for example NP–complete combinatorial search problems like 3SAT and Exact Cover. The solution of those problems therefore reduces to transforming the initial state of the quantum computer into the ground state of the *problem Hamiltonian H_P*. This is realized by making use of the Adiabatic Theorem [9, 69, 46]: this theorem states that a system stays in the instantaneous ground state if it evolves according to a Hamiltonian that varies sufficiently slowly in time. Thus, the obvious thing to do is to construct an "analog" system with a Hamiltonian that interpolates between a *beginning Hamiltonian H_B* whose ground state is easily prepared and the *problem Hamiltonian H_P* as a parameter is varied. The algorithm then consists in preparing the quantum computer in the ground state of the *beginning Hamiltonian* and varying the parameter such that the Hamiltonian of the system changes from the *beginning Hamiltonian* into the *problem Hamiltonian*. If the parameter is varied sufficiently slowly, the Adiabatic Theorem guarantees that the final state of the quantum computer will be close to the ground state of the *problem Hamiltonian*. The measurement of the final state then yields with a high probability of success the solution to the problem. The duration of the algorithm is related to this probability of success, because only a time evolution that lasts for a sufficiently long time guarantees a slowly varying Hamiltonian. In order to ensure a high probability of success, the duration of the algorithm has to exceed a certain bound. The estimation of this bound is fundamental for the discussion of adiabatic quantum computation, because this bound states whether adiabatic quantum computations can surpass computations performed on classical computers. The Adiabatic Theorem basically states that this bound is proportional to $\frac{1}{\Delta^2}$, where Δ denotes the minimum gap between the ground state energy and the energy of the first excited state. As a consequence, level crossings between the ground state and the first excited state that result in $\Delta = 0$ make the algorithm fail. The investigation of the efficiency of adiabatic quantum computation therefore consists in rigorously studying the spectrum of the interpolating Hamiltonian [99].

A system that can be considered as an "analog" quantum simulator for the Bose–Hubbard model [42] is the system of cold atoms in optical lattices [66, 65]. The Bose–Hubbard model describes the physics of interacting bosons on a lattice. It is closely related to the Hubbard model which originates from solid state physics and describes the motion of electrons between the atoms of a crystalline solid. It can also be used for the effective description of other interesting physical systems like arrays of Josephson junctions [11]. The phase diagram of this model is especially interesting because of the competitions between two tendencies of the particles: the tendency towards global coherence, due to the hopping of the particles, and the ten-

dency towards localization induced by the strong interactions. From these competitions two phases emanate: the superfluid phase with completely delocalized particles and the Mott–phase where every particle has a fixed position. Realizations of transitions between these two phases by means of bosons in optical lattices have been proposed theoretically [66] and observed experimentally [54].

Other approaches for an "analog" quantum simulator are based on trapped ions interacting with lasers. These approaches are capable of realizing effective-spin models with Ising or the Heisenberg–like interactions [173, 122, 30] and interacting–boson models [121, 31]. In case of the effective-spin models, the spins are represented by the internal states of the ions. All ions are driven by off-resonant laser beams propagating along the three spatial directions. The effect of these lasers is to exert a state–dependent force on the ions that excites collective motions. These motions induce effective Ising or Heisenberg–like interactions between the internal levels of the ions. In case of the interacting–boson models, the bosons are associated with the vibrations (phonons) of the ions. The anharmonicities in the trapping potentials give rise to the effective phonon–phonon interaction.

In the following, we give two further examples of "analog" quantum simulators. In Chapter 8, a way to realize a Tonks-Girardeau gas by means of atoms in an optical lattice is proposed. In chapter 9, extensions of the idea to realize effective spin–models and interacting–boson models by means of trapped ions interacting with lasers are discussed. It is shown that a wide range of spatial dimensions and particle interactions may be achieved by placing the ions in a regular structure induced by an optical lattice or arrays of ion microtraps.

Chapter 8

Tonks–Girardeau Gas in a 1–D Optical Lattice

Strongly correlated quantum systems are among the most intriguing and fundamental systems in physics. Here the Tonks-Girardeau gas [51, 85], proposed about 40 years ago, is especially remarkable. In such a gas, bosonic particles are confined to one dimension, and repulsive interactions between them dominate the physics of the system. In order to minimize their mutual repulsion, the bosons are prevented to be at the same position in space. This mimics the Pauli exclusion principle for fermions, resulting in pronounced fermionic properties of the bosonic particles [51, 85]. Interestingly however, these fermionized bosons do not exhibit either completely ideal bosonic or fermionic quantum behaviour, which is for example reflected in their characteristic momentum distribution [80]. Here we report on the preparation of a Tonks–Girardeau gas of ultracold rubidium atoms held in a two–dimensional optical lattice formed by two orthogonal standing waves. The addition of a third, shallower lattice potential along the long axis of the quantum gases has allowed us to enter the Tonks–Girardeau regime by increasing the effective mass and thereby enhancing the role of interactions. We make a theoretical prediction of the momentum distribution based on an approach in which trapped bosons acquire fermionic properties and find that it agrees closely with the measured distribution.

8.1 Tonks–Girardeau Gas

The physics of ultracold 1–D Bose systems is drastically different from that of ordinary 3–D cold gases [51, 85, 119, 34]. For example, by decreasing the particle density n, a usual 3–D quantum many body system becomes

more ideal, whereas in a 1–D Bose gas the role of interactions becomes more important. The reason is that at temperatures $T \rightarrow 0$ the kinetic energy of a particle at the mean interparticle separation is $K \propto n^2$ and it decreases with decreasing density n faster than the interaction energy per particle $I \propto n$. The ratio of the interaction to kinetic energy $\gamma = I/K$ characterizes the different physical regimes of the 1–D quantum gas. For a large value of γ, the gas enters the Tonks-Girardeau (TG) regime, where the repulsion between particles strongly decreases the wave function at short interparticle distances.

Achieving such a TG regime and observing "fermionization" of the 1–D Bose system is a great challenge, and it is complementary to the current experiments in which bosonic properties are observed in fermionic quantum gases [67, 1, 176, 125]. The 1–D regime is obtained by tightly confining the particle motion in two directions to zero point oscillations [119, 34, 109]. It was first demonstrated in experiments with weakly interacting Bose-condensed trapped gases, where $\gamma \ll 1$(see ref. [52, 136]). In ref. [53] a tight radial confinement was realized by using two-dimensional optical lattice potentials to create an array of one-dimensional quantum gases. In later experiments with optical lattices [98, 149] it has become possible to reach a one-dimensional regime with $\gamma \approx 1$, i.e. in-between a weakly interacting 1–D Bose condensed gas and a fermionized Tonks-Girardeau gas. So far, however, it has not been possible to bridge the last one or two orders of magnitude in γ that could bring the bosonic quantum gas fully into the TG regime. Larger values of γ could either be reached by decreasing the density of the quantum gas or by increasing the effective interaction strength between the particles [119, 34].

In this work, we propose and demonstrate a novel idea of achieving the TG regime. The main point is to include an additional optical lattice along the 1–D gas, which results in an increase of γ. For a homogeneous gas, γ can be expressed as $\gamma = mg/\hbar^2 n$, where g is the one-dimensional interaction strength, m the mass of a single atom and $\hbar$ denotes Planck's constant divided by 2π. The addition of a periodic potential along the third axis increases the effective mass and thus leads to an increase of γ. In fact, in the limit in which only the first Bloch band is occupied we have $I = U\nu$ and $K = J\nu$, where ν is the filling factor, U the on-site interaction energy and J the tunnelling amplitude, and thus $\gamma = U/J$. Additionally, in order to achieve a pure TG regime in a lattice, the filling factor ν should be smaller than unity. Otherwise doubly occupied sites would be present and the direct correspondence to the TG gas would be lost. Following these ideas we have been able to enter the TG regime with $\gamma \approx 5 - 200$. In this regime, the bosons can be theoretically described using a fermionization approach [35, 77]. For $\gamma \rightarrow \infty$, the ground

state of N bosons at zero temperature is described by the many body wave function

$$\Psi_0(x_1, x_2, \ldots, x_N) \propto |\det[\varphi_i(x_j)]|, \qquad i, j = 1, \ldots, N \qquad (8.1)$$

where det denotes the Slater determinant, and $\varphi_i(x)$ is the ith eigenfunction of the single-particle Hamiltonian. The presence of the Slater determinant guarantees that the wave function vanishes whenever two particles occupy the same position in space. However, the absolute value of the determinant ensures that the wave function for the bosons remains completely symmetric. This wave function reflects the fundamental similarities between strongly interacting bosons and non-interacting fermions in 1–D, with properties such as the spatial density distribution, the density-density correlation function, or the entropy of the gas being the same as in the case of non-interacting fermions. More interestingly though, several properties are strongly modified by the presence of the absolute value of the determinant, leading to a unique behaviour of e.g. the momentum distribution of the TG gas [80]. This can be understood qualitatively in the following way: the bosonic particles in a TG gas are not allowed to occupy the same position in space. Due to this restriction, they are distributed over a more extended region in momentum space than in the case of an ideal or weakly interacting Bose gas. On the other hand, in order to keep themselves apart from each other, they do not need to be in different momentum states, as it would be the case for fermions.

8.2 Experimental Realization

Let us first describe the experimental realization together with the measured data and then provide a detailed theoretical analysis of the system. In order to reach the regime of low filling factor we start with a rather small Bose-Einstein condensate (BEC) of approximately 4×10^4 ^{87}Rb atoms in a magnetic trap. Then the BEC is loaded into a two-dimensional optical lattice potential (along the y- and z-axes) such that an array of one-dimensional quantum gases is created (see Fig. 8.1a). The lattice potential is formed by superimposing two orthogonal standing waves with a wavelength of $823nm$ on top of the BEC. In order to transfer the atoms into the optical potential, the potential depth of the optical lattice is first gradually increased to a mean final value of $27E_R$ (see Fig. 8.1b). Here E_R is the recoil energy $\hbar^2 k^2 / 2m$, with k describing the wave vector of the lattice laser light. During this ramp up of the lattice potentials, the tunnel coupling between the different one-dimensional quantum gases decreases exponentially. This results in a decoupling of the quantum gases, such that particle exchange between
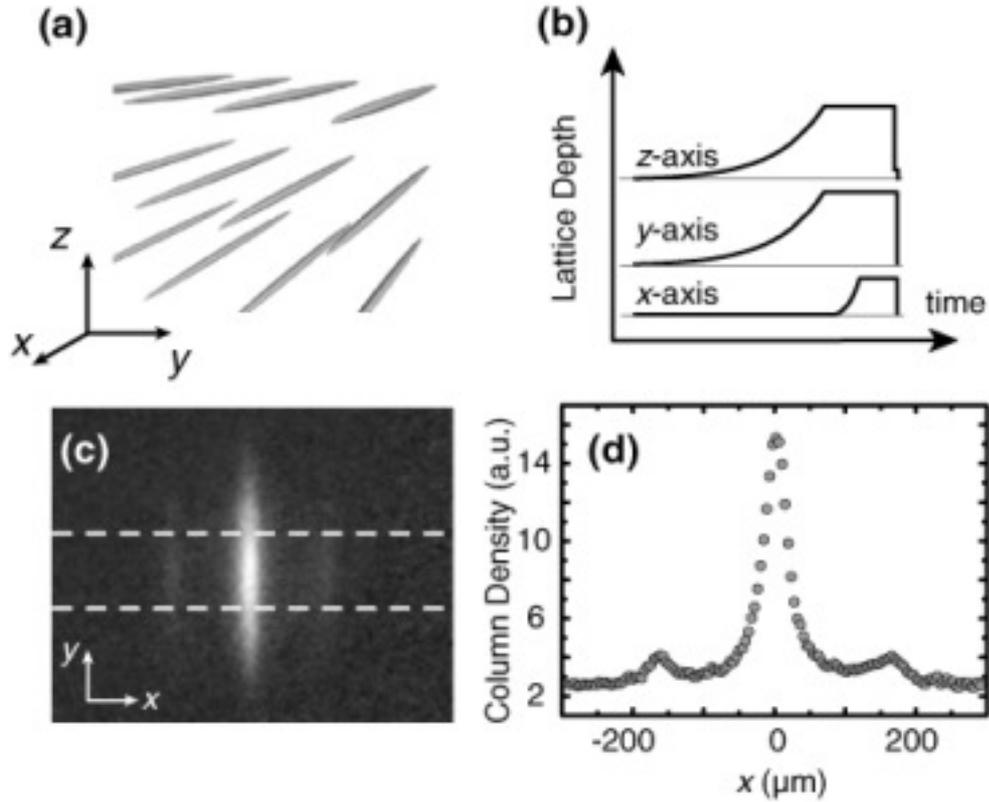
Figure 8.1: (a) Experimental sequence and momentum profiles. (b) Using a 2–D optical lattice potential, we realize an array of 1–D quantum gases. (c) These quantum gases are created by first increasing the optical lattice depths along the y and z axes in an exponential ramp over a time of $160ms$ (time constant $t = 40ms$) to a mean final value of $27E_R$. After a further hold time of $10ms$ at this final lattice depth, we increase the optical lattice potential along the x axis within a time of $20ms$ (time constant $t = 10ms$) to a variable lattice depth V_{ax}. The quantum gases are then allowed to equilibrate for another $30ms$ before we probe the momentum distribution as described in the text. (d) Typical time-of-flight images after a ballistic expansion of the atom clouds over a time of $16ms$ for an axial optical lattice depth $V_{ax} = 6.5E_r$. The white dashed lines denote the area from which averaged momentum profiles along the x axis are extracted.

different tubes is suppressed. For the maximum lattice depth, the Gaussian shape of the laser beams ($150\mu m$ waist) leads to an axial harmonic confinement of the 1–D gases with a trapping frequency of $\omega_{ax} \approx 2\pi \times 60Hz$. This has been verified by exciting a sloshing motion of the thermal cloud and by parametric heating measurements, which both agree with the calculated value. Furthermore, the depths of all standing wave potentials have been measured by vibrational band spectroscopy [113]. For such onedimensional quantum gases, without a lattice in the axial direction, we have $\gamma \approx 0.5$ near the lattice centre.

After a further hold time of $10ms$, we add an optical standing wave along the axial direction (x-axis) in order to increase γ. The intensity of the laser forming this lattice potential (operated at a wavelength of $854nm$) is ramped up to a final depth V_{ax} of up to $18.5E_R$. The axial momentum distribution of the quantum gases is subsequently probed by suddenly removing all optical and magnetic trapping potentials and by imaging the atom clouds after a time-of-flight period of $16ms$. In order to prevent a strong expansion of the atom cloud along the propagation axis of the imaging laser beam (z-axis), which would make the experiment more sensitive to misalignments in the imaging axis, we reduce the confinement along this axis by lowering the z-lattice potential to $6E_R$ within a time of 100 s before initiating the ballistic expansion sequence. Also, along the x-axis we use a ramp down, which is not fully non-adiabatic and leads to a narrowing of the Gaussian envelope in the observed momentum distribution by approx. 20%. This enhances the number of atoms in the central momentum peak. From the absorption images we extract profiles of the axial momentum distribution by averaging horizontal profiles through the centre of the atom cloud (see Fig. 8.1c).

In figures 8.2 and 8.3 we show six experimentally measured momentum profiles (see figures 8.5, 8.6 and 8.7 for all experimentally measured profiles) corresponding to different values of the axial optical lattice depth ($V_{ax}/E_R = 0 - 18.5$). In Fig. 8.2(a) there is no lattice present along the x-axis, and thus no first order diffraction peak appears. Here, the value of $\gamma \approx 0.5$ at the trap centre. For the rest of the figures we can use the relation $\gamma \sim U/J$ obtaining $\gamma \sim 5 - 200$, which indicates that one enters the TG regime rather rapidly when increasing the axial lattice depth. In the figures we also plot our theoretical predictions based on fermionization at finite temperature averaged over the different one dimensional tubes (see methods). Apart from a normalizing factor for each experimental curve, only the atom number in the central tube is used as an overall adjustable parameter in this model. This atom number is however kept constant between different momentum profiles. The initial temperature for the lowest axial lattice depth $V_{ax} = 4.6E_R$ has been obtained through a finite temperature fit
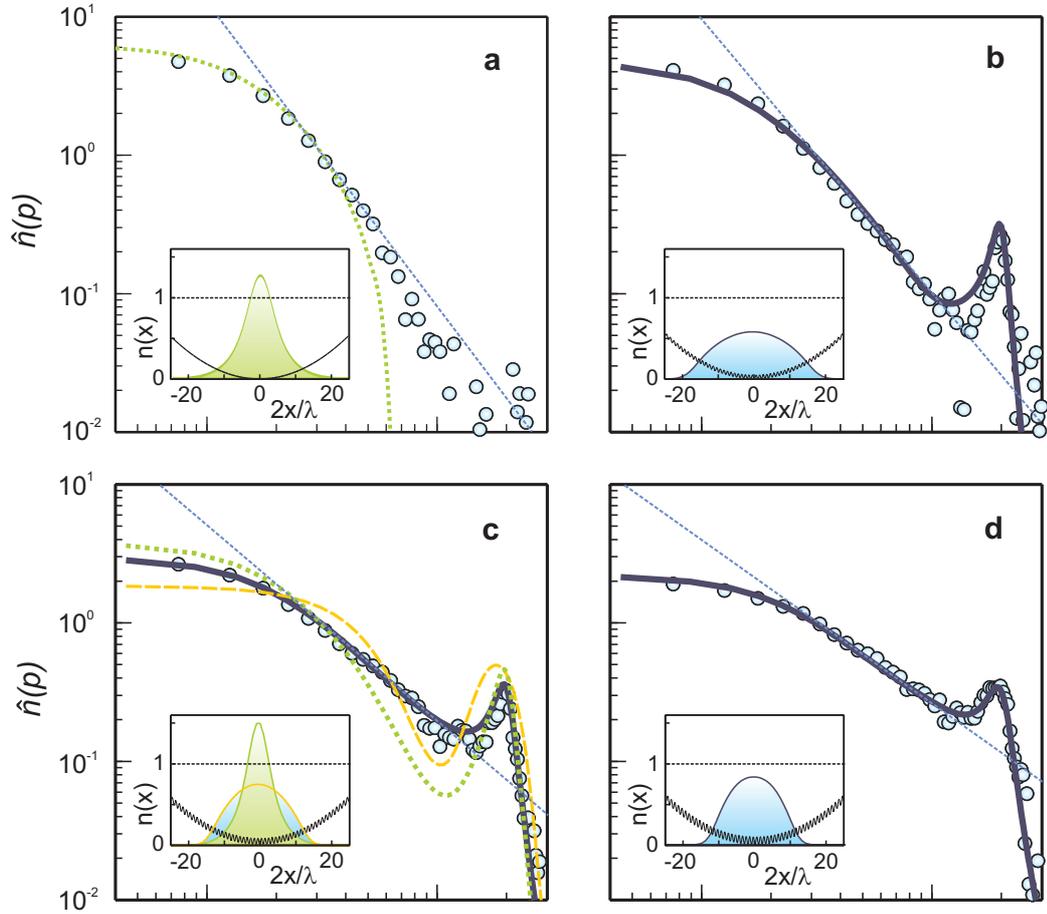
Figure 8.2: Momentum profiles of the 1–D quantum gases for different axial lattice depths. In (b)-(f), the experimental data (blue circles) are displayed together with our theoretical predictions (black line) based on fermionization at finite temperatures, averaged over the different 1D tubes. In order to emphasize the linear part of the momentum profiles, an auxiliary straight line with the corresponding slope is shown in each plot. In (c), the momentum profiles for the ideal Bose gas (green dotted lines) and the ideal Fermi gas (yellow dashed lines) are also displayed for comparison. For all plots, an atomic distribution characterized by an atom number $N_{0,0} = 18$ in the central tube is used, for which we have found the best agreement with the experimental data (see Methods). In the insets of (b)-(f), the density profile of a single 1–D tube with $N = 15$ particles at the corresponding temperature and lattice depth is shown for the fermionized gas (black lines in plots (b)-(f)), for the ideal Fermi gas (yellow line in (c)), and for the ideal Bose gas (green line in (c)).
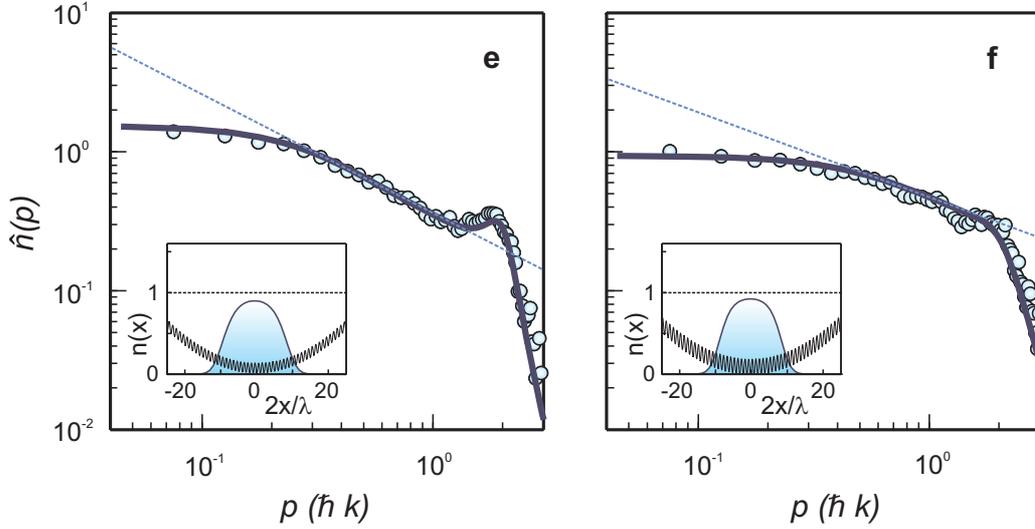
Figure 8.3: (Continuation of Fig. 8.2) The values of the axial lattice depths V_{ax}, the average temperatures, the slopes a of the linear part of the momentum profiles, and the values of $\gamma = U/J$ are: (b) $4.6E_R$ and $k_BT/J = 0.5$ (Tonks), $\alpha = 1.90$, $\gamma = 5.5$; (c) $7.4E_R$ and $k_BT/J = 0.7$ (Tonks), $k_BT/J = 1.6$ (ideal Bose gas), $k_BT/J = 0.7$ (ideal Fermi gas), $\alpha = 1.4$, $\gamma = 13.7$; (d) $9.3E_R$ and $k_BT/J = 0.9$ (Tonks), $\alpha = 1.2$, $\gamma = 23.6$; For the momentum profile without the axial lattice (a), we find $\alpha = 2.2$ and $\gamma = 0.5$ at the center of the trap. (e) $12E_R$ and $k_BT/J = 1.3$ (Tonks), $\alpha = 0.8$, $\gamma = 47.6$; (f) $18.5E_R$ and $k_BT/J = 3.9$ (Tonks), $\alpha = 0.6$, $\gamma = 204.5$.

to the corresponding momentum profiles using our fermionization approach. From this initial temperature the temperatures of the quantum gases at increasing lattice depth V_{ax} have been modelled by assuming conservation of entropy during the ramp up of the axial lattice. For all twelve experimentally measured momentum profiles we find an excellent agreement with the theory based on fermionization. For reference, we have plotted the results obtained assuming an ideal Bose or Fermi gas, also averaged over all the one dimensional tubes and at finite temperatures (see e.g. Fig. 8.2c).

8.3 Momentum Distribution

Let us discuss the momentum distribution in more detail. For a homogeneous gas at zero temperature and in the thermodynamic limit, the low momentum distribution in the Tonks gas regime exhibits a power law decay
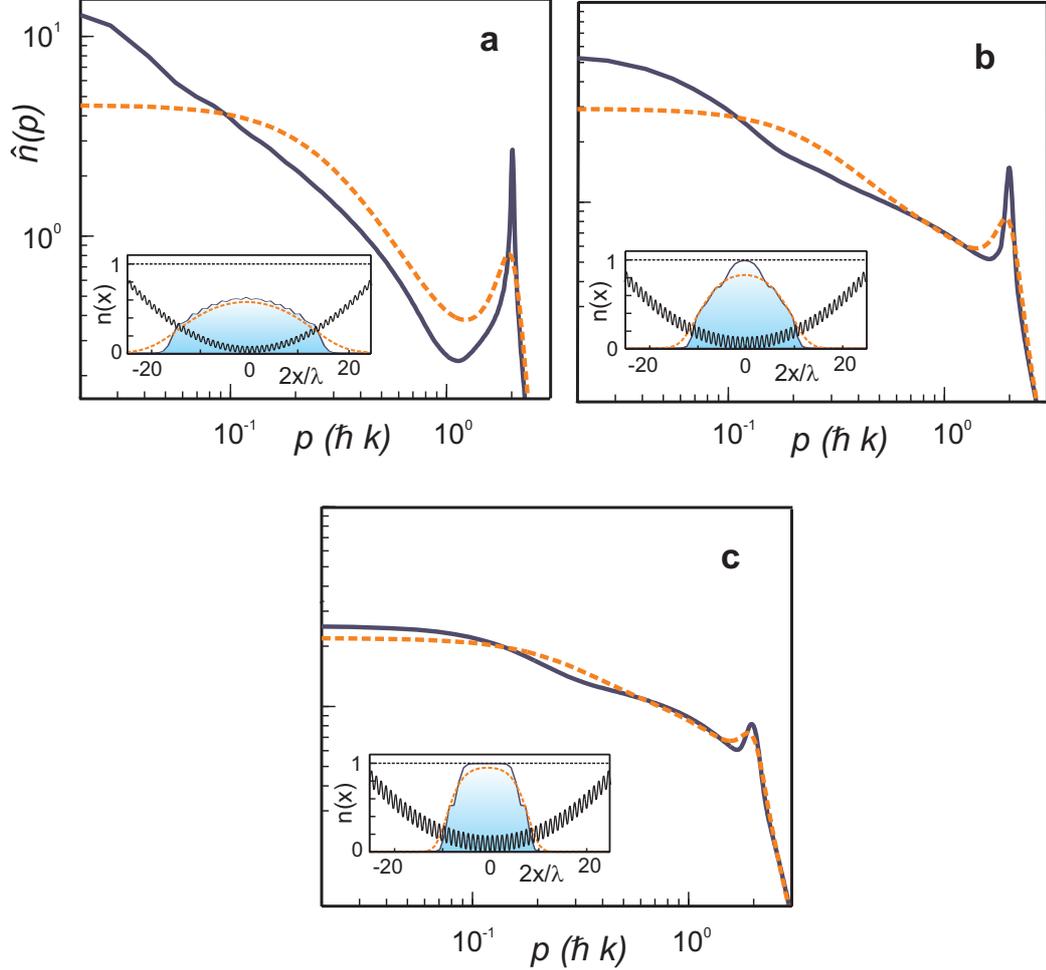
Figure 8.4: Momentum profiles of a single 1D tube obtained from our fermionization-based theory for different lattice depths. The plots are shown for axial lattice depths V_{ax} of $5.0E_R$ (a), $9.5E_R$ (b), and $12.0E_R$ (c). For all plots, the number of particles is $N = 15$, and $b = 8 \times 10^{-4}E_R$ (this value of b corresponds to the trapping frequency of the experiment; see Methods). In each plot, the log-log momentum profile at $k_BT/J = 0$ (black line) is displayed together with that at $k_BT/J = 1.0$ (orange dashed line). The density profiles at $k_BT/J = 0$ and $k_BT/J = 1.0$, together with the corresponding lattice-harmonic potential, are shown in the inset of each plot. Note that at $k_BT/J = 0$, finite size effects make the slope at low momenta deviate from the ideal $1/2$. The slope α is larger than $1/2$ for small filling factors ($\alpha = 0.79$ in (a)), it approaches $1/2$ as a Mott phase is developed at the centre of the trap ($\alpha = 0.49$ in (b)), and it decreases to zero deep in the Mott phase ($a = 0.29$ in (c)).

as $1/\sqrt{p}$ (ref. [80]). Therefore, a log-log plot for the momentum distribution of such a system should show a linear behaviour with slope 1/2. However, here we are considering a system with a finite number of particles (about 20 per tube) in a lattice, in the presence of a harmonic trap, and at finite temperatures. Our fermionization-based theoretical treatment of such a finite inhomogeneous Tonks gas predicts pronounced deviations of the momentum distribution from the "ideal" 1/2 behaviour (see Fig. 8.4), in agreement with the experimental data. Let us qualitatively explain this non-ideal behaviour of the momentum distribution. For an infinite lattice system, the only characteristic momentum is $p_\nu = \hbar \times 2\pi\nu/\lambda$ related to the mean interparticle separation, where λ is the wavelength of the axial lattice laser light and the filling factor ν is here smaller than 1/2. For $\nu \geq 1/2$ the lattice system can be viewed as a system of holes undergoing tunneling, and the filling factor ν in p_ν is replaced by $1 - \nu$, ensuring the particle-hole symmetry of the homogeneous lattice system. For momenta $p \ll p_\nu$ the momentum distribution exhibits a linear 1/2 behaviour, and for larger p it is strongly affected by short range correlations [110], which tend to increase the 1/2 slope. Note that for the case of $\nu = 1/2$, p_ν is the closest to the lattice momentum $\hbar \times 2\pi/\lambda$, and the momentum distribution is the least affected by short range correlations. The trapping potential and finite temperature introduce two new momentum scales, below which the slope has a tendency to decrease [77, 18]. Those are the momentum $p_L = \hbar \times \pi/L$ related to the finite size L of the system, and $p_T = \hbar \times \pi/L_T$, where $L_T \approx \lambda J \sin \pi\nu/k_B T$ is a characteristic length determined by the temperature. In our experiment we have $p_L < p_T \sim p_\nu$. Therefore, finite size and temperature effects overlap with effects of short range correlations, leaving no space for the ideal 1/2 behaviour. This explains the characteristic features of the log-log momentum profiles observed in the experiment:

1. A rather flat momentum distribution at small p, which extends to larger momenta with increasing lattice depth, since the ratio of temperature to tunneling slightly increases.

2. A linear region with slope larger than 1/2 at larger p.

Remarkably, the value of the slope decreases with the lattice depth, and the ideal 1/2 value is recovered on approach to the Mott insulator transition [42, 66, 54, 145, 76]. This is a fundamental feature that is present irrespective of the number of particles and trap frequency. It is related to the fact that in the trapped case the characteristic average filling factor of the system increases with the lattice depth, since tunneling decreases and particles try to accumulate near the trap centre. At the Mott insulator crossover, where

the filling factor at the trap centre is equal to unity, the average filling factor is close to $\nu = 1/2$ (see methods). This is the value for which the effects of short range correlations are strongly suppressed in a uniform lattice system. Note, finally, that in the weakly interacting regime for a trapped quasicondensate one should have a Lorentzian momentum distribution [126], which would correspond to a slope close of 2 for $p \gg \hbar \times \pi/L_T$. Already for low axial lattice depths V_{ax} we observe a smaller slope, which emphasizes a strong difference of our system from previously studied one-dimensional quasicondensates.

8.4   Methods

In the following, we develop the theoretical treatment based on fermionization that we have used above to model the experiment. We consider N bosonic atoms moving in the lowest band of a 1–D lattice and experiencing an additional harmonic potential. This situation is described by the Bose-Hubbard Hamiltonian $H = H_B + V$, where

$$
\begin{aligned}
H_B &= -J \sum_{l=-\infty}^{\infty} \left(a_l^\dagger a_{l+1} + a_{l+1}^\dagger a_l \right) + b \sum_{l=-\infty}^{\infty} l^2 a_l^\dagger a_l \\
V &= U \sum_{l=-\infty}^{\infty} a_l^{\dagger 2} a_l^2
\end{aligned}
$$

The first term describes the motion of the atoms in the combined lattice-harmonic potential, and the second one accounts for on-site interactions. The bosonic operators a_l annihilate one boson at the lth site, and fulfil canonical commutation relations $[a_l, a_{l'}^\dagger] = \delta_{ll'}$. The parameter b is related to the frequency ω of the harmonic potential by $b = 1/8m\omega^2\lambda^2$.

8.4.1   Fermionization

We will be interested in the strongly interacting or Tonks regime, in which two atoms cannot occupy the same lattice site. Within this regime, the bosonic operators a_l can be re-expressed using the Jordan-Wigner transformation [130] (JWT) in terms of fermionic ones c_l fulfilling $[a_l, a_{l'}^\dagger]_+ = \delta_{ll'}$. Under the JWT the interacting Bose Hamiltonian H_B is transformed into a non-interacting fermionic Hamiltonian H_F, through the replacement $a_l \to c_l$. In order to predict the behaviour of the different bosonic observables, one has to transform them into fermionic ones via the JWT, and then evaluate the corresponding expectation values for the fermionic ground state. At $T = 0$ the fermionic ground state is given by the Slater determinant of

eqn. (8.1). At a finite temperature T the wave function is a mixture of different Slater determinants characterized by the many-body density matrix $\rho \propto exp(-H_F/k_BT)$, where k_B is Boltzmann's constant.

8.4.2   Density and momentum distribution

The particle density $n(x)$ coincides with that of non-interacting fermions, since the JWT maps the corresponding bosonic observable onto the same fermionic one (e.g. $a_l^\dagger a_l \to c_l^\dagger c_l$). Under the Thomas-Fermi approximation we have

$$n(x) = \frac{1}{\pi} \arccos \left(\max \left[\frac{\mu - bx^2}{-2J}, -1 \right] \right),$$

if $\mu - bx^2 > -2J$ and zero otherwise. The size L of the cloud is $L = \lambda\sqrt{(2J + \mu)/4b}$, and μ is determined by imposing that the total number of particles is N. When $\mu \geq 2J$ a Mott phase is produced at the center of the trap, and $n(x = 0)$ is equal to 1. At this point the average filling factor of the system $\bar{\nu} = \lambda N/2L \approx 3/\sqrt{2\pi}$, a value which is close to $1/2$.

The momentum distribution $\hat{n}(p)$ is related to the one-particle correlation function $\langle a_l^\dagger a_{l'} \rangle$ through

$$\hat{n}(p) = |\phi(p)|^2 \sum_{l,l'=-\infty}^{\infty} e^{ip(l-l')} \langle a_l^\dagger a_{l'} \rangle,$$

where $\phi(p)$ is the Fourier transform of the Wannier function, and p denotes momentum in units of $\hbar k$. Using the JWT the bosonic one-particle correlation function can be re-expressed as

$$\langle a_l^\dagger a_{l'} \rangle = \langle c_l^\dagger (-1)^{\sum_{l>m>l'} c_m^\dagger c_m} c_{l'} \rangle,$$

where $l > l'$. Making extensive use of Wick's theorem, one can re-express this quantity as a Töplitz determinant $\langle a_l^\dagger a_{l'} \rangle = \det [G_{l,l'}]$, where $G_{l,l'}$ is a $(l - l') \times (l - l')$ matrix with elements

$$(G_{l,l'})_{x,y} = \langle c_{l'+y-1}^\dagger c_{l'+x} \rangle - \delta_{x,y-1}/2.$$

Therefore, in order to evaluate the momentum distribution at a finite temperature T one has to determine the one-particle correlation functions for a non-interacting Fermi system at that temperature. We have used the Grand Canonical Fermi-Dirac distribution and the exact eigenstates $\varphi_i(x)$ of the single-particle Hamiltonian to determine the momentum distribution in this way.

8.4.3   Averaging

In order to give a quantitative prediction for the experimental situation, we have averaged the momentum distribution for different tubes. To determine the atomic distribution, we have assumed that during the ramp up of the two-dimensional optical lattice potential tunnelling becomes negligible, and we have an array of independent 1–D gases. For each tube we have assumed a Thomas-Fermi density profile. Minimizing the total energy of the array with respect to the number of atoms in each of the tubes, we obtain

$$N_{i,j} = N_{0,0} \left(1 - \frac{5N}{2\pi N_{0,0}} (i^2 + j^2) \right)^{3/2},$$

where $N_{i,j}$ is the number of atoms in a tube located at position (i, j) in the two-dimensional optical lattice, N is the total number of particles in the array, and $N_{0,0}$ is the number of particles in the central tube. It follows that the probability of having a tube with M particles is

$$P(M) = \frac{2}{3} \frac{1}{N_{0,0}^{2/3} M^{1/3}},$$

where $M \leq N_{0,0}$. Remarkably, this distribution only depends on one parameter, namely, the number of particles in the central tube, which is the only adjustable parameter in our model.

     The temperature of each 1–D quantum gas has been calculated assuming adiabatic evolution of the system during the ramp up of the axial lattice. Due to the presence of the harmonic confinement, the ratio $k_B T/J$ is not conserved in the adiabatic evolution. Given the temperature at $V_{ax} = 4.6 E_R$, the conservation of entropy allows us to determine the temperature at the final lattice depth V_{ax}. The entropy of the TG gas coincides with that of the non-interacting Fermi gas, since both have the same spectrum and density of states. This results in the same temperatures for a TG gas and an ideal Fermi gas, but a different temperature for the ideal Bose gas when the axial lattice depth is increased. Note that tubes with different number of particles also have different temperatures at the same lattice depth.
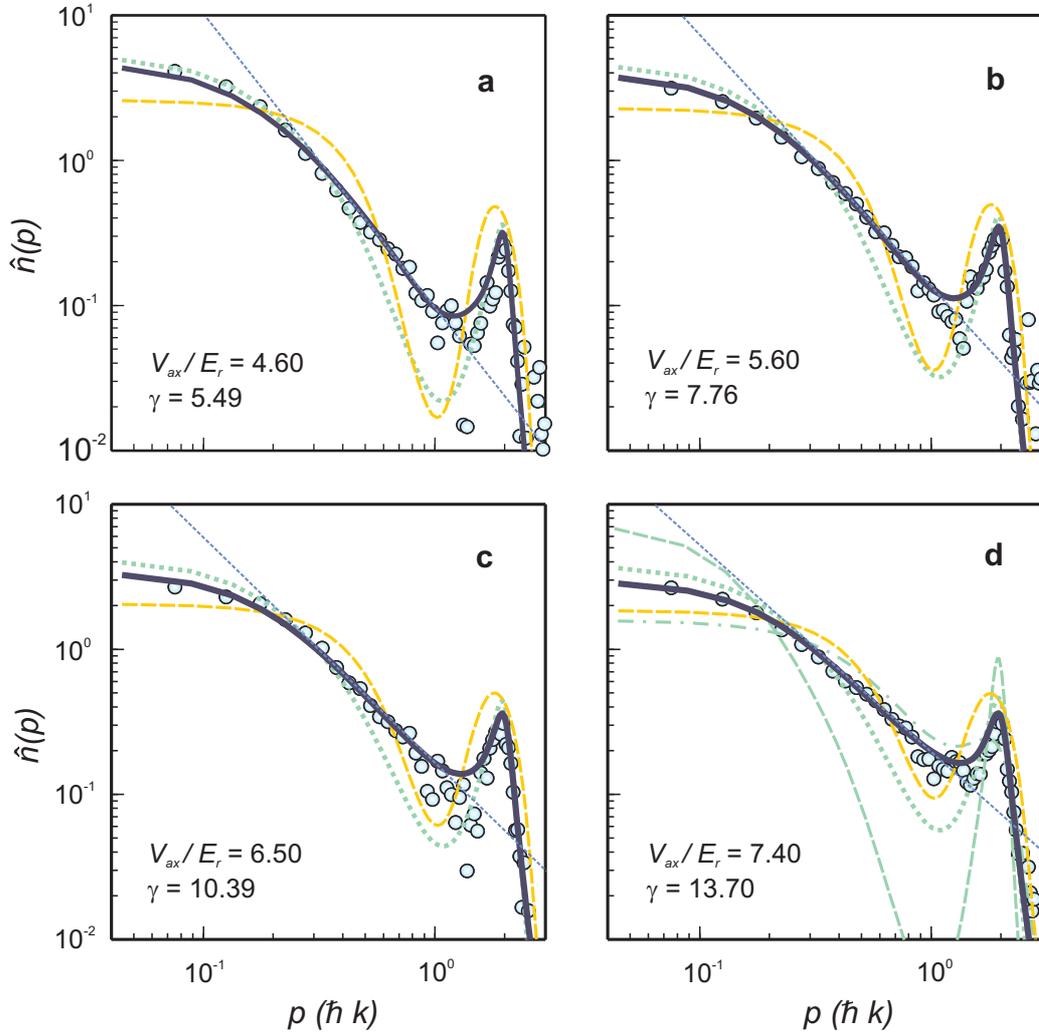
Figure 8.5: Momentum profiles of the one-dimensional quantum gases for different axial lattice depths (a)–(l). The experimental data (blue dots) are displayed together with our theoretical predictions for a fermionized gas (black line), an ideal Bose gas (green dotted line) and an ideal Fermi gas (yellow dashed line). In order to emphasize the linear part of the momentum profiles an auxiliary straight line with the corresponding slope is shown in each plot. For all plots an atomic distribution characterized by an atom number $N_{0,0} = 18$ in the central tube is assumed (see methods).
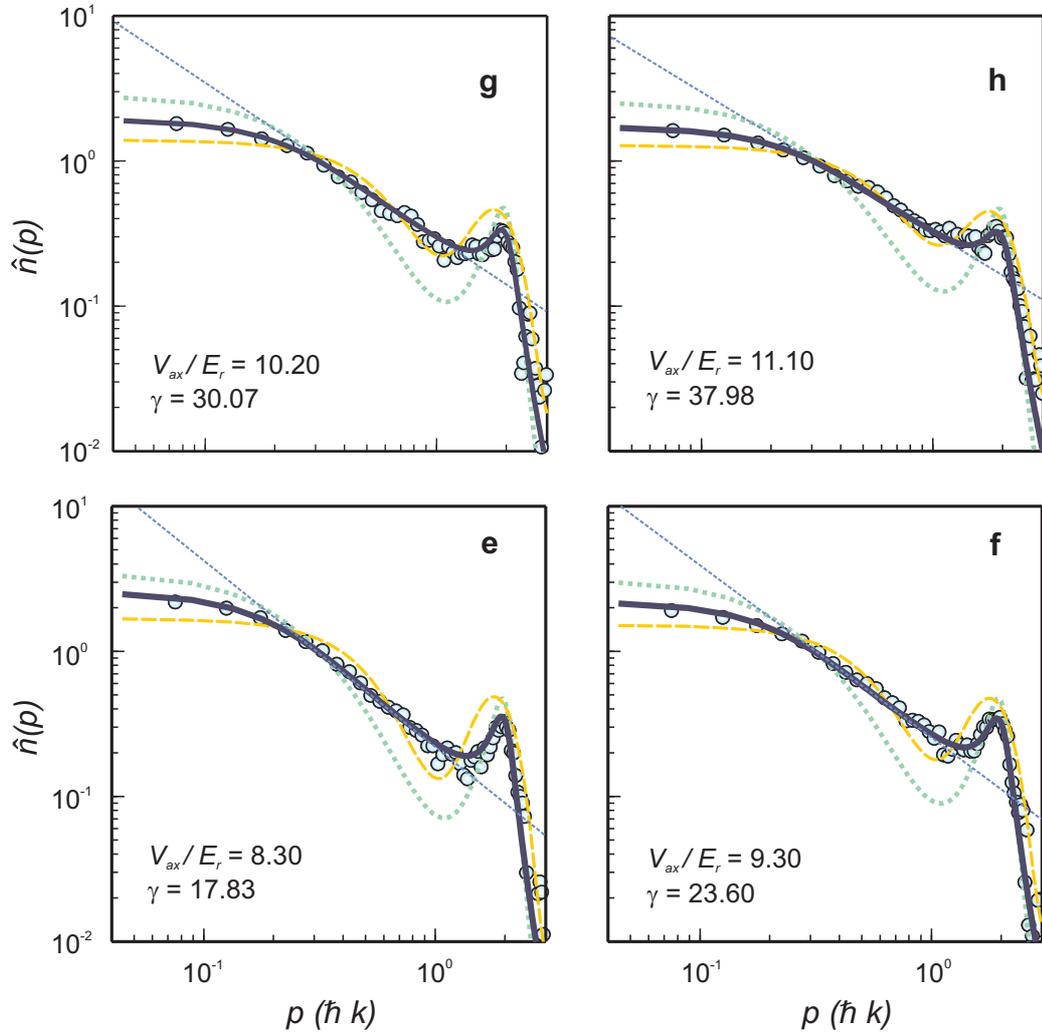
Figure 8.6: (continuation of figure 8.5) The temperatures for the Tonks and ideal Fermi gas have been obtained in the same way as for Fig. 8.2. The temperatures for the ideal Bose gas have been derived again assuming conservation of entropy for increasing axial lattice depths. In this case, the initial temperature at $V_{ax} = 0$ has been obtained using an ideal Bose gas fit to low momenta for this momentum profile, where the ideal Bose gas is a good description of the system.
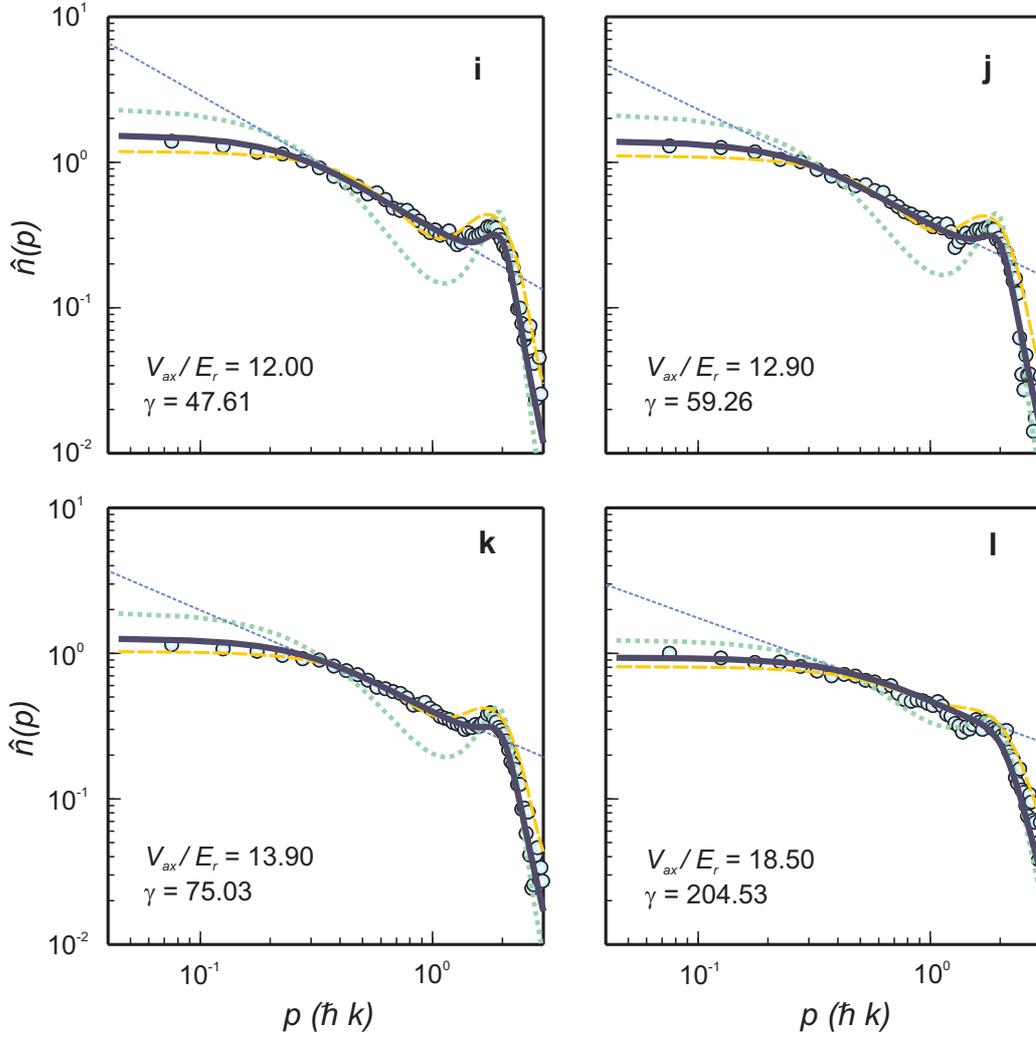
Figure 8.7: (continuation of figure 8.6) In plot (d) the momentum profiles for the ideal Bose gas (green lines) are also displayed for different temperatures and particle numbers in the central tube of $k_B T/J = 3.7$, $N_{0,0} = 16$ (dash-dotted green line) and $k_B T/J = 0.75$, $N_{0,0} = 20$ (dashed green line). The lattice depths and the slopes α of the linear part of the momentum profiles are summarized in the table 8.4.3 together with the calculated temperatures for a Tonks gas, an ideal Fermi gas and an ideal Bose gas.

Fig.	Lattice depth (E_R)	Slope	Tonks and Ideal Fermi Gas $(k_B T/J)$	Ideal Bose Gas $(k_B T/J)$
(a)	4.6	1.9	0.5	1.1
(b)	5.6	1.73	0.56	1.25
(c)	6.5	1.58	0.62	1.41
(d)	7.4	1.44	0.69	1.58
(e)	8.3	1.31	0.77	1.77
(f)	9.3	1.17	0.87	2.02
(g)	10.2	1.05	0.99	2.27
(h)	11.1	0.95	1.13	2.56
(i)	12.0	0.84	1.29	2.90
(j)	12.9	0.75	1.49	3.29
(k)	13.9	0.66	1.76	3.82
(l)	18.5	0.59	3.93	8.0

Table 8.1: The lattice depths and slopes α of the linear part of the momentum profiles shown in figures 8.5, 8.6 and 8.7. Also shown are the calculated temperatures for a Tonks gas, an ideal Fermi gas and an ideal Bose gas.

Chapter 9

Quantum Phases of Trapped Ions in an Optical Lattice

The merging of atomic physics and condensed matter physics has opened exciting new perspectives for the creation and manipulation of quantum states of matter. For example, cold atoms in optical lattices are a setup which allows experimentalists to simulate quantum many-body lattice systems [7, 83]. In recent years, trapped ions have also been proposed as an experimental system where a rich variety of quantum many-body models can be implemented [94, 173, 122, 121, 31]. The advantage of trapped ions is that we profit from the technology that has been developed for quantum information processing [73, 78, 55, 132, 144, 116]. In particular, it is possible to measure and manipulate the system at the single-particle level.

So far, previous proposals fall into two categories: (i) effective-spin models, in which the motion of the ions induces an effective interaction between internal levels [173, 122, 30], and (ii) interacting-Boson models, in which the vibrations (phonons) play the role of interacting particles [121, 31]. In this work we show that these proposals may be scaled up to a wide range of spatial dimensions, geometries, and particle interactions by placing the ions in a regular structure. This structure may be induced by optical lattices or by an array of ion microtraps.

The presence of the trapping structure offers us a way to increase the dimensionality of the system beyond the traditional linear Paul trap scheme. Further, it also opens up new possibilities for controlling particle interactions. On one hand, since ions are tightly confined by individual trapping potentials, their motion in any spatial direction can be used to induce spin–spin interactions which decay with the third power of the distance. This situation is to be compared with the case of Coulomb crystals confined in an overall trapping potential, where vibrational phonons with small wavevector, cor-

responding to highly collective vibrations, have a low-energy spectrum and induce infinite-range spin–spin interactions only [122]. On the other hand, in the optical lattice trapping scheme, we can control the anharmonicities of the trapping potentials and engineer effective phonon–phonon interactions. Thus, vibrational degrees of freedom may follow a Bose–Hubbard model along the lines of Ref. [121].

The realization of a periodic trapping potential with an optical lattice is a standard experimental method. In this work we focus on the study of the quantum many-body phases which arise in such experimental setups. We discuss two limiting cases. First, the case of small anharmonicities, and the effective quantum spin models which can be implemented by using the ion motion as a medium for inducing spin interactions among internal degrees of freedom. Second, we discuss in more detail the ground vibrational state in trapping schemes in which large anharmonicities induce phonon–phonon interactions and allow mapping hard-core phonons onto $S = 1/2$ spins. We focus on the case of periodic trapping potentials with interesting geometries, e.g., the triangular lattice. This case provides us with a playground for studying frustrated quantum magnets in a clean experimental setup. In this way, trapped ions allow us to implement models which have attracted much attention in condensed matter physics.

9.1   Microtraps

The starting point for all of the models in this work is a set of ions trapped in individual microtraps. Such traps have been proposed in the literature to be micro-fabricated, e.g., on surfaces [22], which allows for arbitrary geometries of the resulting ion "crystal" and, in principle, gives the experimentalist great control over the effective anharmonicity of the spatial ion motion near the microtrap minima.

We propose an alternative scheme for creating microtrap potentials, post-poning detailed calculations to a further publication [133]. Optical lattices have been used extensively in experiments with cold atoms, which interact mostly on short length scales and can populate d-dimensional lattices densely. If a d-dimensional Wigner crystal, assembled in an electromagnetic trap, is subjected to a sufficiently strong optical lattice potential, the spatial motion of each ion is restricted to a region near the minimum of the lattice well closest to the crystal equilibrium position. However, the effective amplitude of a realistic optical lattice is much smaller than the repulsion of two ions in the same or even neighboring lattice wells. Therefore, as opposed to experiments with cold atoms, the optical lattice will be very sparsely populated

with ions, but their strong interactions over large distances are nevertheless sufficient for experimentally exploring the models presented in Section 9.3. Depending on the stiffness of the Wigner crystal used as a starting point, the optical lattice does not need to be so strong as to trap the ions by itself; it is sufficient that the zero-point motion of the Wigner crystal is reduced by the optical lattice (since the optical lattice increases the effective mass of the ions) to the point where each ion is constrained to moving within a single lattice minimum.

As we have already mentioned, many interesting models require significant phonon–phonon interactions (see Section 9.2.3). The anharmonicity of the Coulomb interaction in a Wigner crystal is insufficient for observing these phenomena, and a harmonic normal-mode analysis captures the full physics of low-energy ion motion. We can make use of the natural anharmonicity of the sinusoidal optical lattice potential to introduce significant phonon–phonon interactions. For a strong monochromatic optical lattice, the ions are forced to the lattice minima, where the quartic anharmonicity is negative and corresponds to an effective phonon–phonon attraction. Much more interesting phases result from repulsive phonon–phonon interactions, which can be achieved by using an optical superlattice [43, 133]. In what follows we assume such repulsive phonon–phonon interactions, irrespective of how the microtraps are put in place.

9.2 Varying the Anharmonicity

This section describes three regimes of anharmonicities of the microtraps. If the anharmonicities are negligible, the internal degrees of freedom of trapped ions can be made to interact via dipolar phonon-mediated couplings. At the opposite end, for strong anharmonicities the quantized vibrational modes themselves describe a $S = 1/2$ spin model with XY interactions. In the intermediate regime, the vibrational motion of the ions can be effectively described by an interacting Bose–Einstein condensate.

9.2.1 No anharmonicity: short-range lattice Hamiltonians

In Ref. [122] a model is elaborated where internal states of trapped ions represent effective $S = 1/2$ spin degrees of freedom. In this model, the vibrational modes of a self-assembled ion crystal in a harmonic trap mediate variable interactions between the effective spins, allowing for controllable interactions in all spin directions. A drawback of the proposed architecture is that the

longitudinal vibrational modes, where the ion crystal moves as a whole in the ion trap, are naturally slow ("floppy" modes) and lead to long-range ferromagnetic interactions. This limits the generality of the Hamiltonians that can be constructed with such crystals of trapped ions.

If, however, local microtraps are added to the confining potential, then this problem can be overcome by increasing the potential energy curvature in *all* directions of motion of the individual trapped ions. In the simplest case, adding the same isotropic harmonic microtrap potential to each ion, the dispersion and shape of normal modes of the ion crystal are unchanged except for an overall shift in frequency corresponding to the curvature of the microtraps. Such a frequency shift renders the vibrational modes "stiff" for all three spatial directions of each ion. Consequently the effective spin-$\frac{1}{2}$ degrees of freedom of the trapped ions can be made to interact through Ising, XY, or XYZ couplings, all of which have adjustable amplitudes and decay as r^{-3} since they stem from the dipole–dipole interactions of the ionic vibrations. Ref. [122] further shows that if the phonon modes have only finite stiffness, then next-nearest neighbor interactions can be suppressed, approaching effective nearest-neighbor Hamiltonians on arbitrary lattice geometries.

9.2.2 Small anharmonicity: interacting Bose–Einstein condensate

The vibrational motion of a self-assembled ion crystal in a global trap is very well approximated by a harmonic model, as was used in Sec. 9.2.1. At low energies, cubic terms of the Coulomb interaction are unimportant because the three-phonon processes they describe are highly nonresonant. Quartic terms are smaller than the quadratic terms by roughly a factor of $(\zeta/d_0)^2$, where ζ is the zero-point motion amplitude and d_0 the inter-ion distance [129]. Since in realistic self-assembled trapped ion crystals $\zeta \ll d_0$, quartic terms (phonon–phonon interactions) and higher-order interactions can be safely neglected.

This picture changes when microtraps are added to the local potentials of the individual ions. In addition to the harmonic confinement, these microtraps can add significant anharmonicities U_α to the ionic vibrations. As discussed in Refs. [121, 31], the spatial motion of trapped ions thus behaves like a Bose–Hubbard model of phonons, with Hamiltonian

$$\mathcal{H}_{\text{BH}} = \sum_{\langle \alpha,\beta \rangle} t_{\alpha,\beta}(a_\alpha^\dagger a_\beta + \text{h.c.}) + \sum_\alpha U_\alpha n_\alpha(n_\alpha - 1) + \sum_\alpha V_\alpha n_\alpha, \qquad (9.1)$$

where the indices α, β run over the $3N$ eigen-directions of motion of the N ions. Here we assume that the quartic phonon–phonon interaction terms (an-

harmonicities) do not couple different modes, even if the modes are localized on the same ion. This decoupling occurs naturally in a cubic optical lattice; however, irrespective of the microtrap geometry, we will assume throughout this work that of the three directions of motion of each ion, only one is "active" and contributing to the models we wish to study, while the other two modes are off-resonant and do not influence the low-energy dynamics of the active mode. This is achieved with strongly anisotropic prolate microtraps, where one slow direction of motion is decoupled from the two fast directions of motion.[1] For example, in a three-dimensional cubic optical lattice where one standing wave is much weaker than the other two, every lattice minimum constitutes such a prolate microtrap.

Calling $\vec{m}_\alpha$ the direction of motion of the αth ion, the effective tunneling matrix elements of the phonons are of the dipolar form

$$t_{\alpha,\beta} = \frac{\zeta_\alpha \zeta_\beta e^2}{8\pi\varepsilon_0 r_{\alpha,\beta}^3}[\vec{m}_\alpha \cdot \vec{m}_\beta - 3(\vec{n}_{\alpha,\beta} \cdot \vec{m}_\alpha)(\vec{n}_{\alpha,\beta} \cdot \vec{m}_\beta)], \qquad (9.2)$$

where $e^2/(4\pi\varepsilon_0)$ is the electrostatic coupling strength, $\vec{r}_{\alpha,\beta} = \vec{r}_\beta^{(0)} - \vec{r}_\alpha^{(0)}$ are the equilibrium inter-particle spacings, and $\vec{n}_{\alpha,\beta} = \vec{r}_{\alpha,\beta}/r_{\alpha,\beta}$. The length scales ζ_α are those of the harmonic-oscillator motion in the quadratic component of the local microtrap potentials, related to the local potentials as $\zeta_\alpha = \hbar/\sqrt{mV_\alpha}$, where m is the mass of the ions. In a homogeneous lattice of microtraps, where all $\vec{m}_\alpha$ are equal, the angular dependence of Eq. (9.2) is proportional to the Legendre polynomial $t_{\alpha,\beta} \propto -P_2(\vec{n}_{\alpha,\beta} \cdot \vec{m})$. In the following sections, we will focus our attention on the central region of the trap, where the tunneling coefficients $t_{\alpha,\beta}$ and local potentials V_α are sufficiently isotropic to be approximated by a translationally invariant model.

In the absence of anharmonicities ($U_\alpha = 0 \ \forall \alpha$), the Hamiltonian (9.1) can be easily diagonalized. Irrespective of the signs of the tunneling matrix elements $t_{\alpha,\beta}$, there will be a lowest-energy normal mode z (possibly degenerate by symmetry). The ground state in the canonical ensemble of fixed phonon number n is simply $(n!)^{-1/2}(b_z^\dagger)^n|\text{g}\rangle$, which can be interpreted as a Bose–Einstein condensate (BEC) of phonons in mode z.

The BEC analogy can be extended to small but nonzero phonon–phonon interactions U_α. With the canonical transformation $a_\alpha = \sum_k \Gamma_{\alpha,k} b_k$ that diagonalizes the harmonic part of the Hamiltonian (i.e., describes the normal modes), the Hamiltonian is re-expressed as

$$\mathcal{H}_{\text{BH}} = \sum_k \tilde{V}_k n_k + \sum_{k_1,k_2,k_3,k_4} U_{k_1,k_2}^{k_3,k_4} b_{k_1}^\dagger b_{k_2}^\dagger b_{k_3} b_{k_4}, \qquad (9.3)$$

---

[1]Extensions of the present models to two or three ionic degrees of freedom are straightforward and do not introduce new physics if the degrees of freedom are separable.

with the coefficients $U_{k_1,k_2}^{k_3,k_4} = \sum_\alpha U_\alpha \Gamma_{\alpha,k_1}^* \Gamma_{\alpha,k_2}^* \Gamma_{\alpha,k_3} \Gamma_{\alpha,k_4}$ describing interactions between normal modes which deplete the BEC. When approximating the central region of the ion crystal by a quasi-infinite periodic d-dimensional lattice of N ions, the normal modes become Fourier modes

$$b_{\vec{k}} = N^{-1/2} \sum_j a_j \exp(-i\vec{k} \cdot \vec{r}_j).$$

The interaction of these modes conserves linear momentum:

$$\mathcal{H} = \sum_{\vec{k}} \hat{t}(\vec{k}) n_{\vec{k}} + U N^{-1} \sum_{\vec{k}_1,\vec{k}_2,\vec{k}_3,\vec{k}_4} b_{\vec{k}_1}^\dagger b_{\vec{k}_2}^\dagger b_{\vec{k}_3} b_{\vec{k}_4} \delta_{(\vec{k}_1+\vec{k}_2),(\vec{k}_3+\vec{k}_4)},$$

where $\hat{t}(\vec{k}) = \sum_{\vec{\delta}} t(\vec{\delta}) e^{i\vec{k} \cdot \vec{\delta}}$ are the Fourier transformed tunneling couplings, and $n_{\vec{k}} = b_{\vec{k}}^\dagger b_{\vec{k}}$. In this approximation, a small interaction U partly depletes the BEC at $\vec{k}_z$ and broadens the structure factor around this momentum component. The condensate depletion fraction is then [118]

$$\frac{n_{\text{ex}}}{n_0} = \frac{1}{N} \sum_{\vec{k} \neq \vec{k}_z} \frac{1}{2} \left(\frac{\hat{t}(\vec{k}) + 2U n_0}{\sqrt{[\hat{t}(\vec{k})]^2 + 4U n_0 \hat{t}(\vec{k})}} - 1 \right), \tag{9.4}$$

where $n_0 = n/N$ is the undepleted BEC density, and the dispersion relation is shifted such that $\hat{t}(\vec{k}_z) = 0$.

9.2.3   Large anharmonicity: spin-$1/2$ XY models

In the limit of strong repulsion $|U_\alpha| \gg |\sum_\beta t_{\alpha,\beta}| \, \forall \alpha$ and for low phonon filling $n < 1$, double phononic occupancy is strongly suppressed, and the system of phonons attains the hardcore limit, where phonons can be conveniently mapped onto $S = 1/2$ spins via the Holstein–Primakoff transformation $a_\alpha^\dagger \to S_\alpha^+$, $a_\alpha \to S_\alpha^-$, $n_\alpha \to S_\alpha^z + \frac{1}{2}$. For each ion, the vibrational ground state $|0\rangle$ is then mapped onto the spin state $|\downarrow\rangle$, and the lowest excited state $|1\rangle$ onto the state $|\uparrow\rangle$. The resulting spin Hamiltonian has the form of an XY model with long-range dipolar couplings and a site-dependent field:

$$\mathcal{H}_{\text{S}} = 2 \sum_{\langle \alpha,\beta \rangle} t_{\alpha,\beta}(S_\alpha^x S_\beta^x + S_\alpha^y S_\beta^y) + \sum_\alpha V_\alpha S_\alpha^z. \tag{9.5}$$

Any spin–spin couplings for the z components must derive from off-site density–density interactions between the phonons, namely from terms of the form $n_i n_j$. The only source of such interactions is the fourth-order terms

of the Coulomb interaction between the ions; as discussed in Section 9.2.2, they are smaller than the XY interaction by a factor of $(\zeta/d_0)^2$ and therefore negligible. Nonetheless the implementation of the Hamiltonian of Eq. (9.5) is of significant interest, because it offers the possibility of exploring the rich physics of frustrated XY spin models in various dimensions, with a fully tunable frustration. Detailed discussions of several such spin models and associated quantum phases and phase transitions are provided in the next section.

9.3 Frustrated XY Spin-$1/2$ Models

In this section we discuss several frustrated XY lattice spin models belonging to the family described by the Hamiltonian of Eq. (9.5) and realizable in linearly or planarly trapped ions. We henceforth assume for simplicity uniform local potentials $V_\alpha = V$ in the trapping region; under the condition of preparing the system with a well-defined number of phonons, we can then discard the field term in Eq. (9.5). Moreover we focus on a half-filled system of hardcore bosons, corresponding to the zero-magnetization sector of the Hilbert space for the spin system. In the case of bipartite lattices, the ground state of an XY antiferromagnet in this zero-magnetization sector can be rigorously shown to coincide with that of a (more common) XY antiferromagnet without magnetization constraints and in zero field [92]. As for frustrated lattices, this remains certainly true for finite-size systems, where no spontaneous breaking of the Z_2 symmetry of the Hamiltonian can occur.

We have focused on spin models with XY interactions, featuring full frustration for two equivalent (and non-commuting) spin components, a paradigm of quantum frustration. When using internal states of the ions to encode the spin variable (Section 9.2.1), the effective spin–spin interaction which arises is typically of Ising-like symmetry, and full frustration appears only for one spin component at a time. Fine tuning of the system parameters would be required to obtain a rotationally invariant Hamiltonian, *e.g.* in the XY plane. On the other hand, when spins are encoded in the phononic states of each ion (Section 9.2.3), the XY rotational symmetry is a robust property of the Hamiltionan, as it stems from the conservation of the number of phonons.

Linear chain. The Hamiltonian of Eq. (9.5) on a linear chain, obtained by strong transverse confinement of the ions, realizes an $S = 1/2$ one-dimensional XY antiferromagnet with dipolar interactions. If we neglect all interactions except nearest-neighbor ones, we recover an exactly solvable model [84] with power-law decaying correlations in the ground state,
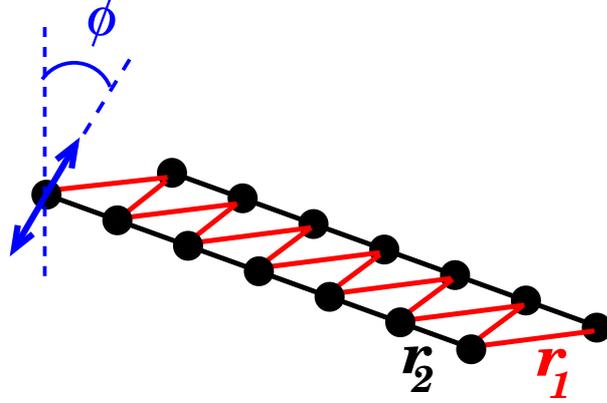
Figure 9.1: The zig-zag ladder with inter-chain distances $r_1 = d_0\sqrt{1+\xi^2}$ and intra-chain distances $r_1 = 2d_0$. The motions of the ions in the direction $\vec{m}$ of the blue arrow are coupled to form a spin lattice model.

$\langle S_i^z S_{i+r}^z \rangle \sim r^{-2}$ and $\langle S_i^x S_{i+r}^x \rangle \sim r^{-1/2}$. Long-range dipolar tunneling simply modifies the decay exponents [30], leading to a faster decay of $\langle S_i^x S_{i+r}^x \rangle$ and to a slower decay of $\langle S_i^z S_{i+r}^z \rangle$.

Zig-zag ladder. A richer physics emerges in the case of a zig-zag ladder of ions, which develops naturally for weaker transverse confinement of the ions [6, 131]. Assuming longitudinal inter-ion spacing d_0 and a zig-zag amplitude $\xi \times d_0$, inter-chain neighboring ions are distant by $r_1 = d_0\sqrt{1+\xi^2}$ and intra-chain neighbors by $r_2 = 2d_0$ (see Fig. 9.1). The relevant phonon direction of motion $\vec{m}$ in Eq. (9.2) is taken perpendicular to the main trap axis and at an angle φ from the ion plane normal. Hence the ratio between the dominant intra-chain (t_2) and inter-chain (t_1) couplings is

$$R = \frac{t_2}{t_1} = \frac{1}{8} \times \frac{(1+\xi^2)^{5/2}}{1 - \frac{1}{2}\xi^2(1 - 3\cos 2\varphi)}. \tag{9.6}$$

In trapped-ion experiments with cylindrically symmetric traps, at $\xi \approx 0.965$ spontaneously generated zig-zag ladders deform into helices [131]. For $\varphi = 0$ (out-of-plane vibrational motion) this limits the range of easily accessible coupling ratios to $R \lesssim 0.335$. In practice, larger amplitudes ξ (and hence a larger R) can be engineered by breaking the cylindrical symmetry of the trap and constraining the ions to two dimension, or by microtrap stabilization [26]. However, choosing $\varphi = \frac{\pi}{2}$ instead (in-plane vibrational motion) gives access to all ratios $R > 1/8$ for $\xi < 1/\sqrt{2}$. In what follows we therefore assume in-plane vibrational motion. We use ξ and R interchangeably through Eq. (9.6).
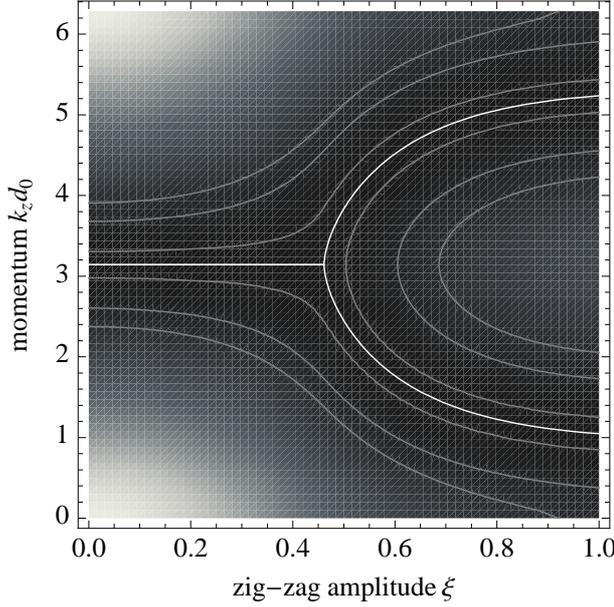
Figure 9.2: Dispersion $\hat{t}(k)$ of normal modes in an infinite zig-zag ladder with dipolar couplings ($\varphi = \frac{\pi}{2}$). The white line traces the minimum as a function of the zig-zag amplitude ξ.

Figure 9.2 shows the normal-mode dispersion relation in the zig-zag ladder. For small zig-zag amplitudes $\xi < \hat{\xi}_{\text{dipole}}^{\text{classical}} = 0.461$ ($R < 0.353$) the normal-mode dispersion $\hat{t}(k)$ has a unique minimum at $k_z d_0 = \pi$, corresponding to Néel order; but for $\xi > \hat{\xi}_{\text{dipole}}^{\text{classical}}$ this minimum bifurcates into two symmetric minima at $k_z^{\pm} d_0 = \pi \pm q(\xi)$, corresponding to spiral order. This is to be compared with a similar result for the system with intra-chain and inter-chain nearest-neighbor couplings only ($\{t_1, t_2\}$ system), where the transition from Néel to spiral order occurs at a smaller value of $R = 1/4$ in the limit of classical XY spins [58]. A spiraling ground state is endowed both with spontaneous magnetic order, namely the breaking of the rotational symmetry in spin space, and with *chiral* order, corresponding to the choice of helicity of the spiraling state.

In a quasi-1D system we define the chirality as [63]

$$\kappa_i = 4(S_i^x S_{i+1}^y - S_i^y S_{i+1}^x), \tag{9.7}$$

where the sites i and $i + 1$ belong to different chains. A striking result in quantum systems is that chiral order can survive even when magnetic order disappears. In fact, the $\{t_1, t_2\}$ XY zig-zag ladder with $S = \frac{1}{2}$ is found in Ref. [63] to exhibit power-law decaying spin–spin correlations for all values
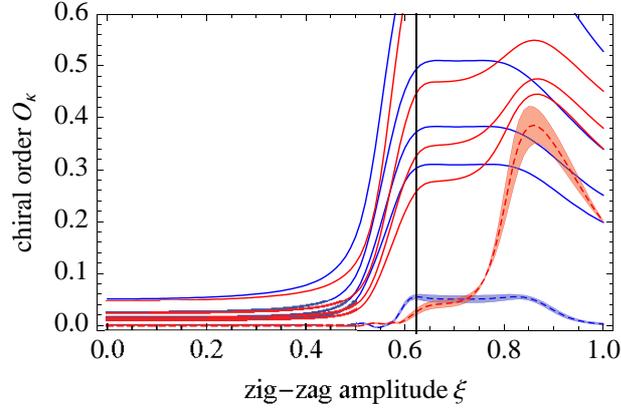
Figure 9.3: The chiral order parameter O_κ from Eq. (9.8b) in the ground state of the zig-zag ladder ($\varphi = \frac{\pi}{2}$), for the $\{t_1, t_2\}$ model (blue) and long-range dipolar interaction (red), computed from exact diagonalizations (Arnoldi) with $L = 8, 12, 16, 20$ spins (top to bottom). The shaded bands indicate 2σ regions of the extrapolation to infinite system size by least-squares fits including L^{-1} and L^{-2} corrections. The vertical line indicates the transition point to long-range chiral order in the $\{t_1, t_2\}$ model, estimated from DMRG calculations [63]

.

of R, but it is also found to develop long-range chiral order for $R > 1.26$. We extend the calculation of Ref. [63] to an XY ladder with dipolar interactions, making use of exact diagonalization up to sizes $L = 20$. We define an order parameter for the chiral phase as the averaged chiral correlation over all pairs of the system:

$$O_\kappa^\Delta = \frac{1}{L - 1 - |\Delta|} \sum_i \langle \kappa_i \kappa_{i+\Delta} \rangle \qquad (9.8a)$$

$$O_\kappa = \frac{1}{2L - 3} \sum_{\Delta = -(L-2)}^{L-2} O_\kappa^\Delta. \qquad (9.8b)$$

Fig. 9.3 shows this chirality order parameter as a function of the zig-zag amplitude. For the $\{t_1, t_2\}$ model, we confirm a relatively sharp transition to a chirally ordered state for $\xi \approx 0.59$ (corresponding to $R \approx 0.9$), consistent with the transition of Ref. [63]. The full long-range dipolar model essentially retains this transition, shifted to slightly higher zig-zag amplitudes ($\xi \approx 0.63$), along with what seems like a reorientation transition around $\xi \approx 0.8$ with significantly higher chiral order, which is not observed in the classical limit. At present we do not provide a description of the phase $0.8 < \xi < 1$, but we
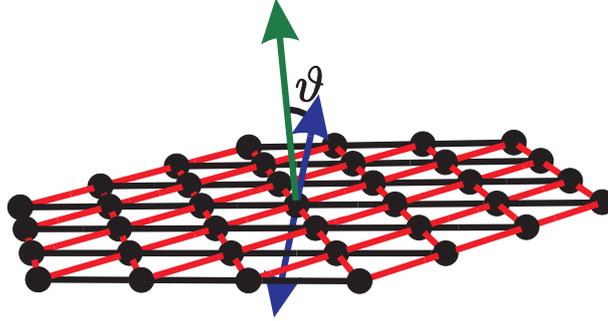
Figure 9.4: Ion vibrational motion in the triangular lattice. The black (red) lines show the t_1 (t_2) interactions in the τ_1 (τ_2) directions. Blue is a possible direction of motion $\vec{m}$, perpendicular to the τ_1 direction and forming an angle ϑ with the surface normal (green arrow).

point out that despite the perturbative appearance of the dipolar interaction tails, they change the phase diagram of this zig-zag ladder drastically. This effect is currently the subject of further study.

Triangular lattice. When put in a planar trap, ions self-assemble into a triangular-lattice Wigner crystal [95]. Adding an optical lattice to this setup, the degrees of freedom associated with the strongly non-linear vibrational motion in the lattice minima can realize a large family of spatially anisotropic XY triangular antiferromagnets. Unlike the case of the zig-zag ladder, we consider fixed average ion positions here, and the model parameters are varied by tilting the direction of motion of the ions $\vec{m}$ with respect to the lattice normal. We further assume that $\vec{m}$ remains perpendicular to one of the lattice directions, indicated by τ_1, and makes an angle ϑ with the lattice normal (see Fig. 9.4).

For $\vartheta = 0$ the model of Eq. (9.5) realizes an isotropic triangular XY antiferromagnet with dipolar couplings, and it is maximally frustrated. For this system the minima of the normal-mode dispersion are on the corners of the hexagonal first Brillouin zone, corresponding in the classical limit to the well-known three-sublattice ordered state with 120° angles between the spin directions on the sublattices [see Fig. 9.5(a)].

A nonzero angle ϑ produces a spatial anisotropy in the couplings, leaving the intra-chain couplings along the τ_1-axis unchanged while modifying the transverse (inter-chain) couplings. The value $\vartheta \approx 31°$ produces the minimum effective interaction between the τ_1-chains, in the sense that the normal-mode dispersion $\hat{t}(\vec{k})$ is least corrugated in the direction perpendicular to τ_1. We note that $\vartheta = 31°$ is also the point where the BEC depletion of Eq. (9.4) grows
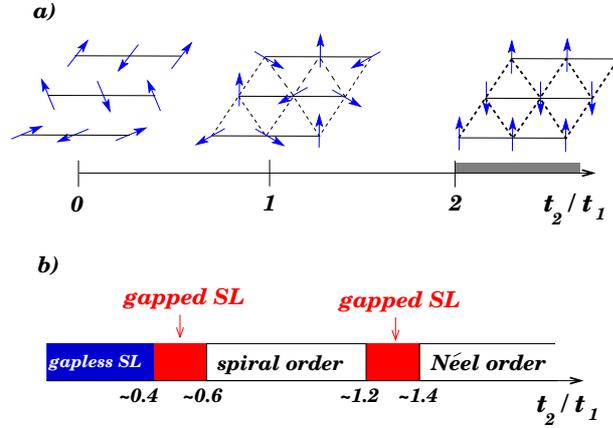
Figure 9.5: Phase diagram of the S=1/2 XY antiferromagnet on the spatially anisotropic triangular lattice ($\{t_1, t_2\}$ model). a) Classical spin ordering: decoupled Néel-ordered horizontal (τ_1) chains for $t_2/t_1 = 0$; three-sublattice ordering for $t_2/t_1 = 1$; Néel order on the t_2 lattice for $t_2/t_1 \geq 2$. b) Proposed quantum phase diagram for $S = 1/2$ spins, including three spin-liquid (SL) phases.

fastest with U, approximating the 1D limit where the BEC is fully depleted for any nonzero interaction U. At $\vartheta \approx 42°$ the nearest-neighbor inter-chain coupling vanishes, while residual weaker couplings to further neighbors survive due to the long-range nature of the dipolar interaction. On the opposite end, a value of $\vartheta = \frac{\pi}{2}$ maximizes the inter-chain nearest-neighbor interaction. Thus by rotating the direction of vibration $\vec{m}$ with respect to the lattice plane we produce a similar effect to that produced in the zig-zag ladder by deformation of the Coulomb crystal. This different method is necessary because tuning the interaction coefficients in the effective spin Hamiltonian by mechanical deformation of the ion crystal is problematic, due to the significant stiffness of a two-dimensional Wigner crystal. The two approaches could possibly be combined in order to cover a larger range of system parameters.

At the classical level, varying ϑ from zero continuously deforms the three-sublattice structure of the ground state of the isotropic triangular antiferromagnet, shifting the peaks in the structure factor away from the corners of the first Brillouin zone. For both zero and nonzero ϑ, the classical ground state has a finite vector chirality, defined on a plaquette with counter-clockwise labeled corners (i, j, k) as [71]

$$\kappa_\triangle = \frac{2}{3\sqrt{3}}[\vec{S}_i \times \vec{S}_j + \vec{S}_j \times \vec{S}_k + \vec{S}_k \times \vec{S}_i]_z, \qquad (9.9)$$
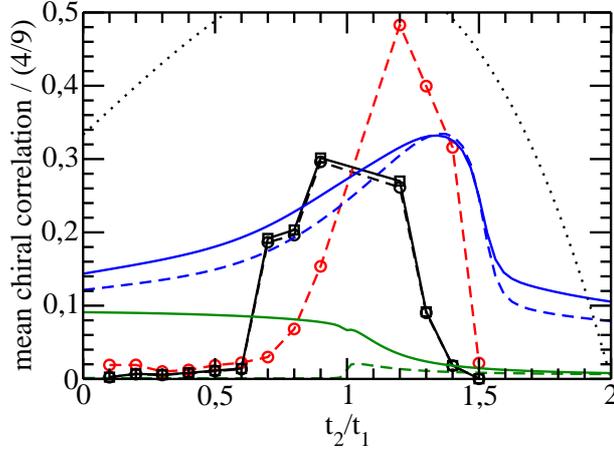
Figure 9.6: Ground-state vector-chirality correlations $\psi_-/\hat{\psi}_-$ from Eq. (9.10), given in terms of the theoretical maximum $\hat{\psi}_- = \frac{4}{9}$. Plotted here are the correlations with the central plaquette pair, averaged over the simulation volume. Black: PEPS 20x20 with $D = 2$. Red: PEPS 10x10 with $D = 3$. Blue: exact diagonalization (Arnoldi) 4x4. Green: exact diagonalization 4x4, periodic boundary conditions. Solid lines, squares: plaquette pairs share a t_1 link; dashed lines, circles: plaquette pairs share a t_2 link. Points around $t_2/t_1 = 1$, where the system is maximally frustrated, have been excluded from the PEPS results due to poor convergence. The black dotted line is the classical result.

and long-range chirality correlations, defined on plaquette pairs as [128]

$$\psi_- = \langle (\kappa_\triangle - \kappa_\triangledown)(\kappa_{\triangle'} - \kappa_{\triangledown'}) \rangle, \tag{9.10}$$

where the plaquette pairs $(\triangle, \triangledown)$ and $(\triangle', \triangledown')$ each share two spins. We find that even in the quantum model it is numerically irrelevant which edge is being shared (along the τ_1 or a τ_2 direction), as shown in Fig. 9.6.

In the quantum limit $S = 1/2$ we neglect the long-range dipolar tail of interactions, restricting our attention to the case of nearest-neighbor intra-chain (t_1) and inter-chain (t_2) couplings. According to the previous discussion on the dependence of inter-chain couplings upon the angle ϑ, one can experimentally span the range of parameter ratios $0 < |t_2/t_1| < 5/4$; the sign of t_2/t_1 is of no relevance since it can be reversed by a π rotation of every other τ_1-row of spins [with a corresponding modification to Eq. (9.9)]. We have done calculations up to $t_2/t_1 = 3/2$, which may be experimentally accessible by minor deformations of the Wigner crystal. Numerical treatment of the two-dimensional model with exact diagonalization is restricted to very small lattices, while other approaches such as quantum Monte Carlo are hindered

by the sign problem due to frustration. We hence resort to a variational calculation based on projected-entangled pair states (PEPS) [154, 101], which allow us to look at much larger lattices than with exact diagonalization. The calculations are performed on rhombic 10x10 and 20x20 lattices with open boundary conditions; such boundary conditions, while being essentially inherent to the PEPS method, are particularly welcome in a system developing incommensurate spiraling order due to frustration, and they moreover mimic the natural boundary conditions realized experimentally in a finite Coulomb crystal. Due to the significant scaling of the computational effort with the bond dimension D of the variational PEPS basis, we limit ourselves to the smallest bond dimensions ($D = 2, 3$) going beyond the mean-field limit $D = 1$. Despite this aspect we still capture dramatic quantum features due to the interplay between frustration and quantum fluctuations.

In Fig. 9.6 we report the evolution of chiral order upon increasing the spatial anisotropy in the couplings. We observe strong indications for the breakdown of chiral order around $t_2/t_1 \approx 0.6$ and $t_2/t_1 \approx 1.3$ via quantum phase transitions. Indeed, at the classical level long-range chiral order is expected for all $t_2/t_1 < 2$, as it is associated with the a spiral state with a well defined helicity of the spirals; chiral order is expected to vanish only for $t_2/t_1 \geq 2$ (square lattice XY antiferromagnet). Quantum mechanically, the limits $t_2 = 0$ and $t_2/t_1 \to \infty$ are well known to give a spin liquid with algebraically decaying correlations, as already mentioned above, and long-range Néel order [45], respectively. The way these two limits are attained is nonetheless highly non-trivial, as clearly shown by the evolution of spin–spin correlations upon changing t_2/t_1. In the following we will focus on the spin–spin correlations along the τ_1 direction (of the t_1 couplings) and along the τ_2 direction (of the t_2 couplings). In particular, we indicate with (i, j) the position of a point in the (τ_1, τ_2) reference system, and for any inter-site separation δ we average over all pairs of sites at a distance of δ, along τ_1 and τ_2. For instance, for correlations along τ_1, we define in analogy to Eq. (9.8a)

$$\langle S_{i,j} S_{i+\delta,j} \rangle = \frac{1}{N_\delta} \sum_{(i,j)_\delta} \langle S_{i,j} S_{i+\delta,j} \rangle, \tag{9.11}$$

where N_δ is the number of sites $(i, j)_\delta$ in the sum for which $(i + \delta, j)$ is also within the simulation cell. Fig. 9.7 shows the spin–spin correlations for different values of t_2/t_1. The correlations along the τ_2 axis build up very slowly upon increasing t_2/t_1, and they become significant only for $t_2/t_1 \approx 0.7$, consistently with the appearance of chiral order as observed in Fig. 9.6. Hence in the interval $0 < t_2/t_1 \lesssim 0.6$ the interplay between quantum fluctuations and frustration leads to an effective decoupling between the τ_1 chains. What
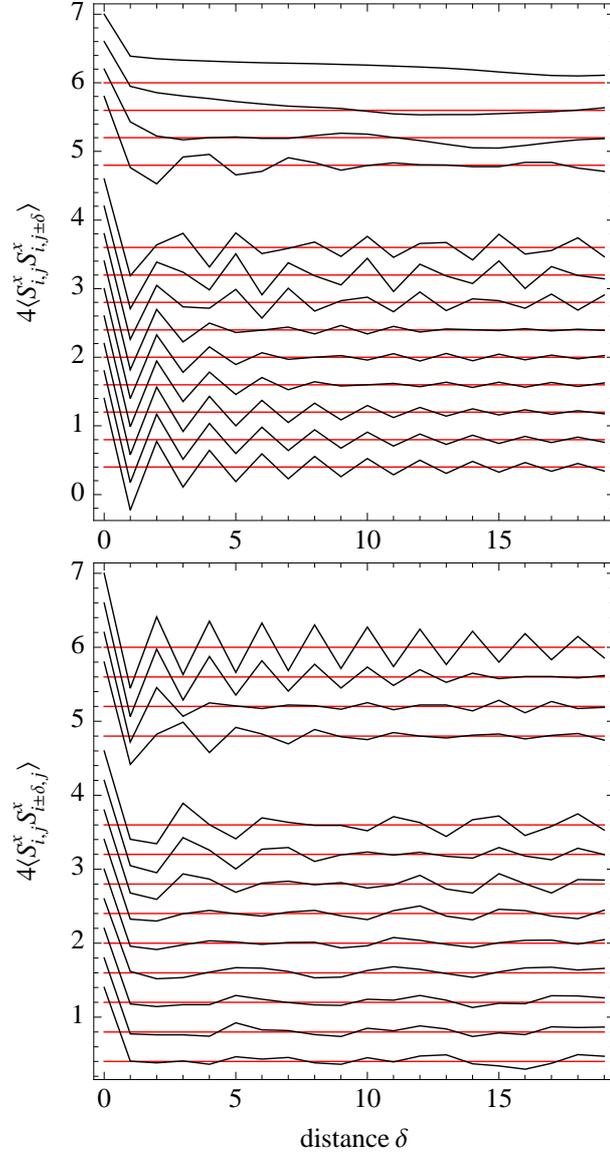
Figure 9.7: Ground-state spin–spin correlation functions $4\langle S^x_{i,j} S^x_{i+\delta i,j+\delta j}\rangle$ along the τ_1-direction (top, along t_1 bonds) and along the τ_2 direction (bottom, along t_2 bonds), averaged over the simulation volume as in Eq. (9.11). Values of t_2/t_1 are $\{0.1, 0.2, 0.3, 0.4, 0.5, 0.6, 0.7, 0.8, 0.9, 1.2, 1.3, 1.4, 1.5\}$ from bottom to top, with the red lines indicating the shifted reference lines of zero correlations. Points around $t_2/t_1 = 1$, where the system is maximally frustrated, have been excluded due to poor convergence of the PEPS calculations. Simulation size was 20×20 with bond dimension $D = 2$.
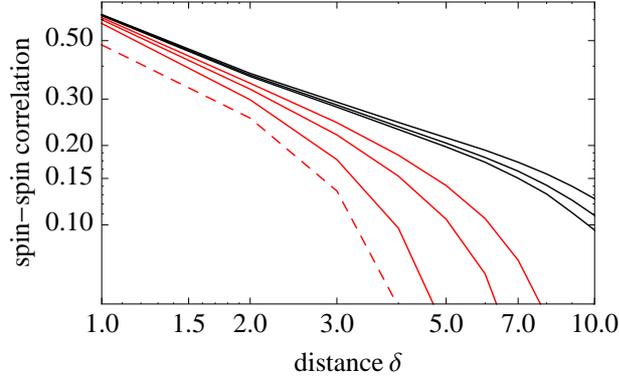
Figure 9.8: Solid lines: comparison of the lowest six curves of the upper panel of Fig. 9.7: τ_1 structure factors $4(-1)^\delta \langle S_{i,j}^x S_{i,j\pm\delta} \rangle$ for $t_2/t_1 = \{0.1, 0.2, 0.3, 0.4, 0.5, 0.6\}$ from top to bottom. Fits to the short-range part $(2 \leq \delta \leq 5)$ reveal a transition from polynomial (black) to exponential (red) decay around $t_2/t_1 \approx 0.4$. Dashed line: τ_2 structure factor $4(-1)^\delta \langle S_{i,j}^x S_{i\pm\delta,j} \rangle$ for $t_2/t_1 = 1.3$, showing exponential decay.

is then the state along each τ_1-chain? Its evolution with increasing t_2/t_1 is absolutely non-trivial and completely dominated by quantum effects. In fact, classically a staggered ordering appears along each chain for $t_2 = 0$ and it turns continuously into (generally incommensurate) spiraling order for any finite t_2. The spiral order reproduces the three-sublattice structure of an isotropic triangular lattice for $t_2 = t_1$, and it realizes Néel order on the t_2-lattice when $t_2/t_1 \geq 2$. This evolution is sketched in Fig. 9.5(a). Quantum mechanically, on the other hand, for $t_2/t_1 \ll 1$ the dominant correlations along each chain remain antiferromagnetic, and the decay of correlations becomes *stronger* for larger t_2: as shown in Fig. 9.8, the decay is initially of the type $1/r^{K/2}$ with $K = 1$ at $t_2 = 0$. K is seen to grow upon increasing t_2: the two-dimensional system hosts a one-dimensional Luttinger-liquid state on each of the τ_1-chains, with a non-universal K exponent. Even more strikingly, the algebraically decaying staggered correlations turn to exponential decay for $0.4 \lesssim t_2/t_1 \lesssim 0.6$, where the state on each chain evolves from a gapless to a gapped spin liquid. Only upon increasing t_2/t_1 further we observe that long-range correlations build up again, this time with a spiraling structure.

When increasing t_2/t_1 above 1, a similarly non-trivial evolution of correlations takes place. We observe that the loss of chiral order, occurring at $t_2/t_1 \approx 1.3$, is accompanied by a loss in correlations along the τ_2 direction, rendering the τ_1-chains again effectively decoupled. The state along each τ_1-chain appears to be again a gapped spin liquid, with exponentially

decaying correlations. It is only for $t_2/t_1 \approx 1.5$ that the system exhibits long-range correlations in both the τ_1 and τ_2 directions, the latter of which already exhibits a full Néel structure. Fig. 9.5(b) summarizes our quantum phase diagram based on PEPS calculations, which exhibit three spin-liquid phases: a gapless one and two gapped ones. The inclusion of long-range dipolar interactions, which physically arise in the ion system, is at present technically challenging; however, we expect the long tail of interactions to give only small corrections to phases which develop a finite gap in the spectrum or finite long-range order in the model limited to short-range couplings, as is the case for most phases in Fig. 9.5(b).

The study of quantum antiferromagnetism on the anisotropic triangular lattice has recently attracted a deep interest in the case of Heisenberg interactions, in connection with the physics of quasi-2D antiferromagnets such as Cs_2CuCl_4 [28]. In particular, a similar phase diagram to the one presented in Fig. 9.5(b) has been obtained in Ref. [174] by variational calculations. It is extremely intriguing to observe that one of the most striking features of the phase diagram predicted for the Heisenberg case [174], namely the emergence of intermediate gapped spin-liquid phases in the system, is also present in the case of XY interactions. Hence the evolution from a 1D gapless spin liquid to a spiraling ordered state, and from spiral to Néel order, apparently acquires a "universal" discontinuous structure: instead of a continuous deformation of correlations in the ground state, exhibited by the classical system, the quantum system first shows a complete loss of (quasi-)long-range correlations in favor of a short-range spin-liquid state, and then a revival of correlations at a different wavevector.

9.3.1 Preparation of the half-filled system

The results for the spin models in this section assume a ground state with zero total magnetization, which corresponds to a phonon model with population $N/2$ assuming N active degrees of freedom. Such a state may be more easily prepared in the absence of anharmonicities, as a BEC of phonons described in Section 9.2.2. The optical lattice constituting the microtraps is subsequently switched on adiabatically, which transforms the BEC into the half-filled ground state of the Bose–Hubbard Hamiltionian (9.1) and, for very large anharmonicities, into that of the $S = 1/2$ spin model.

The phonon BEC at the starting point of this adiabatic passage cannot be prepared by cooling a thermal population of phonons, since their number is not conserved during the cooling process. Instead, we propose that the harmonic trap holding the ion crystal is opened to the point where just the lowest-frequency vibrational mode becomes soft. In a linear chain, for exam-

ple, we open the radial confinement to the point where the chain acquires a small zig-zag amplitude [6, 131]. The ion crystal is then cooled to its vibrational ground state in the new symmetry-broken configuration, after which the trap is rapidly closed to its original state. Depending on the amplitude of this symmetry breaking, the final state of the system is a coherent state of phonons in the lowest-frequency mode. In a sufficiently large system, adjusting the mean number of phonons to the half-filling point results in a coherent state which is not very far from a Fock state of exactly half filling.

Chapter 10

Conclusions

In summary, two specific examples of "analog" quantum simulators have been discussed in this part.

In chapter 8, a method to realize a Tonks–Girardeau gas by means of an optical lattice has been described. This method has been implemented experimentally and the experimental data has been compared to our theoretical predictions. It has been shown that the bosonic atoms exhibit a pronounced fermionic behaviour and show a momentum distribution that is in excellent agreement with a theory of fermionized trapped Bose gases.

In chapter 9, a variety of quantum many-body Hamiltonians realized by the anharmonic vibrations of ions trapped in the wells of a deep optical lattice has been presented. While the dominant Coulomb interaction and the overall trapping potential determines the geometry of the ionic Wigner crystal, the optical lattice allows to engineer the phononic states for the ions and it endows the system with a broad range of tunability. On the one hand, one can control the effective on-site repulsion/attraction of the phonons by modifying the optical lattice potential. In this way, one can explore several regimes: a regime of essentially harmonic phonons, which can mediate anisotropic spin–spin interactions between internal degrees of freedom of the ions [122]; a regime of weakly interacting phonons, which, in the case of a two-dimensional triangular-lattice Wigner crystal, condense in a non-trivial finite-momentum state containing vortex-antivortex pairs; and a regime of essentially hard-core phonons, which allows a mapping of the phononic Hamiltonian onto a frustrated $S = 1/2$ XY model with spatially anisotropic couplings that can be tuned by changing the orientation of the optical lattice with respect to the ionic crystal. In this latter case, it has been shown that an extremely rich physical picture can be obtained in the case of a half-filled system of phonons: in particular, one can realize a gapless spin-liquid phase with long-range chiral order in zig-zag ion ladders, and a

variety of two-dimensional spin-liquid phases, either gapped or gapless, in the case of a triangular Wigner crystal. Hence this setup offers a platform for the exploration of highly non-trivial quantum phases and quantum critical phenomena in tunable frustrated quantum magnets.

Part IV

Appendices

Appendix A

Code Examples

As a last part, we would like to give an idea of how to program the variational methods explained in part II. We present two MATLAB functions, one for the calculation of ground- and first excited states and one for the reduction of the virtual dimension of matrix product states. We demonstrate these functions by calculating the ground state and the first excited state of the antiferromagnetic Heisenberg chain and simulating a time–evolution with respect to this model. Furthermore, we use these functions to calculate the partition function of the 2–D Ising Model and evaluate the scalar product of two PEPS.

A.1 Minimization of the Energy

The function `minimizeE` optimizes the parameters of a matrix product state in such a way that the expectation value with respect to a given Hamiltonian tends to a minimum. The function expects this Hamiltonian to be defined in a $M \times N$ cell `hset`, where N denotes the number of sites and M the number of terms in the Hamiltonian. Assuming the Hamiltonian is of the form

$$H = \sum_{m=1}^{M} h_m^{(1)} \otimes \cdots \otimes h_m^{(N)},$$

the element `hset{m,j}` equals $h_m^{(j)}$. Further arguments are the virtual dimension of the resulting matrix product state, `D`, and the expected accuracy of the energy, `precision`.

Output arguments are the optimized energy `E` and corresponding matrix product state `mps`. The matrix product state is stored as a $1 \times N$ cell, each entry corresponding to one matrix.

Optionally, a matrix product state `mpsB` can be specified as an argument to which the resulting state shall be orthogonal. This is especially useful for calculating the first excited state.

```
function [E,mps]=minimizeE(hset,D,precision,mpsB)

[M,N]=size(hset);
d=size(hset{1,1},1);
mps=createrandommps(N,D,d);
mps=prepare(mps);

% storage-initialization
Hstorage=initHstorage(mps,hset,d);
if ~isempty(mpsB), Cstorage=initCstorage(mps,[],mpsB,N); end
P=[];

% optimization sweeps
while 1
    Evalues=[];

    % *************** cycle 1: j -> j+1 (from 1 to N-1) *************
    for j=1:(N-1)
        % projector-calculation
        if ~isempty(mpsB)
            B=mpsB{j};
            Cleft=Cstorage{j};
            Cright=Cstorage{j+1};
            P=calcprojector_onesite(B,Cleft,Cright);
        end

        % optimization
        Hleft=Hstorage(:,j);
        Hright=Hstorage(:,j+1);
        hsetj=hset(:,j);
        [A,E]=minimizeE_onesite(hsetj,Hleft,Hright,P);
        [A,U]=prepare_onesite(A,'lr');
        mps{j}=A;
        Evalues=[Evalues,E];

        % storage-update
        for m=1:M
            h=reshape(hset{m,j},[1,1,d,d]);
            Hstorage{m,j+1}=updateCleft(Hleft{m},A,h,A);
        end
```

```
            if ~isempty(mpsB)
                Cstorage{j+1}=updateCleft(Cleft,A,[],B);
            end
        end

        % *************** cycle 2: j -> j-1 (from N to 2) ***************
        for j=N:(-1):2
            % projector-calculation
            if ~isempty(mpsB)
                B=mpsB{j};
                Cleft=Cstorage{j};
                Cright=Cstorage{j+1};
                P=calcprojector_onesite(B,Cleft,Cright);
            end

            % minimization
            Hleft=Hstorage(:,j);
            Hright=Hstorage(:,j+1);
            hsetj=hset(:,j);
            [A,E]=minimizeE_onesite(hsetj,Hleft,Hright,P);
            [A,U]=prepare_onesite(A,'rl');
            mps{j}=A;
            Evalues=[Evalues,E];

            % storage-update
            for m=1:M
                h=reshape(hset{m,j},[1,1,d,d]);
                Hstorage{m,j}=updateCright(Hright{m},A,h,A);
            end
            if ~isempty(mpsB)
                Cstorage{j}=updateCright(Cright,A,[],B);
            end
        end

        if (std(Evalues)/abs(mean(Evalues))<precision)
            mps{1}=contracttensors(mps{1},3,2,U,2,1);
            mps{1}=permute(mps{1},[1,3,2]);
            break;
        end
    end
end
```

```
% ******************* one-site optimization ********************

function [A,E]=minimizeE_onesite(hsetj,Hleft,Hright,P)

DAl=size(Hleft{1},1);
DAr=size(Hright{1},1);
d=size(hsetj{1},1);

% calculation of Heff
M=size(hsetj,1);

Heff=0;
for m=1:M
    Heffm=contracttensors(Hleft{m},3,2,Hright{m},3,2);
    Heffm=contracttensors(Heffm,5,5,hsetj{m},3,3);
    Heffm=permute(Heffm,[1,3,5,2,4,6]);
    Heffm=reshape(Heffm,[DAl*DAr*d,DAl*DAr*d]);
    Heff=Heff+Heffm;
end

% projection on orthogonal subspace
if ~isempty(P), Heff=P'*Heff*P; end

% optimization
options.disp=0;
[A,E]=eigs(Heff,1,'sr',options);
if ~isempty(P), A=P*A; end
A=reshape(A,[DAl,DAr,d]);


function [P]=calcprojector_onesite(B,Cleft,Cright)

y=contracttensors(Cleft,3,3,B,3,1);
y=contracttensors(y,4,[2,3],Cright,3,[2,3]);
y=permute(y,[1,3,2]);
y=reshape(y,[prod(size(y)),1]);

Q=orth([y,eye(size(y,1))]);
P=Q(:,2:end);
```

A.2   Time Evolution

The function `reduceD` forms the basis for the simulation of a time evolution. It multiplies a given matrix product state with a given matrix product operator and reduces the virtual dimension of the resuling state, i.e. it searches a matrix product state with reduced virtual dimension and minimal distance to the original state. The matrix product state and the matrix product operator are specified in the arguments `mpsA` and `mpoX`. As before, they are represented by a cell with entries identifying the matrices. The reduced virtual dimension is specified in the argument `DB`. The argument `precision` defines the convergence condition: if fluctutions in the distance are less than `precision`, the optimization is assumed to be finished.

The output argument is the optimized matrix product state `mpsB` with virtual dimension `DB`.

```
function mpsB=reduceD(mpsA,mpoX,DB,precision)

N=length(mpsA);
dB=size(mpoX{1},3);
mpsB=createrandommps(N,DB,dB);
mpsB=prepare(mpsB);
% initialization of the storage
Cstorage=initCstorage(mpsB,mpoX,mpsA,N);

% optimization sweeps
while 1
    Kvalues=[];

    % *************** cycle 1: j -> j+1 (from 1 to N-1) *************
    for j=1:(N-1)
        % optimization
        Cleft=Cstorage{j};
        Cright=Cstorage{j+1};
        A=mpsA{j}; X=mpoX{j};
        [B,K]=reduceD2_onesite(A,X,Cleft,Cright);
        [B,U]=prepare_onesite(B,'lr');
        mpsB{j}=B;
        Kvalues=[Kvalues,K];

        % storage-update
        Cstorage{j+1}=updateCleft(Cleft,B,X,A);
    end
```

```
    % *************** cycle 2: j -> j-1 (from N to 2) ***************
    for j=N:(-1):2
        % optimization
        Cleft=Cstorage{j};
        Cright=Cstorage{j+1};
        A=mpsA{j}; X=mpoX{j};
        [B,K]=reduceD2_onesite(A,X,Cleft,Cright);
        [B,U]=prepare_onesite(B,'rl');
        mpsB{j}=B;
        Kvalues=[Kvalues,K];

        % storage-update
        Cstorage{j}=updateCright(Cright,B,X,A);
    end

    if std(Kvalues)/abs(mean(Kvalues))<precision
        mpsB{1}=contracttensors(mpsB{1},3,2,U,2,1);
        mpsB{1}=permute(mpsB{1},[1,3,2]);
        break;
    end
end


% ********************* one-site optimization **********************

function [B,K]=reduceD2_onesite(A,X,Cleft,Cright)

Cleft=contracttensors(Cleft,3,3,A,3,1);
Cleft=contracttensors(Cleft,4,[2,4],X,4,[1,4]);

B=contracttensors(Cleft,4,[3,2],Cright,3,[2,3]);
B=permute(B,[1,3,2]);

b=reshape(B,[prod(size(B)),1]);
K=-b'*b;
```

A.3   Auxiliary Methods

The previous two functions depend on several auxiliary functions that are printed in this section.

- Gauge transformation that prepares the MPS `mpsB` in such a form that *Neff* is equal to the identity for the first spin (see [157]):

```
function [mps]=prepare(mps)

N=length(mps);

for i=N:-1:2
    [mps{i},U]=prepare_onesite(mps{i},'rl');
    mps{i-1}=contracttensors(mps{i-1},3,2,U,2,1);
    mps{i-1}=permute(mps{i-1},[1,3,2]);
end


function [B,U,DB]=prepare_onesite(A,direction)

[D1,D2,d]=size(A);
switch direction
    case 'lr'
        A=permute(A,[3,1,2]); A=reshape(A,[d*D1,D2]);
        [B,S,U]=svd2(A); DB=size(S,1);
        B=reshape(B,[d,D1,DB]); B=permute(B,[2,3,1]);
        U=S*U;
    case 'rl'
        A=permute(A,[1,3,2]); A=reshape(A,[D1,d*D2]);
        [U,S,B]=svd2(A); DB=size(S,1);
        B=reshape(B,[DB,d,D2]); B=permute(B,[1,3,2]);
        U=U*S;
end
```

- Initialization of storages:

```
function [Hstorage]=initHstorage(mps,hset,d)

[M,N]=size(hset);
Hstorage=cell(M,N+1);
for m=1:M, Hstorage{m,1}=1; Hstorage{m,N+1}=1; end
for j=N:-1:2
```

```
        for m=1:M
            h=reshape(hset{m,j},[1,1,d,d]);
            Hstorage{m,j}=updateCright(Hstorage{m,j+1},mps{j},h,mps{j});
        end
    end
```

```
function [Cstorage]=initCstorage(mpsB,mpoX,mpsA,N)
```

```
Cstorage=cell(1,N+1);
Cstorage{1}=1;
Cstorage{N+1}=1;
for i=N:-1:2
    if isempty(mpoX), X=[]; else X=mpoX{i}; end
    Cstorage{i}=updateCright(Cstorage{i+1},mpsB{i},X,mpsA{i});
end
```

```
function [Cleft]=updateCleft(Cleft,B,X,A)
```

```
if isempty(X), X=reshape(eye(size(B,3)),[1,1,2,2]); end
```

```
Cleft=contracttensors(A,3,1,Cleft,3,3);
Cleft=contracttensors(X,4,[1,4],Cleft,4,[4,2]);
Cleft=contracttensors(conj(B),3,[1,3],Cleft,4,[4,2]);
```

```
function [Cright]=updateCright(Cright,B,X,A)
```

```
if isempty(X), X=reshape(eye(size(B,3)),[1,1,2,2]); end
```

```
Cright=contracttensors(A,3,2,Cright,3,3);
Cright=contracttensors(X,4,[2,4],Cright,4,[4,2]);
Cright=contracttensors(conj(B),3,[2,3],Cright,4,[4,2]);
```

- Creation of a random MPS:

```
function [mps]=createrandommps(N,D,d)
```

```
mps=cell(1,N);
mps{1}=randn(1,D,d)/sqrt(D);
mps{N}=randn(D,1,d)/sqrt(D);
for i=2:(N-1)
```

```
        mps{i}=randn(D,D,d)/sqrt(D);
    end
```

- Scalar product of the MPS `mpsl` with the MPS `mpsr`:

```
function [s]=scalarproduct(mpsl,mpsr)

N=length(mpsl);
d=size(mpsl{1},3);

s=1;
X=eye(d); X=reshape(X,[1,1,d,d]);
for j=N:-1:1
    s=updateCright(s,mpsl{j},X,mpsr{j});
end
```

- Expectation value of the MPS `mps` with respect to the operator defined in `hset`:

```
function [e,n]=expectationvalue(mps,hset)

[M,N]=size(hset);
d=size(mps{1},3);

% expectation value
e=0;
for m=1:M
    em=1;
    for j=N:-1:1
        h=hset{m,j};
        h=reshape(h,[1,1,d,d]);
        em=updateCright(em,mps{j},h,mps{j});
    end
    e=e+em;
end

% norm
n=1;
X=eye(d); X=reshape(X,[1,1,d,d]);
for j=N:-1:1
    n=updateCright(n,mps{j},X,mps{j});
end

e=e/n;
```

- Contraction of index `indX` of tensor `X` with index `indY` of tensor `Y` (`X` and `Y` have a number of indices corresponding to `numindX` and `numindY` respectively):

```
function [X,numindX]=contracttensors(X,numindX,indX,Y,numindY,indY)

Xsize=ones(1,numindX); Xsize(1:length(size(X)))=size(X);
Ysize=ones(1,numindY); Ysize(1:length(size(Y)))=size(Y);

indXl=1:numindX; indXl(indX)=[];
indYr=1:numindY; indYr(indY)=[];

sizeXl=Xsize(indXl);
sizeX=Xsize(indX);
sizeYr=Ysize(indYr);
sizeY=Ysize(indY);

if prod(sizeX)~=prod(sizeY)
    error('indX and indY are not of same dimension.');
end

if isempty(indYr)
    if isempty(indXl)
        X=permute(X,[indX]);
        X=reshape(X,[1,prod(sizeX)]);

        Y=permute(Y,[indY]);
        Y=reshape(Y,[prod(sizeY),1]);

        X=X*Y;
        Xsize=1;

        return;

    else
        X=permute(X,[indXl,indX]);
        X=reshape(X,[prod(sizeXl),prod(sizeX)]);

        Y=permute(Y,[indY]);
        Y=reshape(Y,[prod(sizeY),1]);

        X=X*Y;
        Xsize=Xsize(indXl);
```

```
            X=reshape(X,[Xsize,1]);

            return
        end
    end

    X=permute(X,[indXl,indX]);
    X=reshape(X,[prod(sizeXl),prod(sizeX)]);

    Y=permute(Y,[indY,indYr]);
    Y=reshape(Y,[prod(sizeY),prod(sizeYr)]);

    X=X*Y;
    Xsize=[Xsize(indXl),Ysize(indYr)];

    X=reshape(X,[Xsize,1]);
```

• Economical singular value decomposition:

```
function [U,S,V]=svd2(T)

[m,n]=size(T);
if m>=n, [U,S,V]=svd(T,0); else [V,S,U]=svd(T',0); end
V=V';
```

A.4   Examples

A.4.1   Ground State and First Excited State

As a demonstration of the function `minimizeE` from before, we show how to calculate the ground-state and the first excited state of the Heisenberg antiferromagnetic chain. We focus on a chain of length $N = 10$, and vary D from 2 to 18. The results of the variational calculation we compare to the results obtained via exact diagonalization. As can be gathered from figure A.1 (*left*), the error $|E - E_{exact}|/|E_{exact}|$ is of order 10^{-2} for $D = 2$ and decreases below 10^{-8} for $D = 18$.

The code to obtain these results looks as follows:

```
N=10;
precision=1e-5;
D=5;
% Heisenberg Hamiltonian
M=3*(N-1);
hset=cell(M,N);
sx=[0,1;1,0]; sy=[0,-1i;1i,0]; sz=[1,0;0,-1]; id=eye(2);
for m=1:M, for j=1:N, hset{m,j}=id; end; end
for j=1:(N-1)
    hset{3*(j-1)+1,j}=sx; hset{3*(j-1)+1,j+1}=sx;
    hset{3*(j-1)+2,j}=sy; hset{3*(j-1)+2,j+1}=sy;
    hset{3*(j-1)+3,j}=sz; hset{3*(j-1)+3,j+1}=sz;
end

% ground state energy
randn('state',0)
[E0,mps0]=minimizeE(hset,D,precision,[]);
fprintf('E0 = %g\n',E0);

% first excited state
[E1,mps1]=minimizeE(hset,D,precision,mps0);
fprintf('E1 = %g\n',E1);
```

A.4.2   Time Evolution

To demonstrate the function `reduceD`, we focus on the real time evolution with respect to the Hamiltonian of the Heisenberg antiferromagnetic chain. Starting state is a product state with all spins pointing in z-direction - except the one at the center which is flipped. We evolve the state with the method
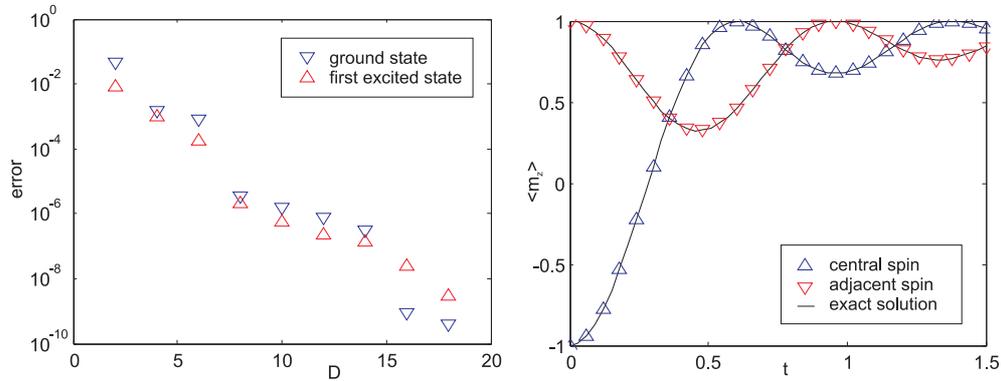
Figure A.1: *left:* Error $|E - E_{exact}|/|E_{exact}|$ of the energy of the ground state and the first excited state of the $N = 1$ Heisenberg antiferromagnetic chain, calculated using the variational method using MPS, as a function of the virtual dimension D. *right:* Time evolution of the magnetization of the central spin (and its neighbor) under the Hamiltonian of the $N = 10$ antiferromagnetic Heisenberg chain. The time evolution is calculated exactly and via reduction of dimension of MPS (D=5). Starting state is a product state with all spins pointing in z-direction - except the one at the center which is flipped.

`reduceD` and calculate at each step the magetization m_z of the central spin. The results for a $N = 10$ chain and $D = 5$ can be gathered from figure A.1 (*right*). This figure also contains the results of an exact calculation.

The code for this example is the following:

```
N=10;
dt=0.03;
D=5;
precision=1e-5;
jflipped=5;

% magnetization in z-direction
oset=cell(1,N);
sx=[0,1;1,0]; sy=[0,-1i;1i,0]; sz=[1,0;0,-1]; id=eye(2);
for j=1:N, oset{1,j}=id; end;
oset{1,jflipped}=sz;

% time evolution operator
h=kron(sx,sx)+kron(sy,sy)+kron(sz,sz);
w=expm(-1i*dt*h);
w=reshape(w,[2,2,2,2]); w=permute(w,[1,3,2,4]); w=reshape(w,[4,4]);
```

```
[U,S,V]=svd2(w); eta=size(S,1);
U=U*sqrt(S); V=sqrt(S)*V;
U=reshape(U,[2,2,eta]); U=permute(U,[4,3,2,1]);
V=reshape(V,[eta,2,2]); V=permute(V,[1,4,3,2]);
I=reshape(id,[1,1,2,2]);
mpo_even=cell(1,N);
mpo_odd=cell(1,N);
for j=1:N, mpo_even{j}=I; mpo_odd{j}=I; end
for j=1:2:(N-1), mpo_odd{j}=U; mpo_odd{j+1}=V; end
for j=2:2:(N-1), mpo_even{j}=U; mpo_even{j+1}=V; end

% starting state (one spin flipped)
mps0=cell(1,N);
for j=1:N
    if j==jflipped, state=[0; 1]; else state=[1; 0]; end
    mps0{j}=reshape(state,[1,1,2]);
end

% time evolution
mps=mps0;
mzvalues=[];
for step=1:50
    fprintf('Step %2d: ',step);
    [mps,K]=reduceD(mps,mpo_even,D,precision);
    [mps,K]=reduceD(mps,mpo_odd,D,precision);
    mz=expectationvalue(mps,oset);
    mzvalues=[mzvalues,mz];
    fprintf('mz=%g\n',mz);
end
```

A.4.3 Evaluation of Partition Functions

Another application of the function `reduceD` is the calculation of partition functions of 2–D classical and 1–D quantum systems, as discussed in chapter 2. In the following, we focus on the 2–D Ising model with open boundary conditions.

As a first step, we have to reexpress the partition function as a contraction of 4–index tensors X (see section 2.1). The calculation of these tensors is performed by the subroutine `createXising`. The parameters that are required are the coupling strengths (in all four directions) in units of $1/\beta$.

The code for this subroutine is as follows:
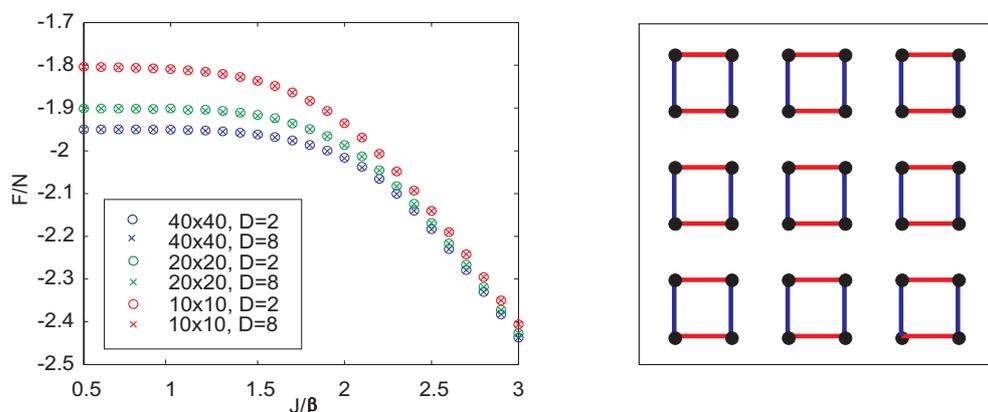
Figure A.2: *left:* Partition function of the 2–D Ising model as a function of J/β. Dots (crosses) denote results for $D = 2$ ($D = 8$). The different colors represent different lattice sizes (see legend). *right:* SRVB with horizontal (vertical) dimers represented by red (blue) lines.

```
function [X]=createXising(Jl,Jr,Ju,Jd)

[fl,gl]=calcfg(Jl);
[fr,gr]=calcfg(Jr);
[fu,gu]=calcfg(Ju);
[fd,gd]=calcfg(Jd);

X=zeros(2,2,2,2);
for l=1:2
    for r=1:2
        for u=1:2
            for d=1:2
                for n=1:2
                    X(l,r,u,d)=X(l,r,u,d)+gl(n,l)*fr(n,r)*gu(n,u)*fd(n,d);
                end
            end
        end
    end
end


function [f,g]=calcfg(J)

w=[exp(-J),exp(J); exp(J),exp(-J)];
[f,s,g]=svd2(w); f=f*sqrt(s); g=sqrt(s)*g; g=g.';
```

Now, since the tensor network has been defined, it can be contracted in an approximative way by reexpressing it as a time–evolution of a MPS. The time–evolution is performed, as before, by means of the subroutine reduceD.

The code for contracting the network looks as follows:

```
N=[20,20];
beta=1;
D=6;
precision=1e-5;

% define upper matrix product state
X=createXising(beta,beta,0,beta);
for j=2:(N(2)-1)
    mpsu{j}=permute(X(:,:,1,:),[1,2,4,3]);
end
X=createXising(0,beta,0,beta);
mpsu{1}=permute(X(1,:,1,:),[1,2,4,3]);
X=createXising(beta,0,0,beta);
mpsu{N(2)}=permute(X(:,1,1,:),[1,2,4,3]);

% define lower matrix product state
mpsd=mpsu;

% define matrix product operators
X=createXising(beta,beta,beta,beta);
for j=2:(N(2)-1)
    mpo{j}=X;
end
X=createXising(0,beta,beta,beta);
mpo{1}=X(1,:,:,:);
X=createXising(beta,0,beta,beta);
mpo{N(2)}=X(:,1,:,:);

% perform the contraction
mps=mpsu;
logfactor=0;
for i=2:(N(1)-1)
    % keep the mps normalized
    n=sqrt(scalarproduct(mps,mps));
    for j=1:N(2), mps{j}=mps{j}/(n^(1/N(2))); end
    logfactor=logfactor+log(n);
```

```
    % time evolution step
    [mps,K]=reduceD(mps,mpo,D,precision);
end
Z=scalarproduct(mpsd,mps);

% the result: the free energy
F=-1/beta*(log(Z)+logfactor);
```

Results for a several lattice–sizes and virtual dimensions D of the MPS can be gathered from figure A.2 (*left*). Here, the free energy is plotted as a function of J/β. It can be seen that convergence is achieved quickly with increasing D. Note that these results differ slightly from the results obtained in section 3.1 for periodic boundary conditions.

A.4.4 Scalar Product of two PEPS

As a last example, we show how the function `reduceD` can be used to efficiently calculate the scalar product of two PEPS. The method we use is the one explained in chapter 4: we rewrite the scalar product as a contraction of a tensor network and perform this contraction by reexpressing it as a time–evolution of a MPS.

We choose two short range valence bond states (SRVB), since these states have an exact representation as PEPS and their scalar product can be evaluated exactly [88]. In particular, we assume that the first SRVB is made up of horizontal dimers and the second SRVB of vertical dimers (see right part of figure A.2).

The code for performing this scalar product is as follows:

```
N=[10,10]; % must be even
D=2;
precision=1e-5;

id=eye(2); sy=[0,-1i;1i,0];
f=id/2^(1/4); g=(-1i*sy)/2^(1/4);

% PEPS1: SRVB with horizontal dimers
peps1=cell(N);
for i=1:N(1)
    for j=1:2:(N(2)-1)
        peps1{i,j}=permute(f,[3,2,4,5,1]);
        peps1{i,j+1}=permute(g,[2,3,4,5,1]);
    end
end
```

```
% PEPS2: SRVB with vertical dimers
peps2=cell(N);
for i=1:2:(N(1)-1)
    for j=1:N(2)
        peps2{i,j}=permute(f,[3,4,5,2,1]);
        peps2{i+1,j}=permute(g,[3,4,2,5,1]);
    end
end

% Tensor network
X=cell(N);
for i=1:N(1)
    for j=1:N(2)
        A=peps1{i,j};
        B=peps2{i,j};
        C=contracttensors(A,5,5,conj(B),5,5);
        C=permute(C,[1,5,2,6,3,7,4,8]);
        C=reshape(C,[size(A,1)*size(B,1),size(A,2)*size(B,2),...
            size(A,3)*size(B,3),size(A,4)*size(B,4)]);
        X{i,j}=C;
    end
end

% upper matrix product state
mpsu=cell(1,N(2));
for j=1:N(2)
    mpsu{j}=permute(X{1,j},[1,2,4,3]);
end

% lower matrix product state
mpsd=cell(1,N(2));
for j=1:N(2)
    mpsd{j}=X{N(1),j};
end

% contraction
mps=mpsd;
logfactor=0;
for i=(N(1)-1):-1:2
    % keep the mps normalized
    n=sqrt(scalarproduct(mps,mps));
    for j=1:N(2), mps{j}=mps{j}/(n^(1/N(2))); end
```

```
    logfactor=logfactor+log(n);

    % time evolution step
    [mps,K]=reduceD(mps,X(i,:),D,precision);
end

% the result
s=exp(logfactor)*scalarproduct(mps,mpsu);

% the error
sexact=2^(prod(N)/4-prod(N)/2);
serr=(s-sexact)/sexact;
```

The precision of the results is very high, already for $D = 2$. For a 10×10 lattice, the relative error is of order 10^{-14}. We note that the way we calculate the scalar product here is not the most efficient one. For maximal efficiency, the order in which all tensor are contracted has to be optimized, as described in chapter 4.

Bibliography

[1] M. G. abd C. Regal and D. S. Jin. Emergence of a molecular bose-einstein condensate from a fermi gas. *Nature*, 426:537, 2003.

[2] I. Affleck, T. Kennedy, E. H. Lieb, and H. Tasaki. *Commun. Math. Phys.*, 115:477, 1988.

[3] S. Anders, M. B. Plenio, W. Dür, F. Verstraete, and H. J. Briegel. Ground-state approximation for strongly interacting spin systems in arbitrary spatial dimension. *Phys. Rev. Lett.*, 97:107206, 2006.

[4] P. W. Anderson. The resonating valence bond state in La2CuO4 and superconductivity. *Science*, 235:1196, 1987.

[5] F. Barahona. On the computational complexity of Ising spin-glass models. *J. Phys. A*, 15:3241, 1982.

[6] G. Birkl, S. Kassner, and H. Walther. Multiple-shell structures of laser-cooled Mg–ions in a quadrupole storage ring. *Nature*, 357:310, 1992.

[7] I. Bloch, J. Dalibard, and W. Zwerger. Many-body physics with ultra-cold gases. *arXiv:0704.3011v2 [cond-mat.other]*, 2007.

[8] L. Bombelli, R. K. Koul, J. H. Lee, and R. D. Sorkin. Quantum source of entropy for black holes. *Phys. Rev. D*, 34:373, 1986.

[9] M. Born and V. Fock. Beweis des Adiabatensatzes. *Z. Phys.*, 51:165–180, 1928.

[10] H. J. Briegel, T. Calarco, D. Jaksch, J. I. Cirac, and P. Zoller. Quantum computing with neutral atoms. *Journal of Modern Optics*, 47:415, 2000.

[11] C. Bruder, R. Fazio, and G. Schön. The Bose-Hubbard model: from Josephson junction arrays to optical lattices. *Ann. Phys.*, 14:566, 2005.

[12] H. P. Büchler, G. Blatter, and W. Zwerger. Commensurate-Incommensurate Transition of Cold Atoms in an Optical Lattice. *Phys. Rev. Lett.*, 90:130401, 2003.

[13] R. J. Bursill, T. Xiang, and G. A. Gehring. *J. Phys. Conden. Matter*, 8:L583, 1996.

[14] P. Calabrese and J. Cardy. Entanglement entropy and quantum field theory. *J. Stat. Mech.*, 0406:P002, 2004.

[15] C. Callan and F. Wilczek. On geometric entropy. *Phys. Rev. B*, 333:55, 1994.

[16] L. Capriotti and S. Sachdev. Low-temperature broken-symmetry phases of spiral antiferromagnets. *Phys. Rev. Lett.*, 93:257206, 2004.

[17] L. Capriotti, D. J. Scalapino, and S. R. White. Spin–liquid versus dimerized ground states in a frustrated heisenberg antiferromagnet. *Phys. Rev. Lett.*, 93:177004, 2004.

[18] M. A. Cazalilla. Bosonizing one-dimensional cold atomic gases. *Journal of Physics B: AMOP*, 37:S1–S47, 2004.

[19] D. M. Ceperley. Path integrals in the theory of condensed helium. *Rev. Mod. Phys.*, 67:279, 1995.

[20] P. Chandra, P. Coleman, and A. I. Larkin. Ising transition in frustrated Heisenberg models. *Phys. Rev. Lett.*, 64:88, 1990.

[21] P. Chandra and B. Doucot. Possible spin-liquid state at large S for the frustrated square Heisenberg lattice. *Phys. Rev. B*, 38:9335, 1988.

[22] J. Chiaverini and W. E. Lybarger. Laserless trapped-ion quantum simulations without spontaneous scattering using microtrap arrays. *arXiv:0711.0233v1 [quant-ph]*, 2007.

[23] A. M. Childs, E. Farhi, and J. Preskill. Robustness of adiabatic quantum computation. *Phys. Rev. A*, 65:012322, 2001.

[24] A. Chubukov. First-order transition in frustrated quantum antiferromagnets. *Phys. Rev. B*, 44:392, 1991.

[25] J. I. Cirac and P. Zoller. Quantum computations with cold trapped ions. *Phys. Rev. Lett.*, 74:4091, 1995.

[26] J. I. Cirac and P. Zoller. A scalable quantum computer with ions in an array of microtraps. *Nature*, 404:579–581, 2000.

[27] V. Coffman, J. Kundu, and W. K. Wootters. Distributed entanglement. *Phys. Rev. A*, 61:052306, 2000.

[28] R. Coldea, D. A. Tennant, A. M. Tsvelik, and Z. Tylczynski. Experimental realization of a 2D fractional quantum spin liquid. *Phys. Rev. Lett.*, 86:1335, 2001.

[29] A. J. Daley, C. Kollath, U. Schollwoeck, and G. Vidal. Time-dependent density-matrix renormalization-group using adaptive effective Hilbert spaces. *J. Stat. Mech.:*, Theor. Exp.:P04005, 2004.

[30] X. L. Deng, D. Porras, and J. I. Cirac. Effective spin quantum phases in systems of trapped ions. *Phys. Rev. A*, 72:063407, 2005.

[31] X. L. Deng, D. Porras, and J. I. Cirac. Quantum phases of interacting phonons in ion traps. *arXiv:quant-ph/0703178v1*, 2007.

[32] P. Dirac. *Proc. Roy. Soc. London*, 112A:661, 1926.

[33] M. S. L. du Croo de Jongh, J. M. J. van Leeuwen, and W. van Saarloos. Incorporation of density-matrix wave functions in Monte Carlo simulations: Application to the frustrated Heisenberg model. *Phys. Rev. B*, 62:14844, 2000.

[34] V. Dunjko, V. Lorent, and M. Olshanii. Bosons in cigar-shaped traps: Thomas-Fermi regime, Tonks-Girardeau regime, and in between. *Phys. Rev. Lett.*, 86:5413, 2001.

[35] K. B. Efetov and A. I. Larkin. Correlation functions in one-dimensional systems with strong interactions. *Sov. Phys. JETP*, 42:390, 1975.

[36] M. Fannes, B. Nachtergaele, and R. F. Werner. *Comm. Math. Phys.*, 144:443, 1992.

[37] E. Farhi, J. Goldstone, S. Gutmann, J. Lapan, A. Lundgren, and D. Preda. A Quantum Adiabatic Evolution Algorithm Applied to Random Instances of an NP–Complete Problem. *Science*, 292:472, 2001.

[38] E. Farhi, J. Goldstone, S. Gutmann, and M. Sipser. Quantum computation by adiabatic evolution. *arXiv:quant-ph/0001106v1*, 2000.

[39] J. Ferrer. Spin-liquid phase for the frustrated quantum heisenberg antiferromagnet on a square lattice. *Phys. Rev. B*, 47:8769, 1993.

[40] R. P. Feynman. Simulating Physics with Computers. *Int. J. Theor. Phys.*, 21:467, 1982.

[41] F. Figueirido, A. Karlhede, S. Kivelson, S. Sondhi, M. Rocek, and D. S. Rokhsar. Exact diagonalization of finite frustrated spin-1/2 Heisenberg models. *Phys. Rev. B*, 41:4619, 1989.

[42] M. P. Fisher, P. B. Weichmann, G. Grinstein, and D. S. Fisher. Boson localization and the superfluid-insulator transition. *Phys. Rev. B*, 40:546, 1989.

[43] S. Fölling, S. Trotzky, P. Cheinet, M. Feld, R. Saers, A. Widera, T. Müller, and I. Bloch. Direct observation of second-order atom tunnelling. *Nature*, 448:1029, 2007.

[44] J. B. Fouet, M. Mambrini, P. Sindzingre, and C. Lhuillier. Planar pyrochlore: A valence-bond crystal. *Phys. Rev. B*, 67:054411, 2003.

[45] E. H. L. u. B. S. Freeman J. Dyson. Phase transitions in quantum spin systems with isotropic and nonisotropic interactions. *J. Stat. Phys.*, 18:335, 1978.

[46] K. Friedrichs. On the Adiabatic Theorem in Quantum Theory. *Report IMM NYU-218*, 1955.

[47] J. J. García-Ripoll. Time evolution algorithms for matrix product states and DMRG. *New J. Phys.*, 8:305, 2006.

[48] M. P. Gelfand, R. R. Singh, and D. A. Huse. Zero-temperature ordering in two-dimensional frustrated quantum Heisenberg antiferromagnets. *Phys. Rev. B*, 40:10801, 1989.

[49] G.Hooft. On the quantum structure of a black hole. *Nucl. Phys. B*, 256:727, 1985.

[50] D. Gioev and I. Klich. Entanglement entropy of fermions in any dimension and the widom conjecture. *Phys. Rev. Lett.*, 96:100503, 2006.

[51] M. Girardeau. Relationship between systems of impenetrable bosons and fermions in one dimension. *J. Math. Phys.*, 1:516, 1960.

[52] A. Görlitz, J. M. Vogels, A. E. Leanhardt, C. Raman, T. L. Gustavson, J. R. Abo-Shaeer, A. P. Chikkatur, S. Gupta, S. Inouye, T. Rosenband, and W. Ketterle. Realization of bose-einstein condensates in lower dimensions. *Phys. Rev. Lett.*, 87:130402, 2001.

[53] M. Greiner, I. Bloch, O. Mandel, T. W. Hänsch, and T. Esslinger. Exploring phase coherence in a 2D lattice of Bose-Einstein condensates. *Phys. Rev. Lett.*, 87:160405, 2001.

[54] M. Greiner, O. Mandel, T. Esslinger, T. W. Hänsch, and I. Bloch. Quantum phase transition from a superfluid to a Mott insulator in a gas of utracold atoms. *Nature*, 415:39, 2002.

[55] S. Gulde, M. Riebe, G. P. T. Lancaster, C. Becher, J. Eschner, H. Häffner, F. Schmidt-Kaler, I. L. Chuang, and R. Blatt. Implementation of the Deutsch-Jozsa algorithm on an ion-trap quantum computer. *Nature*, 421:48, 2003.

[56] F. D. Haldane. Continuum dynamics of the 1-d heisenberg antiferromagnet: Identification with the O(3) nonlinear sigma model. *Phys. Lett. A*, 93:464, 1983.

[57] F. D. Haldane. Nonlinear field theory of large-spin Heisenberg antiferromagnets: Semiclassically quantized solitons of the one-dimensional easy-axis Néel state. *Phys. Rev. Lett.*, 50:1153, 1983.

[58] I. Harada. One-dimensional classical planar model with competing interactions. *J. Phys. Soc. Jpn.*, 53:1643, 1984.

[59] M. B. Hastings. Solving gapped hamiltonians locally. *Phys. Rev. B*, 73:085115, 2006.

[60] M. B. Hastings. Entropy and entanglement in quantum ground states. *arXiv:cond-mat/0701055v1*, 2007.

[61] W. Heisenberg. *Z. Phys.*, 38:441, 1926.

[62] Y. Hieida, K. Okunishi, and Y. Akutsu. *New J. Phys.*, 1:7, 1999.

[63] T. Hikihara, M. Kaburagi, and H. Kawamura. Ground-state phase diagrams of frustrated spin-S XXZ chains: Chiral ordered phases. *Phys. Rev. B*, 63:174430, 2001.

[64] A. Isacsson and O. F. Syljuasen. Variational treatment of the Shastry-Sutherland antiferromagnet using Projected Entangled Pair States (PEPS). *Phys. Rev. E*, 74:026701, 2006.

[65] D. Jaksch, H. J. Briegel, J. I. Cirac, C. W. Gardiner, and P. Zoller. Entanglement of atoms via cold controlled collisions. *Phys. Rev. Lett*, 82:1975, 1999.

[66] D. Jaksch, C. Bruder, J. I. Cirac, C. W. Gardiner, and P. Zoller. Cold bosonic atoms in optical lattices. *Phys. Rev. Lett*, 81:3108, 1998.

[67] S. Jochim, M. Bartenstein, A. Altmeyer, G. Hendl, S. Riedl, C. Chin, J. H. Denschlag, and R. Grimm. Bose-einstein condensation of molecules. *Science*, 302:2101, 2003.

[68] R. Jozsa and N. Linden. On the role of entanglement in quantum computational speed-up. *arXiv:quant-ph/0201143v2*, 2002.

[69] T. Kato. *J. Phys. Soc. Jap.*, 5:435, 1950.

[70] B. Kaufman. Crystal statistics. II. Partition function evaluated by spinor analysis. *Phys. Rev.*, 76:1232, 1949.

[71] H. Kawamura. Classical and quantum chiral order in frustrated XY magnets. *arXiv:cond-mat/0202109v1*, 2002.

[72] T. Kennedy, E. H. Lieb, and B. S. Shastry. The XY model has long-range order for all spins and all dimensions greater than 1. *Phys. Rev. Lett.*, 61:2582, 1988.

[73] D. Kielpinski, C. Monroe, and D. J. Wineland. Architecture for a large-scale ion-trap quantum computer. *Nature*, 417:709, 2002.

[74] A. Kitaev. *Annals of Phys.*, 303:2, 2003.

[75] M. Köhl, T. Stöferle, H. Moritz, C. Schori, and T. Esslinger. 1D Bose gases in an optical lattice. *Appl. Phys. B*, 79:1009, 2004.

[76] C. Kollath, U. Schollwöck, J. von Delft, and W. Zwerger. Spatial correlations of trapped one-dimensional bosons in an optical lattice. *Phys. Rev. A*, 69:031601, 2004.

[77] V. E. Korepin, N. M. Bogoliubov, and A. G. Izergin. *Quantum Inverse Scattering Method and Correlation Functions*. Cambridge University Press, 1993.

[78] D. Leibfried, R. Blatt, C. Monroe, and D. Wineland. Quantum dynamics of single trapped ions. *Rev. Mod. Phys.*, 75:281, 2003.

[79] D. Leibfried, B. DeMarco, V. Meyer, D. Lucas, M. Barrett, J. Britton, W. M. Itano, B. Jelenkovic, C. Langer, T. Rosenband, and D. J. Wineland. Experimental demonstration of a robust, high-fidelity geometric two ion-qubit phase gate. *Nature*, 422:412, 2003.

[80] A. Lenard. Momentum distribution in the ground state of the one-dimensional system of impenetrable bosons. *J. Math. Phys.*, 5:930, 1964.

[81] P. W. Leung and N. Lam. Numerical evidence for the spin-peierls state in the frustrated quantum antiferromagnet. *Phys. Rev. B*, 53:2213, 1996.

[82] M. Levin and X. G. Wen. Detecting topological order in a ground state wave function. *Phys. Rev. Lett.*, 96:110405, 2006.

[83] M. Lewenstein, A. Sanpera, V. Ahufinger, B. Damski, A. Sen, and U. Sen. Ultracold atomic gases in optical lattices: mimicking condensed matter physics and beyond. *Adv. Phys.*, 56:243, 2007.

[84] E. Lieb, T. Schultz, and D. Mattis. Two Soluble Models of an Antiferromagnetic Chain. *Annals of Physics*, 16:407–466, 1961.

[85] E. H. Lieb and W. Liniger. Exact analysis of an interacting bose gas. I. The general solution and the ground state. *Phys. Rev.*, 130:1605, 1963.

[86] S. Lloyd. Universal Quantum Simulators. *Science*, 273:1073, 1996.

[87] P. Locher. Linear spin waves in a frustrated heisenberg model. *Phys. Rev. B*, 41:2537, 1990.

[88] M. Mambrini, A. Läuchli, D. Poilblanc, and F. Mila. Plaquette valence–bond crystal in the frustrated Heisenberg quantum antiferromagnet on the square lattice. *Phys. Rev. B*, 74:144422, 2006.

[89] M. Mambrini and F. Mila. RVB description of the low–energy singlets of the spin 1/2 Kagomé antiferromagnet. *Eur. Phys. J. B*, 17:651, 2000.

[90] O. Mandel, M. Greiner, A. Widera, T. Rom, T. W. Hänsch, and I. Bloch. Controlled collisions for multi-particle entanglement of optically trapped atoms. *Nature*, 425:937, 2003.

[91] M. A. Martin-Delgado, M. Roncaglia, and G. Sierra. *Phys. Rev. B*, 64:075117, 2001.

[92] D. C. Mattis. Ground-state symmetry in XY model of magnetism. *Phys. Rev. Lett.*, 42:1503, 1979.

[93] A. Micheli, G. K. Brennen, and P. Zoller. A toolbox for lattice-spinmodels with polar molecules. *Nature Physics*, 2:341, 2006.

[94] F. Mintert and C. Wunderlich. Ion-trap quantum logic using long-wavelength radiation. *Phys. Rev. Lett.*, 87:257904, 2001.

[95] T. B. Mitchell, J. J. Bollinger, D. H. E. Dubin, X.-P. Huang, W. M. Itano, and R. H. Baughman. Direct observations of structural phase transitions in planar crystallized ion plasmas. *Science*, 282:1290, 1998.

[96] C. Monroe, D. M. Meekhof, B. E. King, W. M. Itano, and D. J. Wineland. Demonstration of a fundamental quantum logic gate. *Phys. Rev. Lett.*, 75:4714, 1995.

[97] A. Moreo, E. Dagotto, T. Jolicoeur, and J. Riera. Incommensurate correlations in the t-J and frustrated spin-1/2 Heisenberg models. *Phys. Rev. B*, 42:6283, 1990.

[98] H. Moritz, T. Stöferle, M. Köhl, and T. Esslinger. Exciting collective oscillations in a trapped 1D gas. *Phys. Rev. Lett.*, 91:250402, 2003.

[99] V. Murg and J. I. Cirac. Adiabatic time evolution in spin-systems. *Phys. Rev. A*, 69:042320, 2004.

[100] V. Murg, F. Verstraete, and J. I. Cirac. Efficient evaluation of partition functions of frustrated and inhomogeneous spin systems. *Phys. Rev. Lett.*, 95:057206, 2005.

[101] V. Murg, F. Verstraete, and J. I. Cirac. Variational study of hard-core bosons in a two-dimensional optical lattice using projected entangled pair states. *Phys. Rev. A*, 75:033605, 2007.

[102] V. Murg, F. Verstraete, and J. I. Cirac. Exploring frustrated spin-systems using projected entangled pair states (PEPS). *in preparation*, 2008.

[103] M. A. Nielsen and I. L. Chuang. *Quantum Computation and Quantum Information.* Cambridge University Press, 2000.

[104] H. Niggeman, A. Klümper, and J. Zittartz. *Z. Phys. B*, 104:103, 1997.

[105] T. Nishino. Density Matrix Renormatlization Group Method for 2D Classical Models. *J. Phys. Soc. Jpn.*, 64:3598, 1995.

[106] T. Nishino, K. Okunishi, Y. Hieida, N. Maeshima, and Y. Akutsu. Self-consistent tensor product variational approximation for 3D classical models. *Nucl. Phys. B*, 575:504, 2004.

[107] Y. Nishio, N. Maeshima, A. Gendiar, and T. Nishino. Tensor product variational formulation for quantum systems. *arXiv:cond-mat/0401115v1*, 2004.

[108] K. Okunishi and T. Nishino. *Prog. Theor. Phys.*, 103:541, 2000.

[109] M. Olshanii. Atomic scattering in the presence of an external confinement. *Phys. Rev. Lett.*, 81:938, 1998.

[110] M. Olshanii and V. Dunjko. Short-distance correlation properties of the Lieb-Liniger system and momentum distributions of trapped one-dimensional atomic gases. *Phys. Rev. Lett.*, 91:090401, 2003.

[111] I. P. Omelyan, I. M. Mryglod, and R. Folk. Optimized Forest-Ruth- and Suzuki-like algorithms for integration of motion in many-body systems. *Computer Physics Communications*, 146:188, 2002.

[112] L. Onsager. Crystal statistics. I. A two-dimensional model with an order-disorder transition. *Phys. Rev.*, 65:117, 1944.

[113] Y. B. Ovchinnikov, J. H. Müller, M. R. Doery, E. J. D. Vredenbregt, K. Helmerson, S. L. Rolston, and W. D. Phillips. Diffraction of a released bose-einstein condensate by a pulsed standing light wave. *Phys. Rev. Lett.*, 83:284, 1999.

[114] B. Paredes, F. Verstraete, and J. I. Cirac. Exploiting quantum parallelism to simulate quantum random many-body systems. *Phys. Rev. Lett.*, 95:140501, 2005.

[115] B. Paredes, A. Widera, V. Murg, O. Mandel, S. Fölling, I. Cirac, G. V. Shlyapnikov, T. W. Hänsch, and I. Bloch. Tonks-girardeau gas of ultracold atoms in an optical lattice. *Nature*, 429:277, 2004.

[116] C. E. Pearson, D. R. Leibrandt, W. S. Bakr, W. J. Mallard, K. R. Brown, , and I. L. Chuang. Experimental investigation of planar ion traps. *Phys. Rev. A*, 73:032307, 2006.

[117] I. Peschel, X. Wang, M. Kaulke, and K. Hallberg. *Density-Matrix Renormalization*. Springer-Verlag, 1998.

[118] C. J. Pethick and H. Smith. *Bose–Einstein Condensation in Dilute Gases*. Cambridge University Press, 2002.

[119] D. S. Petrov, G. V. Shlyapnikov, and J. T. M. Walraven. Regimes of quantum degeneracy in trapped 1D gases. *Phys. Rev. Lett.*, 85:3745, 2000.

[120] L. Pollet, S. M. A. Rombouts, and P. J. H. Denteneer. Ultracold Atoms in One-Dimensional Optical Lattices Approaching the Tonks-Girardeau Regime. *Phys. Rev. Lett.*, 93:210401, 2004.

[121] D. Porras and J. I. Cirac. Bose-einstein condensation and strong-correlation behavior of phonons in ion traps. *Phys. Rev. Lett.*, 93:263602, 2004.

[122] D. Porras and J. I. Cirac. Effective quantum spin systems with trapped ions. *Phys. Rev. Lett.*, 92:207901, 2004.

[123] R. Raussendorf and H. J. Briegel. A one-way quantum computer. *Phys. Rev. Lett*, 86:5188, 2001.

[124] N. Read and S. Sachdev. Large-N expansion for frustrated quantum antiferromagnets. *Phys. Rev. Lett.*, 66:1773, 1991.

[125] C. Regal, M. Greiner, and D. S. Jin. Observation of resonance condensation of fermionic atom pairs. *Phys. Rev. Lett.*, 92:040403, 2004.

[126] S. Richard, F. Gerbier, J. H. Thywissen, M. Hugbart, P. Bouyer, and A. Aspect. Momentum spectroscopy of 1D phase fluctuations in bose-einstein condensates. *Phys. Rev. Lett.*, 91:010405, 2003.

[127] J. Richter, R. Darradi, R. Zinke, and R. F. Bishop. Path integrals in the theory of condensed helium. *Int. J. Modern Phys. B*, 21:2273, 2007.

[128] J. Richter, C. Gros, and W. Weber. Chiral ordering in a frustrated quantum spin system. *Phys. Rev. B*, 44:906, 1991.

[129] C. F. Roos, T. Monz, K. Kim, M. Riebe, H. Haeffner, D. F. V. James, and R. Blatt. Nonlinear coupling of continuous variables at the single quantum level. *arXiv:0705.0788v1 [quant-ph]*, 2007.

[130] S. Sachdev. *Quantum Phase Transitions*. Cambridge University Press, 1999.

[131] J. P. Schiffer. Phase transitions in anisotropically confined ionic crystals. *Phys. Rev. Lett.*, 70:818, 1993.

[132] F. Schmidt-Kaler, H. Häffner, M. Riebe, S. Gulde, G. P. T. Lancaster, T. Deuschle, C. Becher, C. F. Roos, J. Eschner, and R. Blatt. Realization of the CiracZoller controlled-NOT quantum gate. *Nature*, 422:408, 2003.

[133] R. Schmied. *in preparation*, 2008.

[134] R. Schmied, T. Roscilde, V. Murg, D. Porras, and J. I. Cirac. Quantum phases of trapped ions in an optical lattice. *arXiv:0712.4073v1 [cond-mat.str-el]*, 2007.

[135] U. Schollwöck. The density-matrix renormalization group. *Rev. Mod. Phys.*, 77:259, 2005.

[136] F. Schreck, L. Khaykovich, K. L. Corwin, G. Ferrari, T. Bourdel, J. Cubizolles, and C. Salomon. A quasipure bose-einstein condensate immersed in a fermi sea. *Phys. Rev. Lett.*, 87:080403, 2001.

[137] N. Schuch, M. M. Wolf, F. Verstraete, and J. I. Cirac. The computational complexity of PEPS. *Phys. Rev. Lett.*, 98:140506, 2007.

[138] T. D. Schultz, D. C. Mattis, and E. H. Lieb. Two-dimensional ising model as a soluble problem of many fermions. *Rev. Mod. Phys.*, 36:856, 1964.

[139] N. Shibata. Thermodynamics of the Anisotropic Heisenberg Chain Calculated by the Density Matrix Renormalization Group Method. *J. Phys. Soc. Jpn.*, 66:2221, 1997.

[140] P. W. Shor. *SIAM J. Comput.*, 26:1484, 1997.

[141] A. Sørensen and K. Mølmer. Spin-spin interaction and spin squeezing in an optical lattice. *Phys. Rev. Lett.*, 83:2274, 1999.

[142] A. T. Sornborger and E. D. Stewart. Higher-order methods for quantum simulations. *Phys. Rev. A*, 60:156, 1999.

[143] M. Sredniicki. Entropy and area. *Phys. Rev. Lett.*, 71:666, 1993.

[144] D. Stick, W. K. Hensinger, S. Olmschenk, M. J. Madsen, K. Schwab, and C. Monroe. Ion trap in a semiconductor chip. *Nature Physics*, 2:36, 2006.

[145] T. Stöferle, H. Moritz, C. Schori, M. Köhl, and T. Esslinger. Transition from a Strongly Iinteracting 1D Superfluid to a Mott Insulator. *Phys. Rev. Lett.*, 92:130403, 2004.

[146] E. Størmer. *J. Funct. Anal.*, 3:48, 1969.

[147] M. Suzuki. *Phys. Lett. A*, 146:319, 1990.

[148] M. Suzuki. *J. Math. Phys.*, 32:400, 1991.

[149] B. L. Tolra, K. M. O'Hara, J. H. Huckans, W. D. Phillips, S. L. Rolston, and J. V. Porto. Observation of reduced three-body recombination in a fermionized 1d bose gas. *Phys. Rev. Lett.*, 92:190401, 2004.

[150] M. Troyer and U. Wiese. Computational complexity and fundamental limitations to fermionic quantum Monte Carlo simulations. *Phys.Rev.Lett.*, 94:170201, 2005.

[151] W. van Dam, M. Mosca, and U. Vazirani. How powerful is adiabatic quantum computation ? *Proceedings of the 42nd Annual Symposium on Foundations of Computer Science*, pages 279–287, 2001.

[152] F. Verstraete and I. J. Cirac. Valence bond solids for quantum computation. *Phys. Rev. A*, 70:060302, 2004.

[153] F. Verstraete and J. Cirac. Matrix product states represent ground states faithfully. *Phys. Rev. B*, 73:094423, 2006.

[154] F. Verstraete and J. I. Cirac. Renormalization algorithms for Quantum-Many Body Systems in two and higher dimensions. *arXiv:cond-mat/0407066v1*, 2004.

[155] F. Verstraete, J. I. Cirac, and V. Murg. Matrix Product States, Projected Entangled Pair States, and variational renormalization group methods for quantum spin systems. *to be published in Adv. Phys.*, 2008.

[156] F. Verstraete, J. J. García-Ripoll, and J. I. Cirac. Matrix Product Density Operators: Simulation of finite-T and dissipative systems. *Phys. Rev. Lett*, 93:207204, 2004.

[157] F. Verstraete, D. Porras, and J. I. Cirac. DMRG and periodic boundary conditions: a quantum information perspective. *Phys. Rev. Lett*, 93:227205, 2004.

[158] F. Verstraete and A. Winter. *in preparation*, 2008.

[159] F. Verstraete, M. M. Wolf, D. Perez-Garcia, and J. I. Cirac. Criticality, the area law, and the computational power of peps. *Phys. Rev. Lett.*, 96:220601, 2006.

[160] G. Vidal. Efficient classical simulation of slightly entangled quantum computations. *Phys. Rev. Lett*, 91:147902, 2003.

[161] G. Vidal. Efficient simulation of one-dimensional quantum many-body systems. *Phys. Rev. Lett*, 93:040502, 2004.

[162] G. Vidal. Classical simulation of infinite-size quantum lattice systems in one spatial dimension. *Phys. Rev. Lett.*, 98:070201, 2007.

[163] G. Vidal, J. I. Latorre, E. Rico, and A. Kitaev. Entanglement in quantum critical phenomena. *Phys. Rev. Lett*, 90:227902, 2003.

[164] J. Villain. *J. Phys. (Paris)*, 38:26, 1977.

[165] X. Wang and T. Xiang. Transfer-matrix density-matrix renormalization-group theory for thermodynamics of one-dimensional quantum systems. *Phys. Rev. B*, 56:5061, 1997.

[166] X.-G. Wen. *Quantum Field Theory of Many-body Systems.* Oxford University Press, 2004.

[167] S. Wessel, F. Alet, S. Trebst, D. Leumann, M. Troyer, and G. G. Matrouni. Bosons in optical lattices - from the Mott transition to the Tonks-Girardeau gas. *arXiv:cond-mat/0411473v2*, 2004.

[168] S. R. White. Density-matrix algorithms for quantum renormalization groups. *Phys. Rev. B*, 48:10345, 1992.

[169] S. R. White. Density Matrix Formulation for Quantum Renormalization Groups. *Phys. Rev. Lett*, 69:2863, 1992.

[170] K. G. Wilson. The renormalization group: Critical phenomena and the Kondo problem. *Rev. Mod. Phys.*, 47:773, 1975.

[171] M. Wolf, F. Verstraete, M. Hastings, and J. Cirac. Area laws in quantum systems: mutual information and correlations. *arXiv:0704.3906v1*, 2007.

[172] M. M. Wolf. Violation of the entropic area law for fermions. *Phys. Rev. Lett.*, 96:010404, 2006.

[173] C. Wunderlich. Conditional spin resonance with trapped ions. *arXiv:quant-ph/0111158v1*, 2001.

[174] S. Yunoki and S. Sorella. Two spin liquid phases in the spatially anisotropic triangular Heisenberg model. *Phys. Rev. B*, 74:014408, 2006.

[175] Q. F. Zhong and S. Sorella. Spin-wave theory on finite lattices: Application to the J1-J2 Heisenberg model. *Europhys. Lett.*, 21:629, 1993.

[176] M. W. Zwierlein, C. A. Stan, C. H. Schunck, S. M. F. Raupach, S. Gupta, Z. Hadzibabic, and W. Ketterle. Observation of Bose-Einstein condensation of molecules. *Phys. Rev. Lett.*, 91:250401, 2003.

[177] M. Zwolak and G. Vidal. Mixed-state dynamics in one-dimensional quantum lattice systems: a time-dependent superoperator renormalization algorithm. *Phys. Rev. Lett*, 93:207205, 2004.

Danksagung

Ich möchte mich besonders bei Prof. Dr. J. Ignacio Cirac, dem Betreuer meiner Doktorarbeit, für seine Hilfsbereitschaft und Unterstützung bedanken. Er hat immer Zeit gefunden, sich mit meinen Fragen und Anliegen zu beschäftigen und hat mein Interesse an der theoretischen Physik gefördert. Besonderer Dank gebührt auch meinen Kollegen und Betreuern Belén Paredes, Frank Verstraete, Roman Schmied und Tommaso Roscilde, die mit mir zusammen gearbeitet haben und deren Ideen viele Teile der Arbeit erst ermöglichten.

Meinen Kollegen und Freunden danke ich für viele motivierende und aufmunternde Worte und die notwendige Abwechslung vom Physikstudium. Besonders bedanken möchte ich mich bei meinen Eltern, die mich sowohl finanziell als auch moralisch immer unterstützt haben.